SISSA ISAS

INTERNATIONAL SCHOOL FOR ADVANCED STUDIES
Condensed Matter Sector

Competing Mechanisms in Strongly Correlated Systems Close to a Mott Insulator

Thesis submitted for the degree of
Doctor Philosophiæ

Candidate
Michel Ferrero

Supervisors
Prof. Michele Fabrizio
Dr Federico Becca

October 2006

Contents

Contents i

Acknowledgments iii

1 Introduction 1

2 The Mott Transition: Models and Methods 9

- 2.1 The Hubbard Model . . . 9
- 2.2 Gutzwiller Wave Functions . . . 10
  - 2.2.1 Original Formulation . . . 11
  - 2.2.2 A Word About the $d \to \infty$ Limit . . . 13
  - 2.2.3 Generalized Multi-Band Gutzwiller Wave Functions . . . 14
  - 2.2.4 Example: The Single-Band Hubbard Model . . . 18
- 2.3 Dynamical Mean-Field Theory . . . 19
  - 2.3.1 Mapping to a Single-Site Model . . . 20
  - 2.3.2 The $d \to \infty$ Limit . . . 22
  - 2.3.3 The Bethe Lattice . . . 24
  - 2.3.4 Implementation by Iteration . . . 25
- 2.4 The Anderson Impurity Model . . . 26
- 2.5 The Kondo Model . . . 30
- 2.6 Wilson's Numerical Renormalization Group . . . 32
  - 2.6.1 One-Dimensional Formulation of the Model . . . 33
  - 2.6.2 Logarithmic Discretization . . . 34
  - 2.6.3 Iterative Diagonalization . . . 36
  - 2.6.4 Implementation . . . 37
  - 2.6.5 Fixed Points . . . 37
  - 2.6.6 Spectral Function . . . 38
- 2.7 Conformal Field Theory . . . 39
  - 2.7.1 Boundary Conformal Field Theory . . . 40
  - 2.7.2 Ground-State Degeneracy . . . 44
  - 2.7.3 Scattering Matrix . . . 44

3 Different Bandwidths in the Two-Band Hubbard Model 47

3.1 Introduction . . . 47
3.2 The Model . . . 49
3.3 Gutzwiller Variational Technique . . . 50
  3.3.1 Results for $J = 0$ . . . 52
  3.3.2 Results for $J \neq 0$ . . . 55
3.4 Dynamical Mean-Field Theory . . . 57
3.5 Single Impurity Spectral Properties . . . 63
3.6 Projective Self-Consistent Technique . . . 65
3.7 Discussion and Conclusions . . . 69

4 Critical Behavior in Impurity Trimers and Tetramers 73

4.1 Introduction . . . 73
4.2 The Impurity Dimer . . . 77
4.3 The Impurity Trimer . . . 80
  4.3.1 CFT Preliminaries for the Trimer . . . 81
  4.3.2 Fixed Points in the Trimer Phase Diagram . . . 82
  4.3.3 Concluding Remarks About the Trimer . . . 90
4.4 The Impurity Tetramer . . . 91
  4.4.1 CFT Preliminaries for the Tetramer . . . 92
  4.4.2 Fixed Points in the Tetramer Phase Diagram . . . 93
4.5 Conclusions . . . 99

A Character Decompositions 101

A.1 The Impurity Trimer . . . 101
A.2 The Impurity Tetramer . . . 102

B Modular $\mathcal{S}$-Matrices 105

B.1 Modular $\mathcal{S}$-Matrix for the Ising Model . . . 105
B.2 Modular $\mathcal{S}$-Matrix for the TIM . . . 105
B.3 Modular $\mathcal{S}$-Matrix for the $c = 1$ CFT . . . 106

Bibliography 107

Acknowledgments

I would like to express my gratitude to Michele Fabrizio for proposing the challenging and exciting subjects of my thesis and for sharing his enthusiasm, understanding and profound knowledge of the theory of strongly correlated systems. My sincere thanks also to Federico Becca for helping and assisting me with great expertise, for his encouragements and availability. The close cooperation and numerous discussions with Michele and Federico have been a continuous motivation as well as a most rewarding experience for me.

Many thanks also to Frédéric Mila for introducing me to the field of condensed matter physics at the EPFL in Lausanne and for remaining available and open to communication during my years in Trieste. It has been a fantastic opportunity to be able to continue working together with him and with Arnaud Ralko, Federico Becca and Dmitri Ivanov on the project of quantum dimers. I am grateful to my friends of the condensed matter group at the EPFL for their hospitality and the many fruitful exchanges, especially with Arnaud Ralko and Cédric Weber.

The work related to the orbital-selective Mott transition has been enhanced by many instructive debates with Massimo Capone, Luca de' Medici, Antoine Georges, Akihisa Koga, Ansgar Liebsch, Nicola Manini, and Manfred Sigrist. I am obliged to all of them. I am also indebted to Lorenzo de Leo and Giuseppe Santoro for introducing me to Wilson's numerical renormalization group.

It has been a pleasure to spend these fascinating years at SISSA together with many new friends, sharing our scientific and other interests. In this respect, I wish to acknowledge the captivating conversations with Walter van Suijlekom, Guido Fratesi, Adriano Mosca Conte, Manuela Capello, Tommaso Caneva and Nicola Lanatà. I would also like to thank Giuliano Niccoli for our lasting friendship and for the help he gave me in understanding certain aspects of conformal field theory.

Finally, I would like to thank my family for the support they provided me and for their continuous encouragements and trust as well as Petra for the wonderful time we have spent together in Trieste.

Chapter 1

Introduction

Strongly Correlated Systems

One of the greatest successes of the quantum mechanical description of solids certainly was the development of band structure theory and the classification of crystalline solids into conductors and insulators. Roughly speaking, within this approach every electron is assumed to feel an effective periodic potential produced by the positive ions and the other electrons, and any other electron-electron correlation is neglected. The eigenstates of the one-particle problem are classified according to their crystal momentum and the corresponding eigenvalues form dispersing bands. If the number of electrons in the crystal is such that there is a finite energy gap between the last occupied state and the lowest unoccupied one, the crystal is an insulator, otherwise it is a metal.

Even if this treatment seems oversimplified, it has been very successful, especially to describe solids with very wide bands. However, soon after the introduction of band theory, examples were shown that could not be understood within this framework. In 1934, de Boer and Verwey [19] reported that many properties of some transition-metal oxides were in disagreement with band-structure calculations. These materials are insulators whereas they are expected to be conductors because of their partially filled d-band. Mott and Peierls [92, 93] suggested that the reason for the failure of conventional band structure theory might be its poor mean-field-like treatment of the repulsive electron-electron Coulomb interaction. Indeed, if the electrons were moving slowly, they would be spending more time on every atomic site and hence experience a strong interaction with the other electrons present on the same atom. If the energy cost of this interaction is too big, it might become favorable for the electrons to stop moving at all and form what is now universally called a *Mott insulator*.

With these considerations, the solids can be further classified. In those with large conduction bands, the electrons are delocalized and move fast over the whole crystal. They do not interact strongly and are well described by Bloch waves. Other solids, instead, have narrower bands with the consequence that the electrons move slower and remain for a longer time at a given lattice site. Typical candidates are transition metal oxides where the hopping between the partially filled *d*-shells of the transition metal ions is bridged by the oxygen cage and can hence become comparable with the *d*-shell Coulomb repulsion or the metal-oxygen charge transfer gap. Other candidates are for instance molecular conductors, where the large separation between neighboring molecules makes the inter-molecular hopping very small. As a result, the energy scale coming from the electronic interaction becomes of the same order as the band energy gain. These systems are said to be *strongly correlated* and the rather localized electrons are not anymore well characterized by the purely Bloch wave-like picture provided by band theory. In some cases, correlations are so strong to stabilize a Mott insulator where a description in terms of localized Wannier orbitals is the most appropriate. In less extreme situations, the correlated material is still metallic but the competition between the two energy scales, and hence between a wave-like against a particle-like behavior, leads to very interesting physical phenomena.

Over the past decades, many novel materials displaying unusual behaviors that are poorly described by conventional techniques have been discovered and together with these, new theoretical methods have been developed. The behavior of magnetic impurities diluted in a metallic host and the subsequent introduction of the Kondo and Anderson impurity models are just one example of these phenomena. It is however surely the discovery of high-temperature superconductivity [16] in doped Mott insulator cuprates that triggered today's great interest in strongly correlated materials.

Experimental Results

Let us consider some particular examples where strong electronic correlations play a relevant role. A very interesting experimental opportunity arises when it is possible to control the bandwidth by varying external parameters, like the pressure, that modify the structure of the crystal and increase or decrease the overlap between neighboring orbitals. For some materials, it is then possible to induce a *Mott transition* from a metal to a Mott insulator, or vice versa, as a function of external parameters. This is the case for $(V_{1-x}Cr_x)_2O_3$ [83] whose phase diagram is shown in the left panel of Fig. 1.1. At temperatures above ~ 200 K a Mott transition between a paramagnetic insulator and a metal is observed. It is interesting to note that, at low temperatures, the insulator develops an antiferromagnetic ordering, signaling that other energy scales besides the Coulomb repulsion/charge transfer gap and the band energy gain, come into play: in this example, the Coulomb exchange, the super-exchange and the coupling to the lattice.

Another example is the organic compound κ-(BEDT-TTF)$_2$Cu[N(CN)$_2$]Cl

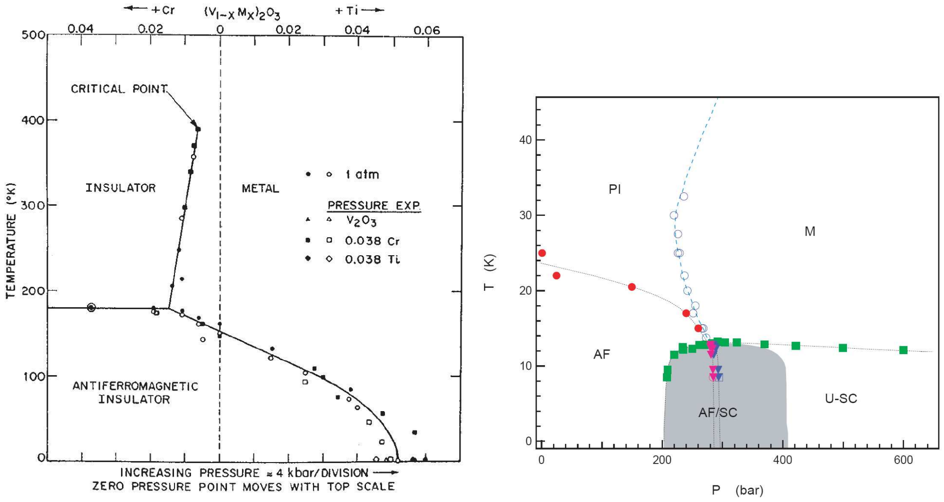

Figure 1.1: Left: Phase diagram for the metal-insulator transition in $(V_{1-x}Cr_x)_2O_3$ as a function of doping with Cr or Ti and as a function of pressure [83]. Right: Phase diagram of κ-(BEDT-TTF)$_2$Cu[N(CN)$_2$]Cl as a function of pressure [76].

showing unconventional superconductivity at low temperatures. Its phase diagram [76] is shown in the right panel of Fig. 1.1. An observation strikes the eye: There are many similarities between this phase diagram and that of $(V_{1-x}Cr_x)_2O_3$ although the energy scales are very different. This suggests that the mechanisms behind the Mott transition have a universal character. Here too, the paramagnetic insulator becomes magnetically ordered below ~ 20 K.

Signals of strong correlations are also found in the spectroscopic properties of many compounds. In Fig. 1.2 (left panel) we show the photoemission spectra for several d^1 transition metal oxides. In these systems, the lattice distortion changes the overlap between neighboring d-orbitals such that the compounds range from a Mott insulator to a paramagnetic metal [39]. It is clear from the data that the lower band seen at ~ -1.5 eV (called the lower *Hubbard band*) in the insulating $YTiO_3$ is already preformed in the metallic phase, *e.g.* of $SrVO_3$. Such a feature is not at all captured by standard band-structure calculations. In the metallic phase there is also a visible separation between a quasiparticle peak and the Hubbard band as one gets closer to the Mott transition. Although in this early data the quasiparticle peak is not very visible, later experiments allowed to have a higher definition, as shown in the right panel of Fig. 1.2. In this experiment [89], the photoemission spectra is shown for different photon energies. When the latter increases, thus sampling the solid deeper in the bulk, the quasiparticle peak gets higher and sharper.

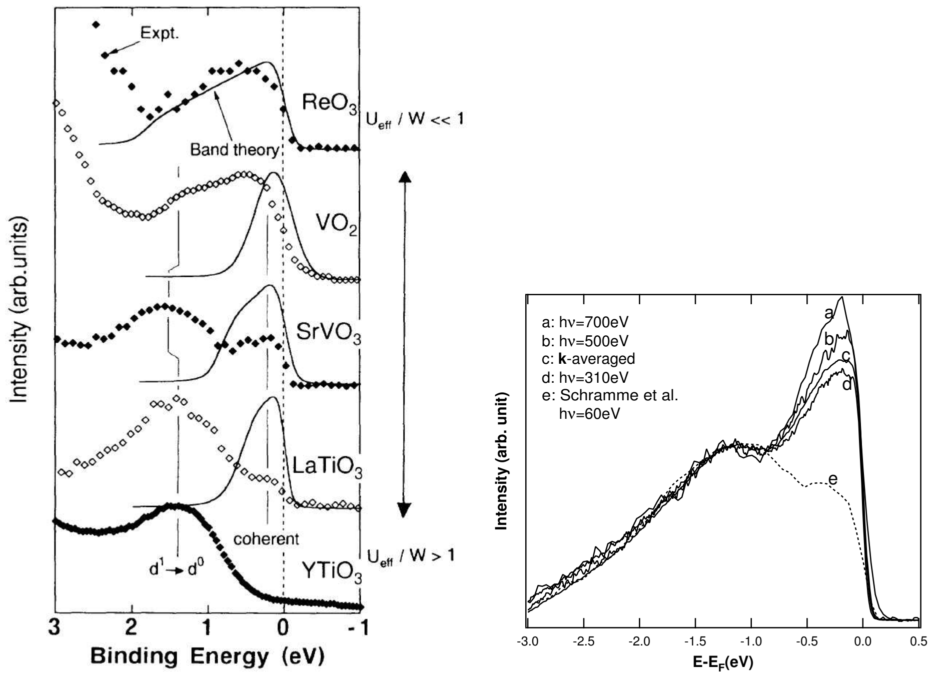

Figure 1.2: Left: Photoemission spectra of different perovskite-type transition metal oxides in the d-band region [39]. Right: Photoemission spectra of V_2O_3 taken with various photon energies $h\nu$ [89].

Let us finally show some experimental results about the single-layered ruthenates $Ca_{2-x}Sr_xRuO_4$ that are pertinent to the study of Chapter 3. The basic crystal structure of this compound is shown in the left panel of Fig. 1.3. The ruthenates have lately attracted a lot of interest because of the unconventional spin-triplet superconductivity observed in Sr_2RuO_4 [80]. Curiously, while Sr_2RuO_4 is a well-defined Fermi liquid, the substitution of Ca^{2+} for Sr^{2+} produces a Mott insulator, Ca_2RuO_4, with a staggered moment $S = 1$. Between these two extremes [95], a series of correlated metallic states are found, see the phase diagram in Fig. 1.3 (right panel). At low temperature, for dopings $0.5 \lesssim x < 2$, the system is a paramagnetic metal. As $x \to 0.5$, the characteristic Curie-Weiss temperature approaches zero. The most unusual properties are found at the critical concentration $x = 0.5$, where the magnetic susceptibility shows a free Curie form with a spin $S = 1/2$, coexisting with metallic transport properties. The region $0.2 \lesssim x \lesssim 0.5$ is characterized by antiferromagnetic correlations, still coexisting with metallic properties. Finally, for Ca concentrations $x \lesssim 0.2$, an insulating behavior is stabilized.

In these ruthenate alloys, the relevant $4d$-orbitals are split by the crystal field into an essentially threefold degenerate t_{2g} subshell that hosts 4 electrons

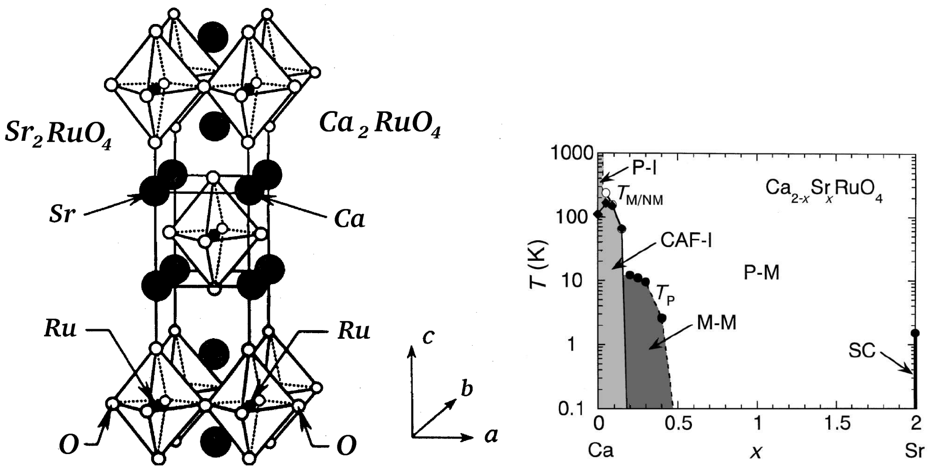

Figure 1.3: Left: Layered perovskite-like structure of the alloy series $Ca_{2-x}Sr_xRuO_4$. Right: Phase diagram as a function of the concentration x [95].

and a doubly degenerate empty e_g subshell that is lying at higher energy and does not participate in the conduction properties. While the transition at $x \sim 0.2$ to a Mott insulator can be understood by the narrowing of the d-bands because of modifications in the crystal structure, the exotic behavior near the critical concentration $x \sim 0.5$ calls for a more detailed analysis. Anisimov *et al.* [12] proposed that the behavior could be a consequence of the different bandwidth of the (xz,yz)-bands with respect to the xy-bands. Indeed, the xy-orbitals hybridize with four in-plane oxygen neighbors while the (xz,yz)-orbitals only hybridize with the two oxygens along the x,y axis. The resulting xy-band is about twice as large as the (xz,yz)-bands. In their scenario, as the concentration in Ca is increased, the bands get narrower and a first Mott transition is proposed to occur within the (xz,yz)-bands, which trap 3 electrons because of Hund's rules, while the xy-band is still conducting. The xy-band eventually becomes insulating for a higher concentration of Ca. This would explain the coexistence for $0.2 \lesssim x \lesssim 0.5$ of localized moments $S = 1/2$ formed by the three localized spins in the (xz,yz)-orbitals and metallic properties due to the itinerant xy-band. The proposal to have two distinct Mott transitions has lead to both experimental [15, 109] and theoretical controversy, as we will see in Chapter 3.

Effective Theoretical Models

The examples above are only a very limited selection of the extensive experimental work that has been devoted to strongly correlated materials. However, they show features, like the coexistence of delocalized quasiparticles and localized atomic-like excitations, or the presence of anomalous phases close to a Mott transition, that are common to many other compounds. From a theoretical standpoint, these similarities motivated the introduction of simple and quite universal models designed such as to contain the minimum number of ingredients able to uncover the physics of strong correlation. The most known example is the single-band Hubbard model, which is believed to be representative of many materials, including cuprates and the organic quasi-two dimensional compounds of Fig. 1.1. In this model, a *single* valence orbital per site is assumed. An electron on this orbital feels a Coulomb repulsion from another electron sitting the same orbital. In addition, electrons can hop from one lattice site to another. Even if very simplified, the Hubbard model contains the main ingredient of strong correlation, namely the competition between localization induced by the electronic repulsion and itineracy favored by the hopping term. Since this competition arises when both the Coulomb repulsion and the band-energy gain are comparable in magnitude, it lacks any small expansion parameter and it is very difficult to study, even in the simple case of the single-band Hubbard model. In spite of that, a lot of progresses have been achieved thanks to the development of the so-called dynamical mean-field theory [42]. Within this theory, a lattice model is mapped onto an effective single-site problem, which amounts to assume that spatial fluctuations are frozen, while full time dynamics is retained. This mapping is exact in infinite coordination lattices, but yet, it is assumed to remain a sensible approximation even beyond that limit. The resulting single-site model is easier to study and intense analytical and numerical studies over the past 15 years have shown that it captures many of the features observed experimentally. For instance, this method allowed to show that the coexistence of delocalized and localized single-particle excitations on well separated energy scales, as seen in photoemission spectroscopy, is a generic feature of the above-mentioned competition between the short-range Coulomb repulsion and the hopping energy. In other words, if one neglects all complications like magnetism or other symmetry breakings that may intervene at very low temperature and only considers the transition from a non-symmetry-breaking metal into an *ideal* non-symmetry-breaking Mott insulator, this transition is indeed characterized by the disappearance of a quasi-particle peak within well preformed Hubbard-side bands, which are almost insensitive to the transition.

However, on the insulating side of the transition, new energy scales come into play at low temperature, whose role is to rid the *ideal* non-symmetry-breaking Mott insulator of its residual entropy. As a result, a *realistic* insulating phase is eventually established, which is usually accompanied by a phase transition into some symmetry-broken phase, for instance a magnetic-ordered phase. These additional energy scales include, for instance, the on-site Coulomb exchange, responsible for the Hund's rules, the inter-site direct- or super-exchange, the coupling to the lattice or the crystal field. Obviously, these processes do exist also in the metallic side of the transition, hence one may wonder what is going to happen when the characteristic energy scale of the quasiparticles becomes comparable with them. We are going to argue that this situation uncovers a new type of competition which emerges before a metal-to-insulator Mott transition and which is as generic as the main competition between the Coulomb repulsion and the hopping energy.

The Thesis

In order to have further insight, let us assume that, among all these additional low-energy scales, a single one dominates, denoted as J. It can be regarded as the temperature at which the entropy of the residual degrees of freedom of the ideal Mott insulator start to be quenched. This is in contrast to recent research activities that focus on the possibility that different symmetry broken phases may compete in the insulating phases, leading to exotic phenomena [88]. We will discard this event and concentrate on the metallic phase adjacent the Mott insulator. Here, the quenching of the entropy is due to the formation of a Fermi sea of quasiparticles and takes place below the quasiparticle effective Fermi temperature, T_F^*, which might be much smaller than the bare T_F due to strong correlations. Since Landau quasiparticles carry the same quantum numbers as the electrons, the entropy quenching involves all degrees of freedom at the same time, including the charge. However, the presence of J provides the metallic phase with an alternative mechanism to freeze spin and eventually orbital degrees of freedom, independently of the charge ones, and becomes competitive with the onset of a degenerate quasiparticle gas when $T_F^* \simeq J$. Unlike the competition between different symmetry-broken Mott-insulating phases, which requires fine tuning of the Hamiltonian parameters and may only accidentally occur in real materials, this new type of competition should be accessible whenever it is possible to move gradually from a Mott insulator into a metallic phase, for instance by doping or applying pressure.

Clearly, a single-site, single-band model is not suited to study this issue. However, over the past years a large effort has been devoted to account for these extra ingredients like the exchange-splitting, the crystal-field splitting, the inter-site magnetic exchange and so on. They have for example lead to multi-band generalizations or to extensions of the dynamical mean-field theory that account for short-range spatial interactions by mapping the lattice model onto a small cluster of sites. Nevertheless, most of these efforts have not put much emphasis on the competition induced by these additional ingredients which, we believe, may be the key to understand the emergence of the anomalous phases observed in many strongly-correlated materials close to a Mott transition.

In this thesis, we intend to investigate the effects of this competition in two different generalizations of a single-band model. Let us briefly outline our work:

In Chapter 2, we present some of the theoretical methods and models that have been developed to study the physics of strongly correlated materials and that will be used in the thesis. We follow the example of the single-band Hubbard model for which the formalism is easiest to write, introducing generalizations for some techniques when it proves necessary.

This will provide all the necessary background to investigate, in Chapter 3, the role of the bandwidth difference in a two-band Hubbard model in infinite dimensions. Such a model could be relevant to understand the physics of compounds like the ruthenates described above. In particular, we explore the possibility to have a so-called orbital-selective Mott transition, for which distinct Mott transitions appear in the two bands at different values of the on-site Coulomb repulsion. We show that for a ratio small enough between the bandwidths, two distinct transitions can occur and that particular features appear in the low-energy properties of the system.

In the second part of the thesis, presented in Chapter 4, we focus on the properties of two clusters made of three and four impurities. These clusters appear in extensions of the dynamical mean-field theory and we discuss them in this context. We show that the competition between conventional Kondo screening and inter-impurity couplings reveals a very interesting physics and that the presence of anomalous bulk phases close to the Mott transition might be traced back to instabilities that are already present at the impurity level.

Chapter 2

The Mott Transition: Models and Methods

We expose the main techniques that we use in Chapters 3 and 4. Even though we will be investigating more complicated models, we consider the prototypical example of the single-band Hubbard model and show the connection between different methods that have been developed to understand its physics. The first approach we introduce is the Gutzwiller variational technique and the so-called Gutzwiller approximation to evaluate average values over the variational wave function. We then present the dynamical mean-field theory, in which the original Hubbard model is mapped onto a single-site problem, and emphasize the important role played by impurity models to describe the Mott transition. In particular, the Kondo and the Anderson impurity models are introduced as well as Wilson's numerical renormalization group that enables to study impurity models in detail. We conclude the chapter with an overview of conformal field theory, a powerful tool to analyze and classify the fixed points of the renormalization group applied to impurity models.

2.1 The Hubbard Model

From a theoretical perspective, the search for an understanding of strongly correlated systems has lead to the introduction of simplified models that capture the main features of strongly correlated electrons. Essentially simultaneously, Hubbard [54], Gutzwiller [45] and Kanamori [63] proposed a very simple model that contains the minimum ingredients to account for both band-like and localized behavior. Their model is obtained by neglecting fully-occupied and unoccupied bands. It is more careful to say that the degrees of freedom provided by these bands have been "integrated out", leading to renormalized parameters in the Hamiltonian. The remaining Wannier orbitals are those close to the Fermi level (the valence bands) and, in the most elementary form of the model, there is just one such orbital. This could represent materials in which the orbital degeneracy has been lifted completely by a crystal field. The resulting Hamiltonian reads

$$\mathcal{H} = \mathcal{H}_0 + \mathcal{H}_{\text{int}} = -\sum_{ij\sigma} t_{ij}\, f^{\dagger}_{i,\sigma} f_{j,\sigma} + H.c. + U \sum_{i} n_{i\uparrow} n_{i\downarrow}, \tag{2.1}$$

where $f^{\dagger}_{i,\sigma}$ creates an electron in the Wannier orbital with spin σ and $n_{i\sigma} = f^{\dagger}_{i\sigma} f_{i\sigma}$ is the occupation number. The first part of the Hamiltonian $\mathcal{H}_0$ expresses, through t_{ij}, the possibility of an electron hopping between neighboring sites i and j. Another approximation is to neglect the long-range tail of the Coulomb interaction which is assumed to be local. This is encoded in $\mathcal{H}_{\text{int}}$ and U is the energy cost for having two electrons on the same orbital. Changing the ratio U/t emulates the effect of varying external parameters like the pressure.

What makes the Hubbard model so interesting is that it combines two drastically different behaviors: On one hand, $\mathcal{H}_0$ is a tight-binding Hamiltonian leading to the formation of bands that are delocalized and on the other hand, $\mathcal{H}_{\text{int}}$ is a purely local term that tends to form atomic states. In other words, if $U = 0$ the Hamiltonian describes a metal and if $t_{ij} = 0$ it describes an insulator. The basic question of what the behavior between these two limits might be has given the physics community a real challenge, and many techniques and approximation schemes have been developed. Despite its apparently simple form, the Hubbard model has an exact solution only in 1 dimension so far.

The scenario for the Mott transition proposed by Hubbard assumes that the density of states in the Mott insulator is concentrated in two subbands: a lower and an upper Hubbard band, representing states with empty and doubly occupied sites. As U is decreased, the two bands move towards the chemical potential to finally get back to the non-interacting density of states for $U = 0$, see Fig. 2.1. In this picture, which is close to the original ideas of Mott [92], the transition is driven by the closing of a gap between the Hubbard bands in the density of states and should occur for a U of the order of the bandwidth of the conduction band. This interpretation is clearly based on the atomic limit and gives a rather good description of the case of large U. For that limit, effective models that describe the low-energy physics of the Hubbard model have been developed and gave birth to the Heisenberg and $t - J$ model.

Brinkman and Rice [20], building on previous works by Gutzwiller, gave a description of the Mott transition starting from the non-interacting limit. The idea is to start from the solution of the non-interacting Hamiltonian $\mathcal{H}_0$ and construct a variational wave function that accounts for electronic correlations. Let us describe this technique that will be used in Chapter 3.

2.2 Gutzwiller Wave Functions

Originally interested in the possibility of a ferromagnetic transition in narrow-band conductors, Gutzwiller [45, 46, 47] developed a variational approach

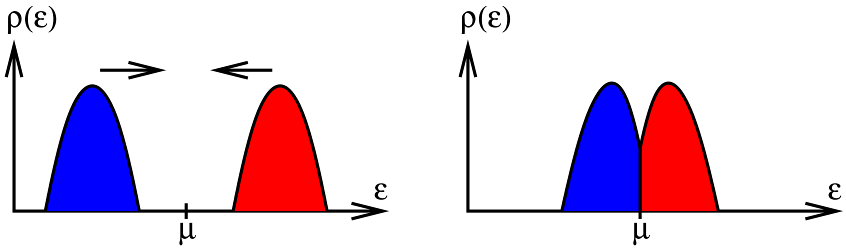

Figure 2.1: The Mott transition as seen by Hubbard. The two subbands merge into each other as the Coulomb repulsion U is decreased.

to include electronic correlations in an otherwise uncorrelated wave function. Gutzwiller's technique has later received a lot of interest, mostly for its success to describe the phenomenology of normal ^{3}He.

2.2.1 Original Formulation

Let us consider the ground state of $\mathcal{H}_0$ in the Hubbard model (2.1). In this Fermi-sea state, the occupation of an orbital by an up-spin electron is independent of its occupation by a down-spin electron. In the half-filled case, the probability to have an up-spin is the same as for a down-spin electron and is given by $1/2$. This means that the probability to have a doubly occupied site is $1/4$, which reflects the presence of important charge fluctuations. Clearly, as we start to give U a non-zero value, these doubly occupied states have a high energy cost. To be specific, the average value of the energy in the Fermi sea goes like $U/4$ and would eventually grow larger than that of a wave function corresponding to disconnected sites with one electron sitting on them. In order to avoid a too large energy as U is increased, it is necessary to reduce the number of double occupancies.

Gutzwiller's idea was to construct a trial wave function starting from $|\Psi_0\rangle$, the uncorrelated ground state of $\mathcal{H}_0$, and applying a projector on it that reduces the number of doubly occupied sites. In practice, the variational wave function $|\Psi\rangle$ is written as

$$|\Psi\rangle = \mathcal{P}_G|\Psi_0\rangle = \prod_i [1 - (1 - g) n_{i\uparrow} n_{i\downarrow}] |\Psi_0\rangle,$$

where $\mathcal{P}_G$ is the Gutzwiller projector and g a variational parameter. If $g = 1$ the projector has no effect and we obtain the original uncorrelated state for $U = 0$. When $g \neq 1$, the effect of $\mathcal{P}_G$ is to lower the contributions of those states that have two electrons on the same site. In the extreme case $g = 0$, these states are completely removed and we have a good ground state for $U \to \infty$. Note that, in going from $|\Psi_0\rangle$ to $|\Psi\rangle$, only the absolute value of the coefficients of the real space configurations with doubly occupied sites have been diminished. The relative phases of the configurations are still the same and insure that even after the projection there is still a sharp Fermi surface, so that $|\Psi\rangle$ describes a metal for any $g \neq 0$. In order to have the best approximate ground state for a given value of U, the parameter g has to be tuned such as to minimize the ground-state energy

$$E(g) = \frac{\langle\Psi|\mathcal{H}|\Psi\rangle}{\langle\Psi|\Psi\rangle}.$$

Unfortunately, computing $E(g)$ is still a very complicated task and, to make progress, Gutzwiller introduced an approximation (now called the *Gutzwiller approximation*) to evaluate the variational energy. Let us define

$$d = \frac{1}{L}\langle\Psi|\sum_i n_{i\uparrow}n_{i\downarrow}|\Psi\rangle,$$

which is the average number of doubly occupied sites in the correlated state. d is some function of g and we can use it as variational parameter instead of g. The average value of the local interaction in terms of d is trivial

$$\frac{1}{L}\langle\Psi|\mathcal{H}_{\text{int}}|\Psi\rangle = Ud.$$

The evaluation of the average value of the kinetic term is a lot more difficult and involves computing a sum of configuration-dependent determinants. In the Gutzwiller approximation, these determinants lose their configuration dependence and the computation of the kinetic term boils down to mere combinatorics. Skipping all the details of this derivation, we just state the result. The variational ground-state energy is

$$E/L = Z_\uparrow\bar{\epsilon}_\uparrow + Z_\downarrow\bar{\epsilon}_\downarrow + Ud, \tag{2.2}$$

where the reduction factors Z_σ are the height of the discontinuities in the momentum distribution at the Fermi energy. Their expression reads

$$Z_\sigma = \frac{\left(\sqrt{(n_\sigma - d)(1 - n_\sigma - n_{-\sigma} + d)} + \sqrt{(n_{-\sigma} - d)d}\right)^2}{n_\sigma(1 - n_\sigma)}.$$

Here, n_σ is the average number of σ-electrons in the uncorrelated Fermi sea and $\bar{\epsilon}_\sigma$ their average kinetic energy

$$\bar{\epsilon}_\sigma = \frac{1}{L}\langle\Psi_0| - \Big(\sum_{ij} t_{ij}\, f^\dagger_{i,\sigma} f_{j,\sigma} + H.c.\Big)|\Psi_0\rangle.$$

The variational problem is solved by minimizing the ground-state energy (2.2) with respect to d.

Brinkman and Rice [20] realized that such an approximate solution could describe a metal-insulator transition in the case of half-filled bands, preventing any kind of symmetry breaking. In this case, by SU(2) spin symmetry, $n_\uparrow = n_\downarrow = 1/2$, $Z = 8d(1-2d)$ and the ground-state energy is minimized by

$$d = \frac{1}{4}\Big(1 - \frac{U}{8\bar{\epsilon}}\Big),$$

which yields

$$Z = 1 - \Big(\frac{U}{8\bar{\epsilon}}\Big)^2.$$

Therefore, the Gutzwiller approximation predicts a transition to an insulator when $U = U_c = 8\bar{\epsilon}$. Above this value, Z is pinned to 0. The existence of a Mott transition in the Gutzwiller approximation is rather surprising because if a numerical evaluation of the Gutzwiller variational wave function is performed for a finite-dimensional lattice, it describes a metallic state for any value of U and the Mott transition does not exist [113]. It is the Gutzwiller approximation that induces the presence of a Mott transition for a finite U. Another important point is that the insulator described by the Gutzwiller approximation is not realistic: It is completely featureless, with zero energy for any $U > U_c$.

It is interesting to note that in the previous expressions the lattice enters only through $\bar{\epsilon}$, which is also defined in continuous systems. It turns out that using the Gutzwiller approximation to compute the parameters of Landau's Fermi-liquid theory leads to results that are in surprisingly good agreement with experiments on ^{3}He [108]. This agreement was initially the only justification for what seemed to be a very crude approximation. The question of the reliability of the Gutzwiller approximation was finally settled in the late '80s by Metzner and Vollhardt [85, 86] who devised a method for carrying out the Gutzwiller variational procedure exactly. In their treatment, closed-form results can be obtained for spatial dimension $d = 1$ and $d \to \infty$. It was shown that the Gutzwiller approximation is actually exact when $d \to \infty$ and this ensured that the approximation itself is indeed a sensible one.

The limit of infinite dimensionality brought a lot of excitement. It allowed to bring systematic corrections in $1/d$ in the Gutzwiller approximation [40], but more importantly set a firm ground on which more general Gutzwiller wave functions could be constructed. As we will be interested in multi-band systems, the Gutzwiller projector needs to be modified to account for these additional degrees of freedom.

2.2.2 A Word About the $d \to \infty$ Limit

What is so special about the limit $d \to \infty$? Let us consider the example of the Hubbard model (2.1) on an hybercubic lattice in d dimensions. In that case, every site has $2d$ neighbors. When the dimensionality goes to infinity the number of these neighbors grows and the possible hopping events grow.

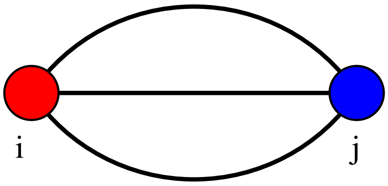

Figure 2.2: A term in a typical diagrammatic expansion. The operator $\mathcal{A}_i$ is represented by the left vertex and $\mathcal{B}_j$ by the right one. Because three independent fermionic lines connect the vertices, this diagram gives a vanishing contribution unless $i = j$.

If the prefactors t_{ij} do not scale correctly, the kinetic term would grow huge leading to a trivial physics. It was shown [112] that a finite density of states is recovered only if $t_{ij} = t/\sqrt{2d}^{|i-j|}$. The local Coulomb repulsion, on the contrary, is not aware of the increasing number of neighbors and does not need any special treatment. As a consequence of the scaling of the t_{ij}, the hopping matrix elements also behave like

$$\langle \Psi_0 | c_i^\dagger c_j | \Psi_0 \rangle \sim 1/\sqrt{2d}^{|i-j|}, \tag{2.3}$$

where $|\Psi_0\rangle$ is the ground state of $\mathcal{H}_0$ and local indices that do not matter here are neglected. This property brings in very important simplifications in the diagrammatic evaluation of average values. Generally, in a perturbation expansion one is lead to compute quantities of the form

$$\langle \Psi_0 | \mathcal{A}_i \sum_j \mathcal{B}_j | \Psi_0 \rangle,$$

where $\mathcal{A}_i$ and $\mathcal{B}_j$ are generic operators on the lattice sites i and j. In the diagrammatic computation of this quantity, the operators can be represented as vertices connected by a certain number of fermionic lines given by (2.3). The simplifications [87, 94] arise when there are three or more independent lines that connect i and j, see Fig. 2.2. In that case, for a given Manhattan distance R between the sites, the fermionic lines bring a factor scaling at most as $1/(2d)^{3R/2}$. The eventual summation over j, instead, brings a factor $(2d)^R$. As $d \to \infty$ the overall factor $(2d)^{-R/2}$ goes to zero except when $i = j$ (because then $R = 0$). In conclusion, any two vertices that are connected by three or more independent paths must correspond to the same site. This will be very useful in constructing multi-band Gutzwiller wave functions and within the dynamical mean-field theory.

2.2.3 Generalized Multi-Band Gutzwiller Wave Functions

The goal is to construct a variational wave function for models that have more than a single band and to find an approximation to evaluate average values in this variational state. There are, in principle, many ways to do this and it is not easy to figure out which ones provide a sensible physics. The works by Metzner and Vollhardt [85, 86] have shown that part of the success of the Gutzwiller approximation lies in the fact that there is a limit in which it is exact, that of infinite dimensionality. Therefore, it seems natural to follow the route $d \to \infty$ in order to have a controlled approximation and we follow Ref. [13, 22, 23] to show how this can be done. Let us consider a general k-orbital Hamiltonian $\mathcal{H} = \mathcal{H}_0 + \mathcal{H}_{\text{int}}$ that contains, beside the hopping term

$$\mathcal{H}_0 = -\sum_{ij\sigma\sigma'} \sum_{a,b=1}^{k} t_{ij,ab}^{\sigma\sigma'} f_{i,a\sigma}^{\dagger} f_{j,b\sigma'} + H.c., \tag{2.4}$$

an on-site interaction of the general form

$$\mathcal{H}_{\text{int}} = \sum_{i} \sum_{n,\Gamma} U(n,\Gamma)\, \mathcal{P}_i(n,\Gamma), \tag{2.5}$$

where $\mathcal{P}_i(n,\Gamma) = |i;n,\Gamma\rangle\langle i;n,\Gamma|$ is the projector onto the site-i state Γ with n electrons. Clearly, the $|i;n,\Gamma\rangle$ are eigenvectors of the interaction Hamiltonian. Hereafter, we use Greek letters to label the eigenvectors of (2.5) whereas Roman letters denote the natural basis of the Hilbert space of atomic configurations: $|i;n,I\rangle = f_{i,a\sigma}^{\dagger} \ldots f_{i,b\sigma'}^{\dagger}|0\rangle$. In terms of these, the eigenvectors are

$$|i;n,\Gamma\rangle = \sum_{I} A_{\Gamma I}\, |i;n,I\rangle,$$

so that the interaction Hamiltonian in the natural basis is written as

$$\mathcal{H}_{\text{int}} = \sum_{i} \sum_{n,\Gamma,I,J} U(n,\Gamma)\, A_{\Gamma I} A_{\Gamma J}^{*}\, \mathcal{P}_i(n,I,J), \tag{2.6}$$

where $\mathcal{P}_i(n,I,J) = |i;n,I\rangle\langle i;n,J|$ is a generic off-diagonal projector. The natural generalization for the Gutzwiller wave function $|\Psi\rangle$ is obtained from the Fermi-sea Slater determinant of the non-interacting Hamiltonian $|\Psi_0\rangle$ through

$$|\Psi\rangle = \mathcal{P}_G\, |\Psi_0\rangle = \prod_i \mathcal{P}_{i\,G}\, |\Psi_0\rangle,$$

where the operator $\mathcal{P}_{i\,G}$ acts on site i and is given by a sum over the projectors that appear in (2.6)

$$\mathcal{P}_{i\,G} = \sum_{n,I,J} \lambda_{nIJ}\, \mathcal{P}_i(n,I,J).$$

Here, the λ_{nIJ} are the variational parameters that need to be optimized such as to minimize the variational energy $E = \langle\Psi|\mathcal{H}|\Psi\rangle/\langle\Psi|\Psi\rangle$. Unfortunately, exactly computing E analytically is a very difficult problem and we want to derive an approximation scheme that would become exact in infinite dimensions. Let us consider the average value of a local operator $\mathcal{O}_i$ on site i

$$\frac{\langle\Psi|\mathcal{O}_i|\Psi\rangle}{\langle\Psi|\Psi\rangle} = \frac{\langle\Psi_0|\mathcal{P}^\dagger_{i\,G}\,\mathcal{O}_i\,\mathcal{P}_{i\,G}\,\prod_{j\neq i}\mathcal{P}^\dagger_{j\,G}\mathcal{P}_{j\,G}|\Psi_0\rangle}{\langle\Psi_0|\prod_i\mathcal{P}^\dagger_{i\,G}\mathcal{P}_{i\,G}|\Psi_0\rangle}. \tag{2.7}$$

To take advantage of the $d\to\infty$ limit, it is necessary to derive a diagrammatic expansion of this quantity. When all the $\lambda_{nIJ}=\delta_{IJ}$ the projector is just the identity, so in order to construct a perturbation expansion we write

$$\mathcal{P}^\dagger_{i\,G}\mathcal{P}_{i\,G} = 1+\sum_{n,I,J}\left(\sum_K \lambda_{nIK}\lambda^*_{nJK}-\delta_{IJ}\right)\mathcal{P}_i(n,I,J) = 1+\bar{P}_i,$$

where $\bar{P}_i$ is the perturbation around the identity and the prefactors of $\mathcal{P}_i(n,I,J)$ are the small parameters of the expansion. We can now write the product in the numerator of (2.7) as

$$\prod_{j\neq i}\mathcal{P}^\dagger_{j\,G}\mathcal{P}_{j\,G} = 1+\sum_{k=1}^{\infty}\frac{1}{k!}\sum_{i_1,\dots,i_k}{}'\prod_{j=i_1}^{i_k}\bar{P}_j,$$

where the prime on the sum indicates that $i\neq i_1\neq\ldots\neq i_k$. The generic form of a term in the numerator of (2.7) is therefore $\langle\Psi_0|\mathcal{P}^\dagger_{i\,G}\,\mathcal{O}_i\,\mathcal{P}_{i\,G}\,\prod_j\bar{P}_j|\Psi_0\rangle$. The diagram for this contribution has an external vertex i that represents the operator $\mathcal{P}^\dagger_{i\,G}\mathcal{O}_i\mathcal{P}_{i\,G}$ and a set of internal vertices j that embody the effect of $\bar{P}_j$. These vertices are connected by fermionic lines $\langle\Psi_0|f^\dagger_{i,a\sigma}f_{j,b\sigma'}|\Psi_0\rangle$. A typical diagram is shown in Fig. 2.3. An important simplification would arise if in any diagram there were vertices connected by at least three independent paths. As we have seen earlier, this would imply that the contribution from the diagram vanishes unless the vertices are on the same site. Given that $i\neq i_1\neq\ldots\neq i_k$, this means that any such diagram would vanish and only the trivial order would participate in the average value, i.e. $\langle\Psi_0|\mathcal{P}^\dagger_{i\,G}\,\mathcal{O}_i\,\mathcal{P}_{i\,G}|\Psi_0\rangle$.

However, without imposing further restrictions on the structure of $\bar{P}_i$ the diagrams do not satisfy this property. It is easy to see that the vertices of a diagram are connected by three independent paths whenever there are at least three fermionic lines coming out of every vertex. The non-vanishing diagrams are those that display vertices $\bar{P}_i$ that have less than three fermionic lines. It is therefore necessary to require that these vertices cancel. This can be enforced by imposing

$$\langle\Psi_0|\mathcal{P}^\dagger_{i\,G}\mathcal{P}_{i\,G}|\Psi_0\rangle = \langle\Psi_0|\Psi_0\rangle = 1, \tag{2.8}$$

$$\langle\Psi_0|f^\dagger_{i,a\sigma}f_{i,b\sigma'}\,\mathcal{P}^\dagger_{i\,G}\mathcal{P}_{i\,G}|\Psi_0\rangle = \langle\Psi_0|f^\dagger_{i,a\sigma}f_{i,b\sigma'}|\Psi_0\rangle. \tag{2.9}$$

The first equation is equivalent to imposing $\langle\Psi_0|\bar{P}_i|\Psi_0\rangle = 0$. In the diagrammatic language this means that an isolated vertex $\bar{P}_i$ cancels, see panel (A)

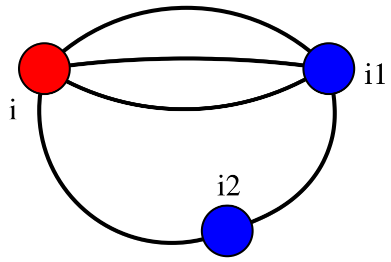

Figure 2.3: Typical diagram appearing in the computation of the numerator of (2.7). The vertex i represents $\mathcal{P}_{i\,G}^{\dagger}\mathcal{O}_i\mathcal{P}_{i\,G}$ whereas the vertices i_1 and i_2 correspond to $\bar{P}_{i_1}$ and $\bar{P}_{i_2}$.

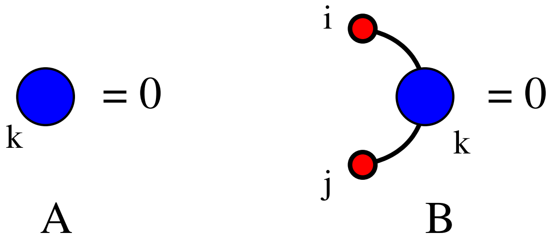

Figure 2.4: Diagrammatic illustration of the restrictions (2.8) and (2.9). (A) An isolated vertex $\bar{P}_k$ vanishes. (B) When the vertex $\bar{P}_k$ is connected to any two operators $f_{i,a\sigma}^{\dagger}$ and $f_{j,b\sigma'}$ it cancels.

---

in Fig. 2.4. The second equation reads $\langle\Psi_0|f_{i,a\sigma}^{\dagger}f_{i,b\sigma'}\,\bar{P}_i|\Psi_0\rangle = 0$. In evaluating the left-hand side, there is a first term in which $f_{i,a\sigma}^{\dagger}$ and $f_{i,b\sigma'}$ are contracted and multiply $\langle\Psi_0|\bar{P}_i|\Psi_0\rangle$. By equation (2.8) this term vanishes. The other contribution comes from the diagram in which the two operators are connected to the vertex $\bar{P}_i$. Therefore, the restriction (2.9) requires that whenever a vertex $\bar{P}_i$ is connected to two operators $f_{i,a\sigma}^{\dagger}$ and $f_{i,b\sigma'}$ it vanishes. Note that the two operators connect to the different terms in the Hartree-Fock decomposition of $\bar{P}_i$. There are $(2k)^2$ such terms corresponding to the possible pairs of fermionic operators. Given that (2.9) is also imposing $(2k)^2$ conditions, we expect that all the terms in the Hartree-Fock decomposition of $\bar{P}_i$ cancel. In other words, $\bar{P}_i$ vanishes when it is connected to *any* two operators, see panel (B) in Fig. 2.4.

We have shown that in infinite dimensions, imposing specific constraints on the Gutzwiller projector, the average value of a local operator $\mathcal{O}_i$ is simply given by

$$\frac{\langle\Psi|\mathcal{O}_i|\Psi\rangle}{\langle\Psi|\Psi\rangle} = \langle\Psi_0|\mathcal{P}_{i\,G}^{\dagger}\,\mathcal{O}_i\,\mathcal{P}_{i\,G}|\Psi_0\rangle.$$

Indeed, with the considerations made above, it is clear that the denominator on the left-hand side is 1. Similar arguments show that the average value of the kinetic term is reduced to

$$\begin{aligned}\frac{\langle\Psi|f^{\dagger}_{i,a\sigma}f_{j,b\sigma'}|\Psi\rangle}{\langle\Psi|\Psi\rangle} &= \langle\Psi_0|\mathcal{P}^{\dagger}_{i\,G}\,f^{\dagger}_{i,a\sigma}\,\mathcal{P}_{i\,G}\mathcal{P}^{\dagger}_{j\,G}\,f_{j,b\sigma'}\,\mathcal{P}_{j\,G}|\Psi_0\rangle \\ &= \sum_{\alpha\alpha' uv}\sqrt{Z^{u\alpha}_{a\sigma}Z^{v\alpha'}_{b\sigma'}}\langle\Psi_0|f^{\dagger}_{i,u\alpha}f_{j,v\alpha'}|\Psi_0\rangle,\end{aligned}$$

where the reduction factors are given by

$$\sqrt{Z^{u\alpha}_{a\sigma}} = \langle\Psi_0|\mathcal{P}^{\dagger}_{i\,G}\,f^{\dagger}_{i,a\sigma}\,\mathcal{P}_{i\,G}\,f_{i,u\alpha}|\Psi_0\rangle - \langle\Psi_0|f_{i,u\alpha}\,\mathcal{P}^{\dagger}_{i\,G}\,f^{\dagger}_{i,a\sigma}\,\mathcal{P}_{i\,G}|\Psi_0\rangle.$$

One can always express the original variational parameters λ_{nIJ} through $P(n,I,J)$, the correlated probabilities of the on-site projector

$$P(n,I,J) = \langle\Psi|\mathcal{P}_i(n,I,J)|\Psi\rangle.$$

Putting everything together, the Gutzwiller variational energy is given by

$$\begin{aligned}E &= \frac{\langle\Psi|\mathcal{H}_0+\mathcal{H}_{\text{int}}|\Psi\rangle}{\langle\Psi|\Psi\rangle} \\ &= -\sum_{ij\sigma\sigma'}\sum_{a,b=1}^{k}\sum_{\alpha\alpha' uv} t^{\sigma\sigma'}_{ij,ab}\sqrt{Z^{u\alpha}_{a\sigma}Z^{v\alpha'}_{b\sigma'}}\,\langle\Psi_0|f^{\dagger}_{i,u\alpha}f_{j,v\alpha'}+H.c.|\Psi_0\rangle \qquad (2.10) \\ &\quad+\sum_i\sum_{n,\Gamma,I,J} U(n,\Gamma)\,A_{\Gamma I}A^{*}_{\Gamma J}\,P(n,I,J).\end{aligned}$$

Here E is understood as being a function of the correlated probabilities $P(n,I,J)$ and one needs to minimize it with respect to these parameters.

2.2.4 Example: The Single-Band Hubbard Model

Let us review here the single-band Hubbard model (2.1) using the general formalism presented above and show that one indeed recovers the result (2.2) obtained by Gutzwiller.

There are four atomic states, an empty site, two states with one spin and a doubly occupied state. These states are all eigenvectors of the interaction Hamiltonian and therefore the Gutzwiller projector is a sum over diagonal projectors only

$$\mathcal{P}_G = \prod_i \mathcal{P}_{i\,G} = \prod_i\sum_{n,I}\lambda_{nI}\,\mathcal{P}_i(n,I,I).$$

Instead of using the variational parameters λ_{nI}, we use $P(n,I) = \langle\Psi|\mathcal{P}_i(n,I,I)|\Psi\rangle$. They are related through

$$\lambda^2_{nI} = \frac{P(n,I)}{P^{(0)}(n,I)},$$

where $P^{(0)}(n,I) = \langle \Psi_0 | \mathcal{P}_i(n,I,I) | \Psi_0 \rangle$ is the uncorrelated probability of the configuration I. In this example, we will denote the correlated probabilities of the four atomic configurations by $P(0)$, $P(\uparrow)$, $P(\downarrow)$, and $P(2)$. Clearly, the variational energy for the on-site interaction is simply given by $UP(2)$. The restrictions (2.8) and (2.9) read

$$\begin{aligned} P(0) + P(\uparrow) + P(\downarrow) + P(2) &= 1 \\ P(\uparrow) + P(2) &= n_\uparrow^{(0)} \\ P(\downarrow) + P(2) &= n_\downarrow^{(0)}. \end{aligned}$$

A simple calculation shows that the reduction factors are given by

$$\begin{aligned} \sqrt{Z_\sigma^{\sigma'}} &= \delta_{\sigma\sigma'} \frac{1}{n_\sigma^{(0)}} \Big(\sqrt{P(0)P(\sigma)} \sqrt{\frac{P^{(0)}(\sigma)}{P^{(0)}(0)}} \\ &\quad + \sqrt{P(-\sigma)P(2)} \sqrt{\frac{P^{(0)}(2)}{P^{(0)}(-\sigma)}} \Big) \\ &= \delta_{\sigma\sigma'} \frac{\Big(\sqrt{P(0)P(\sigma)} + \sqrt{P(-\sigma)P(2)} \Big)}{\sqrt{n_\sigma^{(0)}(1 - n_\sigma^{(0)})}}, \end{aligned}$$

which, upon using the restrictions above and defining $d = P(2)$, can be written as

$$Z_\sigma^{\sigma'} = \delta_{\sigma\sigma'} \frac{\Big(\sqrt{(1 - n_\sigma^{(0)} - n_{-\sigma}^{(0)} + d)(n_\sigma^{(0)} - d)} + \sqrt{(n_{-\sigma}^{(0)} - d)d} \Big)^2}{n_\sigma^{(0)}(1 - n_\sigma^{(0)})}.$$

This is the same result as the the variational energy (2.2).

In conclusion, average values on the Gutzwiller wave function can be computed analytically in $d \to \infty$ and the results coincide with the Gutzwiller approximation. However, as we previously mentioned, the Gutzwiller wave function leads to an unrealistic structureless insulator. Hence, it is not at all clear to what extent it is a faithful representation of the actual ground state. Novel techniques are therefore needed to have a more complete picture. In that respect, the development of dynamical mean-field theory over the past 15 years has brought important insights.

2.3 Dynamical Mean-Field Theory

As we have seen above, the difficulty that one faces in trying to understand the physics of the Mott transition is that it occurs in a region where $U \sim t$. Most of the techniques that had been developed before the '90s were, in one way or another, designed around $U/t \ll 1$ or $U/t \gg 1$. The introduction of dynamical mean-field theory (DMFT) provided a new approach to the Mott transition that overcame part of these difficulties. The theory was born in the beginning of the '90s, when there was a growing interest in the limit of infinite dimensionality (see [42] for a review). We will describe DMFT in more detail in this section, but let us briefly summarize some of its important aspects that have allowed significant advances in understanding the physics of strongly correlated materials. The theory can be thought of as a quantum version of classical mean-field theory. It maps a lattice model onto a single-site problem and, whereas the spatial degrees of freedom are frozen and lead to a simplified treatment of the lattice model, dynamical fluctuations instead are fully retained. In the limit $d \to \infty$, this mapping is exact. Yet, DMFT is assumed to be a sensible approximation for any finite-dimensional systems. A central aspect is that, within DMFT, quasiparticle excitations and high-energy incoherent excitations are treated on equal footing.

2.3.1 Mapping to a Single-Site Model

DMFT can in principle be used on a variety of models but we will focus here on the simple example of the single-band Hubbard model. Generalizations to more complicated models, like the multi-band Hubbard model of Chapter 3, are usually straightforward. Let us consider the Hubbard Hamiltonian (2.1)

$$\mathcal{H} = -\sum_{i,j,\sigma} t_{ij}\,(c^{\dagger}_{i\sigma}c_{j\sigma} + H.c.) + U\sum_{i} n_{i\uparrow}n_{i\downarrow},$$

where we recall that U implements the local Coulomb repulsion of two electrons sitting on the same site and t_{ij} describe the hopping of nearest-neighbor sites. As we will be interested in the limit of infinite dimensions d (which is equivalent to the limit of infinite coordination number z), it is important that the hopping coefficients scale like $t_{ij} \sim (1/\sqrt{d})^{|i-j|}$ in order to give a finite kinetic energy [87]. The partition function for this model can be written as a path integral

$$Z = \mathrm{Tr}\, e^{-\beta H} = \int \prod_{i,\sigma} Dc^{\dagger}_{i\sigma} Dc_{i\sigma} e^{-S},$$

where $\beta = 1/k_B T$ and with

$$S = \int_0^{\beta} \mathrm{d}\tau \left[\sum_{i,\sigma} c^{\dagger}_{i\sigma}(\tau)(\frac{\partial}{\partial\tau} - \mu)c_{i\sigma}(\tau) + H(c^{\dagger}_{i\sigma}, c_{i\sigma})\right].$$

Following up on the idea of a classical mean-field theory, one would like to reduce this to a single-site problem (see Fig. 2.5) with an effective action S_{eff} defined by

$$\frac{1}{Z_{\text{eff}}} e^{-S_{\text{eff}}(c^{\dagger}_0, c_0)} = \frac{1}{Z}\int \prod_{i\neq 0,\sigma} Dc^{\dagger}_{i\sigma} Dc_{i\sigma} e^{-S}.$$

Therefore we want to integrate out the contribution from all sites $i \neq 0$ and keep the full dynamics for the site 0. In order to achieve this, let us rewrite the action as the sum of three terms $S = S_0 + \Delta S + S^{(0)}$, where

$$
\begin{aligned}
S_0 &= \int_0^\beta d\tau \left[\sum_\sigma c^\dagger_{0\sigma}(\tau)(\frac{\partial}{\partial\tau} - \mu)c_{0\sigma} + U n_{0\uparrow}(\tau) n_{0\downarrow}(\tau) \right] \\
\Delta S &= -\int_0^\beta d\tau \left[\sum_{i,\sigma} t_{i0} c^\dagger_{i\sigma}(\tau) c_{0\sigma}(\tau) + t_{0i} c^\dagger_{0\sigma}(\tau) c_{i\sigma}(\tau) \right] \\
S^{(0)} &= \int_0^\beta d\tau \left[\sum_{i\neq 0,\sigma} c^\dagger_{i\sigma}(\tau)(\frac{\partial}{\partial\tau} - \mu) c_{i\sigma}(\tau) - \right. \\
&\qquad \left. \sum_{i\neq 0, j\neq 0,\sigma} t_{ij} c^\dagger_{i\sigma}(\tau) c_{j\sigma}(\tau) + \sum_{i\neq 0} U n_{i\uparrow}(\tau) n_{i\downarrow}(\tau) \right].
\end{aligned}
$$

S_0 is the action of the site 0, decoupled from the rest of the lattice. $S^{(0)}$ is the action of the lattice with the site 0 removed. Finally, ΔS is the action connecting the site 0 with the lattice. With these definitions, the partition function can be rewritten as

$$
\begin{aligned}
Z &= \int Dc^\dagger_{0\sigma} Dc_{0\sigma} e^{-S_0} \int \prod_{i\neq 0} Dc^\dagger_{i\sigma} Dc_{i\sigma} e^{-S^{(0)} - \Delta S} \\
&= \int Dc^\dagger_{0\sigma} Dc_{0\sigma} e^{-S_0} Z^{(0)} \langle \exp \int_0^\beta d\tau \sum_{i,\sigma} \Big(c^\dagger_{i\sigma}(\tau) \eta_{i\sigma} + \eta^+_{i\sigma} c_{i\sigma}(\tau) \Big) \rangle^{(0)},
\end{aligned}
$$

where $\langle \bullet \rangle^{(0)}$ denotes a thermal average over the action $S^{(0)}$, $Z^{(0)}$ is the partition function of the lattice without the site 0, and the sources $\eta_{i\sigma} = t_{i0} c_{0\sigma}$. The last term in the thermal average is recognized as the generating functional of the cavity Green's function $G^{(0)}$. It follows that

$$
\begin{aligned}
A &= \langle \exp \int_0^\beta \mathrm{d}\tau \sum_{i,\sigma} \Big(c^\dagger_{i\sigma}(\tau) \eta_{i\sigma} + \eta^+_{i\sigma} c_{i\sigma}(\tau) \Big) \rangle^{(0)} \\
&= \sum_{n=1}^{\infty} \sum_{i_1,\ldots,j_n,\sigma} \int_0^\beta d\tau_{i_1} \cdots d\tau_{j_n}\, \eta^\dagger_{i_1\sigma}(\tau_{i_1}) \cdots \eta^\dagger_{i_n\sigma}(\tau_{i_n}) \\
&\qquad \tilde{G}^{(0)}_{i_1\ldots j_n}(\tau_{i_1} \ldots \tau_{i_n}, \tau_{j_1} \ldots \tau_{j_n})\, \eta_{j_1\sigma}(\tau_{j_1}) \cdots \eta_{j_n\sigma}(\tau_{j_n}),
\end{aligned}
\tag{2.11}
$$

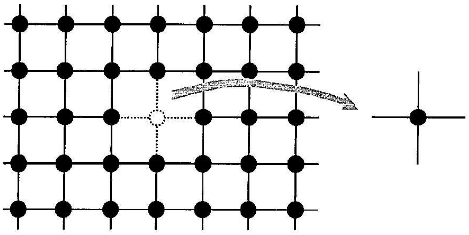

Figure 2.5: Mapping from the lattice model to a single-site problem.

where the $\tilde{G}^{(0)}_{i_1 \ldots j_n}$ are $2n$-point Green's functions of the lattice with the site 0 removed. We now have an expression for the effective action S_{eff}

$$\begin{aligned}
S_{\text{eff}} &= S_0 - \ln A + \text{const} \\
&= S_0 - \sum_{n=1}^{\infty} \sum_{i_1,\ldots,j_n,\sigma} \int_0^{\beta} d\tau_{i_1} \cdots d\tau_{j_n} \, t_{i_1 0} \cdots t_{0 j_n} \, c^{\dagger}_{0\sigma}(\tau_{i_1}) \cdots c^{\dagger}_{0\sigma}(\tau_{i_n}) \\
&\quad G^{(0)}_{i_1 \ldots j_n}(\tau_{i_1} \ldots \tau_{i_n}, \tau_{j_1} \ldots \tau_{j_n}) \, c_{0\sigma}(\tau_{j_1}) \cdots c_{0\sigma}(\tau_{j_n}) + \text{const},
\end{aligned} \tag{2.12}$$

where, by the linked cluster theorem, $G^{(0)}_{i_1 \ldots j_n}$ are the *connected* Green's functions of the lattice with a missing site. So far, we have obtained a single-site formulation of the problem, where the dynamics is described by the above effective action.

2.3.2 The $d \to \infty$ Limit

We can now use the simplifications generated by the $d \to \infty$ limit. As we have seen earlier, the t_{ij} scale like $(1/\sqrt{d})^{|i-j|}$, and so does the 2-point Green's function $G^{(0)}_{ij}$. Therefore, the contribution from $n = 1$ in (2.12) is of order 1. When one considers the contributions from $n \geq 2$, it turns out that they bring in a contribution of order at least $1/d$. Hence, in the limit $d \to \infty$ all contributions from $n > 1$ vanish and we are left with the following expression for S_{eff}

$$\begin{aligned}
S_{\text{eff}} = &\int_0^{\beta} d\tau_1 \int_0^{\beta} d\tau_2 \sum_{\sigma} c^{\dagger}_{0\sigma}(\tau_1) \, \mathcal{G}_0^{-1}(\tau_1 - \tau_2) \, c_{0\sigma}(\tau_2) \\
&+ \int_0^{\beta} d\tau \, U \, n_{0\uparrow}(\tau) \, n_{0\downarrow}(\tau) + \text{const},
\end{aligned} \tag{2.13}$$

where the Fourier transform of $\mathcal{G}_0^{-1}$ is given by

$$\mathcal{G}_0^{-1}(i\omega_n) = i\omega_n + \mu - \sum_{ij} t_{i0} t_{0j} G^{(0)}_{ij}(i\omega_n).$$

The action (2.13) describes a single site with a local Coulomb repulsion U. The site can exchange electrons with the external environment. This hybridization is encoded in $\mathcal{G}_0$, that plays the role of the effective Weiss field of classical mean-field theory. $\mathcal{G}_0$ is defined by the properties of the lattice with a missing site. In order to have a closed set of equations, it is necessary to relate these properties to those of the single site. In infinite dimensions, and for a general lattice, one can show that

$$G_{ij}^{(0)} = G_{ij}^{\mathrm{latt}} - \frac{G_{i0}^{\mathrm{latt}} G_{0j}^{\mathrm{latt}}}{G_{00}^{\mathrm{latt}}},$$

where G_{ij}^{latt} is the Green's function of the full lattice. Using this expression and taking a Fourier transform, one obtains

$$\mathcal{G}_0^{-1}(i\omega_n) = \Sigma^{\mathrm{latt}}(i\omega_n) + \left(\sum_{\mathbf{k}} G^{\mathrm{latt}}(\mathbf{k}, i\omega_n) \right)^{-1},$$

where the lattice Green's function in k-space is given by

$$G^{\mathrm{latt}}(\mathbf{k}, i\omega_n) = \frac{1}{i\omega_n + \mu - \epsilon_{\mathbf{k}} - \Sigma^{\mathrm{latt}}(i\omega_n)}, \tag{2.14}$$

with the non-interacting dispersion relation

$$\epsilon_{\mathbf{k}} = \sum_j t_{ij} e^{i\mathbf{k}(\mathbf{R}_i - \mathbf{R}_j)}.$$

A crucial point in deriving the above equations is that in the expression of the lattice Green's function (2.14), the self-energy $\Sigma^{\mathrm{latt}}(i\omega_n)$ of the lattice has no **k**-dependence. This can be proven to be true in the $d \to \infty$ limit [87, 94]. It is also possible to relate Σ^{latt} to G^{latt} via (2.14)

$$\sum_{\mathbf{k}} G^{\mathrm{latt}}(\mathbf{k}, i\omega_n) = \int \frac{\rho(\epsilon)}{i\omega_n + \mu - \epsilon - \Sigma^{\mathrm{latt}}(i\omega_n)},$$

where $\rho(\epsilon)$ is the non-interacting density of states, so that Σ^{latt} is given by

$$\Sigma^{\mathrm{latt}}(i\omega_n) = i\omega_n + \mu - \mathcal{R}\left[\sum_{\mathbf{k}} G^{\mathrm{latt}}(\mathbf{k}, i\omega_n) \right],$$

where $\mathcal{R}$ denotes the inverse Hilbert transform. In order to get a closed set of equations, one needs to impose a self-consistency which relates the lattice Green's function to the single-site. Given the translational invariance of the lattice, this is clearly obtained by imposing

$$G(i\omega_n) = \sum_{\mathbf{k}} G^{\mathrm{latt}}(\mathbf{k}, i\omega_n),$$

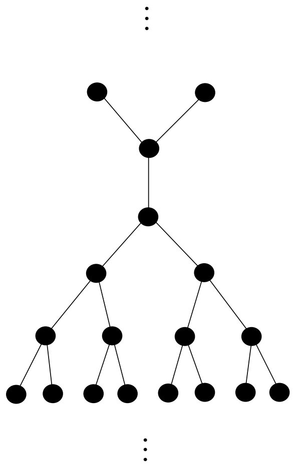

Figure 2.6: Illustration of the Bethe lattice for $z = 3$.

where $G(i\omega_n)$ is the Green's function of the single site. Putting everything together one gets the following self-consistency equation

$$\mathcal{G}_0^{-1}(i\omega_n) = i\omega_n + \mu - \mathcal{R}\left[G(i\omega_n)\right] + G^{-1}(i\omega_n). \tag{2.15}$$

In this equation, the lattice structure is encoded in the reciprocal Hilbert transform $\mathcal{R}$. Before going any further, we describe a particular lattice for which (2.15) takes an easy form and that will be used in Chapter 3.

2.3.3 The Bethe Lattice

In the above formulation of DMFT, the structure of the lattice enters only in the reciprocal Hilbert transform, through the non-interacting density of states $\rho(\epsilon)$. In general, $\rho(\epsilon)$ around the chemical potential is a smooth function. We exclude particular cases where the chemical potential is right at a van Hove singularity or in a dip where the density of states vanishes. Therefore, when one is interested in the generic mechanisms of the paramagnetic Mott transition, it is enough to consider any regular density of states extending over a finite interval of energy. A possible choice, that proves useful, is a semi-circular density of states which is obtained on the Bethe lattice (or Cayley tree). In this case, the Hilbert transform, and hence the self-consistency equation (2.15), takes a particularly simple form.

The Bethe lattice with connectivity z is a lattice on which every site is coupled to z neighbors and for which there is only one path to go from one site to another on the lattice, see Fig. 2.6. We consider the model for which there is only nearest-neighbor hopping $t_{ij} = t/\sqrt{z}$. In this case, and when

$z \to \infty$, the non-interacting density of states can be shown to be semi-circular

$$\rho(\epsilon) = \frac{1}{2\pi t^2}\sqrt{4t^2 - \epsilon^2}.$$

Using this expression, the reciprocal Hilbert transform is given by

$$\mathcal{R}\left[G(i\omega_n)\right] = t^2 G(i\omega_n) + G^{-1}(i\omega_n),$$

and when inserted in (2.15), it yields the following simple form of the self-consistency equation

$$\mathcal{G}_0^{-1}(i\omega_n) = i\omega_n + \mu - t^2 G(i\omega_n). \tag{2.16}$$

Hereafter, we will only consider the Bethe lattice and this form for the self-consistency equation. The physical quantities will be given in units of the half-bandwidth $D = 2t$.

The original problem has been mapped onto one of a single site living in an effective bath, described by $\mathcal{G}_0$, which can exchange particles. Using the limit of infinite dimensions, it was possible to find (2.16) which relates $\mathcal{G}_0$ to the Green's function of the site. In this limit, the original problem and the single-site problem are equivalent and the mapping is exact. It is however important to realize that one can also consider this mapping to be an approximation for a finite-dimensional problem. The approximation is then that of freezing the spatial fluctuations, neglecting the **k**-dependence of the lattice self-energy. The lattice Green's function can be recovered using (2.14) and the dispersion relation of the lattice (obtained by some other technique). In this way, more quantitative calculations can be realized, and this is for example the aim of LDA+DMFT. From this standpoint, the limit of infinite dimensions insures that DMFT provides a consistent set of equations. Finally, note that whereas the spatial fluctuations are frozen, the full time-dependence is taken into account and therefore quantum fluctuations are well described.

2.3.4 Implementation by Iteration

In an actual implementation, one usually starts with a guess for $\mathcal{G}_0$. This fully defines the action (2.13) and one can, in principle, solve the problem for the single site, extracting its Green's function. Inserting this Green's function in (2.16), one gets a new $\mathcal{G}_0$, in general different from the one used in the beginning. This new $\mathcal{G}_0$ defines a new action and a new problem to be solved. This procedure is repeated until convergence, see Fig. 2.7, and is usually achieved after a few iterations.

The practical difficulty is to extract the physical properties of the single-site, knowing its effective action. Although there are no spatial fluctuations, this is still a complicated many-body problem. Thankfully, various techniques are available to study the single-site problem, both numerical and analytical.

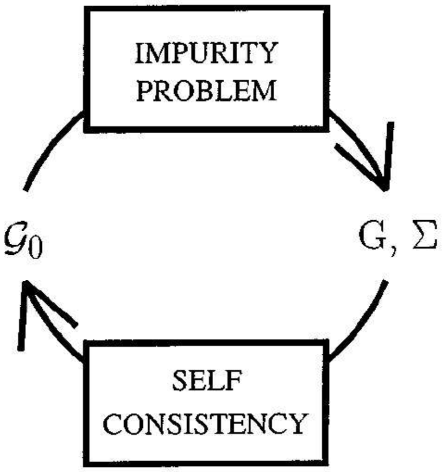

Figure 2.7: Schematic implementation of DMFT.

We choose to use mainly exact diagonalization with a Lanczos [73] procedure. Contrary to other techniques, like quantum Monte Carlo [42, 53] that can directly work with a time-discretized version of the effective action S_{eff}, an exact diagonalization method requires that the problem be brought to a matrix form. Hence, it proves very useful to find a Hamiltonian formulation of DMFT so that exact diagonalization techniques can be used.

Actually, a Hamiltonian formulation of DMFT not only provides a tool to make practical calculations, but also permits to gain considerable physical insight. What Hamiltonian should then be used to model the influence of the effective action? DMFT describes the physics of a site embedded in an effective bath, which strongly resembles that of an impurity embedded in a metal and exchanging electrons with its conduction electrons. The Hamiltonian that should therefore naturally arise is that of the Anderson impurity model [41].

2.4 The Anderson Impurity Model

The Anderson Impurity Model [10] appeared in the study of transition metal magnetic impurities with unfilled 3*d* shells diluted in a host metal (like Fe in Cu). In isolation, the ions have a magnetic moment given by the Hund's rules, but it is not clear if they retain a fraction of this moment, or none at all, when placed in a metallic environment. Indeed, experiments have shown that under certain conditions the impurities do keep a magnetic moment, and in other cases do not [52]. In order to have insight into this problem, Anderson suggested a very simple model that was able to explain these experimental results. His idea was that the resonance induced by the scattering off the impurity was roughly behaving like an atomic level (hybridized to the conduction electrons). As such, it would accommodate a certain equilibrium number of electrons and there would be a cost U for adding or removing an electron on that level. A difficulty arises because the occupation number in the resonance is a complicated object to deal with. Anderson's idea was to overcome it by replacing the resonance by an additional electronic level lying in the conduction band. The resulting Hamiltonian is

$$\mathcal{H}_{\mathrm{AM}} = \sum_{\mathbf{k}\sigma} \epsilon_{\mathbf{k}} c^{\dagger}_{\mathbf{k}\sigma} c_{\mathbf{k}\sigma} + \epsilon_d n_d + \sum_{\mathbf{k}\sigma} \left(V_{\mathbf{k}} c^{\dagger}_{\mathbf{k}\sigma} d_{\sigma} + H.c. \right) + U n_{d\uparrow} n_{d\downarrow}, \qquad (2.17)$$

where $n_{d\sigma} = d^{\dagger}_{\sigma} d_{\sigma}$ and $n_d = n_{d\uparrow} + n_{d\downarrow}$. The conduction electrons are described by the creation operators $c^{\dagger}_{\mathbf{k}\sigma}$ and have a dispersion relation $\epsilon_{\mathbf{k}}$. The operators $d^{\dagger}_{\sigma}$ create an electron on the additional electronic level sitting at an energy ϵ_d. The exchange of electrons between the conduction bands and the level is made possible through a hybridization term. In this context, $V_{\mathbf{k}}$ is the probability amplitude to have a transition from a conduction state with momentum $\mathbf{k}$ to the level. Finally, the energy cost coming from the Coulomb interaction between two electrons being on the electronic level is given by U.

Let us first of all make the connection with DMFT. It is necessary to bring the problem to a single-site one by integrating out the conduction electron degrees of freedom in (2.17). The resulting action on the electronic level is

$$\begin{aligned} S_{\mathrm{eff}} = &\int_0^{\beta} d\tau_1 \int_0^{\beta} d\tau_2 \sum_{\sigma} d^{\dagger}_{\sigma}(\tau_1)\, \mathcal{G}_0^{-1}(\tau_1 - \tau_2)\, d_{\sigma}(\tau_2) \\ &+ \int_0^{\beta} d\tau\, U\, n_{d\uparrow}(\tau)\, n_{d\downarrow}(\tau). \end{aligned} \qquad (2.18)$$

Here, $\mathcal{G}_0$ is the non-interacting ($U = 0$) Green's function of the Anderson model and its Fourier transform is given by

$$\mathcal{G}_0^{-1}(i\omega_n) = i\omega_n - \epsilon_d - \int_{-\infty}^{\infty} \frac{d\epsilon}{\pi} \frac{\Delta(\epsilon)}{i\omega_n - \epsilon},$$

where $\Delta(\epsilon) = \pi \sum_{\mathbf{k}} |V_{\mathbf{k}}|^2\, \delta(\epsilon - \epsilon_{\mathbf{k}})$. The action (2.18) is exactly the same as the action (2.13) provided that $\epsilon_d = -\mu$ and that the parameters $V_{\mathbf{k}}$, $\epsilon_{\mathbf{k}}$ are tuned such as to give $\mathcal{G}_0$ the shape required by DMFT. In other words, the effective single-site problem which the original Hubbard model is mapped onto can be seen as a particular Anderson impurity model. The self-consistency (2.16) now reads

$$t^2 G(i\omega_n) = \sum_{\mathbf{k}} \frac{|V_{\mathbf{k}}|^2}{i\omega_n - \epsilon_{\mathbf{k}}}, \qquad (2.19)$$

and relates the parameters of the Anderson model to the Green's function of the impurity. Such a Hamiltonian description of the impurity problem allows for a straightforward numerical iterative implementation [24]. One starts with a set of parameters $V_{\mathbf{k}}$, $\epsilon_{\mathbf{k}}$ that fully define the Hamiltonian (2.17). The Hamiltonian is diagonalized using a Lanczos procedure and the properties of the impurity can be computed. In particular, the Green's function is extracted. Then the self-consistency equation (2.19) is used to determine a new set of parameters for the next iteration. Ideally, there would be an infinite set of parameters such as to perfectly satisfy the self-consistency. However, a numerical implementation can only be carried out with a finite number of orbitals (and therefore a finite number of parameters) and the parameters for the next iteration are found by a fitting procedure along the imaginary axis.

The reformulation of the single-site problem as an Anderson impurity model is very useful as it allows to perform practical calculations, but more importantly this alternative approach provides a bridge between lattice and impurity models. At the time when DMFT was developed, a lot of work had already been done on impurity models, that were 40 years older, and many techniques had been developed. The knowledge about the Anderson model could therefore be used to know more about the Hubbard model.

When he introduced his impurity model, Anderson studied its properties within a Hartree-Fock approximation. He could conclude that there was a transition between a non-magnetic impurity regime and a magnetic one when $U\rho^{(0)}(\epsilon_d) > 1$ (here $\rho^{(0)}(\epsilon)$ is the non-interaction density of states). It was later shown that this transition was really a crossover [103] and that the low-frequency behavior of the Anderson model satisfied Fermi-liquid theory [74] as well as the Friedel sum rule. In the case of the symmetric Anderson model ($\epsilon_d = -U/2$), the spectral density $\rho(\epsilon)$ for small U has a large Abrikosov-Suhl resonance. As U is increased, the resonance gets narrower (its width is of the order of the Kondo temperature T_K) and coexists with two high-energy structures.

These studies have important consequences on the properties of the infinite-dimensional Hubbard model. With the assumption that $\mathrm{Im}\Sigma(i0^+) = 0$ and that $\mathrm{Re}\Sigma(i0^+)$ is finite, they imply [41] that the paramagnetic phase has a Fermi-liquid nature, so that the self-energy is expected to have the low-energy behavior

$$\begin{aligned}\mathrm{Re}\Sigma(\omega + i0^+) &= \mu + (1 - 1/Z)\omega + \ldots \\ \mathrm{Im}\Sigma(\omega + i0^+) &= -\Gamma\omega^2 + \ldots,\end{aligned}$$

where $Z^{-1} = 1 - [\partial\mathrm{Re}\Sigma(\omega)/\partial\omega]|_{\omega\to 0}$ is the quasiparticle residue, related to the effective mass by $m^*/m = 1/Z$. Also, the single-particle spectral density $\rho(\epsilon)$ is expected to have the same regimes as those that were found in the Anderson model. In the case of the half-filled Hubbard model the density of states for very small U has a shape close to the non-interacting one with some of the spectral weight transferred to the tails. For larger U, $\rho(\epsilon)$ has a three peak structure made of two bands (recognized as the Hubbard bands)

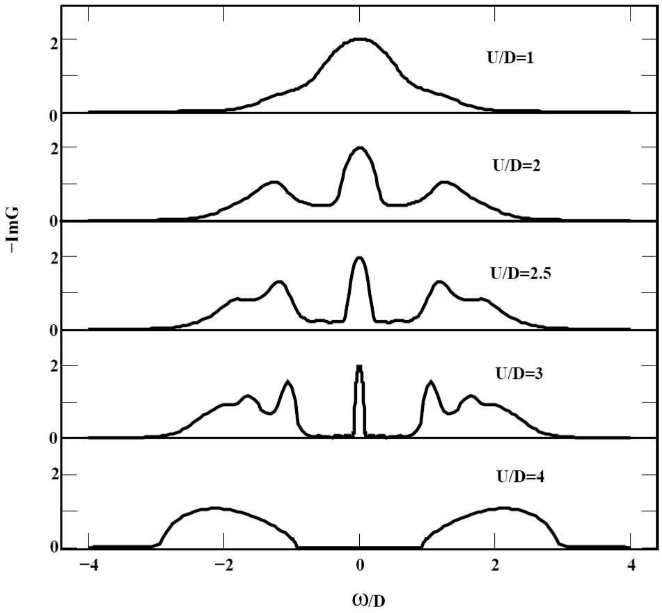

Figure 2.8: Local spectral density at $T = 0$, for increasing values of U/D. The results were obtained by iterated perturbation theory [114], on the infinite dimensional Bethe lattice.

at energies of order U and a narrow quasiparticle peak, the counterpart of the Abrikosov-Suhl resonance. There is therefore a transfer of spectral weight to the Hubbard bands as U is increased.

Those Fermi-liquid properties are found in a regime for which $\Delta(0) \neq 0$. This does not need to be true. In particular, the self-consistency within DMFT provides a mechanism to make $\Delta(0)$ vanish after some critical U_c, or in other words, to bring $T_K \to 0$. In the half-filled Hubbard model, it was shown [43, 59, 100] that, assuming $\Delta(0) = 0$, an insulating solution is stabilized. In this case, the Kondo model (see Section 2.5), obtained from the Anderson model with $\Delta(0) = 0$, scales to weak coupling [111], and the insulator has frozen charge degrees of freedom and spins that are free to fluctuate. The transition from the Fermi-liquid to the Mott insulator, obtained by increasing U, is described by the vanishing of the quasiparticle peak, transferring its weight to the Hubbard bands, that are already present in the metallic phase.

This picture for the Mott transition in the infinite-dimensional Hubbard model has later been confirmed by iterated perturbation theory [114], see Fig 2.8. As is clear from the figure, when U is large but still in the metallic phase, the quasiparticle peak is well separated from the Hubbard bands and the low-energy dynamics consists of spin fluctuations between $|\uparrow\rangle$ and $|\downarrow\rangle$, while the empty and doubly occupied states are decoupled. The physics of the

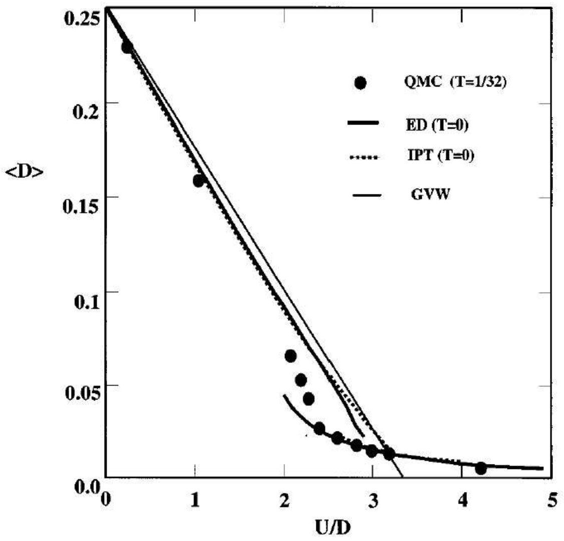

Figure 2.9: Double occupancy as a function of U/D. The data corresponds to QMC simulations (dots), exact diagonalization (bold line), iterated perturbation theory at $T = 0$ (dotted line) and the Gutzwiller approximation (thin line) [42].

resonance is therefore that of a single spin connected to the conduction bath. We will see that this is described by a particular limit of the Anderson model, the so-called s-d exchange model.

It is important to note that the insulator obtained by DMFT is not a trivial one. As can be seen from Fig. 2.9, the double occupancy does not vanish in the insulator because of the presence of small virtual hoppings. This is in contrast with the Gutzwiller approximation where the insulator is completely featureless. Nevertheless, the double occupancy appears to be the sum of two contributions: a smooth contribution across the Mott transition coming from the virtual hoppings and a contribution from the quasiparticle Fermi sea that vanishes at the critical U_c. The latter is actually captured well by the Gutzwiller approximation. Therefore, the results of the Gutzwiller approximation can still be very useful, especially in determining the properties related to the quasiparticle excitations.

2.5 The Kondo Model

The studies on the Anderson model made it clear that a sufficiently large Coulomb repulsion U with respect to the width of the resonance could induce a localized moment on the diluted impurities inside a metal. An important question that arises is how they might affect the conduction electrons of the host metal? Experimentally, it is observed that such impurities give anomalous contributions to many metallic properties, particularly to the transport properties such as resistivity and thermopower. One notable consequence is the observation of a resistance minimum occurring at low temperature. This is a surprising feature as in the case of non-magnetic impurities, with $T \to 0$, phonon scattering induces a monotonically decreasing resistivity going to a residual value at $T = 0$. The resistance minimum is observed at low temperatures, where the local moments are believed to be well established.

The model that allowed to explain these features is the s-d model, or Kondo model, in which the local magnetic moment is already formed and has a spin S. It is coupled via an exchange interaction J_K with the conduction electrons:

$$\mathcal{H} = \sum_{\mathbf{k}\sigma} \epsilon_{\mathbf{k}} c^{\dagger}_{\mathbf{k}\sigma} c_{\mathbf{k}\sigma} + J_K \, \mathbf{s} \cdot \mathbf{S},$$

where $\mathbf{s} = \frac{1}{2V} \sum_{\mathbf{k}\mathbf{k}'} c^{\dagger}_{\mathbf{k}\alpha} \boldsymbol{\sigma}_{\alpha\beta} c_{\mathbf{k}'\beta}$, V is the volume and $\mathbf{S}$ denotes the spin of the impurity. For $S = 1/2$, this model can be shown to be obtained from the Anderson model (2.17) in the limit $U \to \infty$. This is much in the same spirit as the connection between the Hubbard model and the $t - J$ model. Formally, the Kondo model is obtained by a Schrieffer-Wolff [104] transformation and the parameters of both models are related by

$$J_K = \frac{-|V_{\mathbf{k}}|^2 \, U \, V}{\epsilon_d (\epsilon_d + U)}.$$

Note that J_K is positive and therefore induces an antiferromagnetic coupling. By treating this model to third order perturbation theory in the coupling J, Kondo [68] was able to show that the magnetic interaction leads to singular scattering of the conduction electrons near the Fermi level and a $\ln T$ contribution to the resistivity

$$R(T) \sim S(S+1) J_K^2 c_{\text{imp}} \left[1 + 2\rho_0 J_K \ln \left(\frac{T}{D} \right) \right]^{-2},$$

where c_{imp} is the concentration of impurities, ρ_0 the density of states at the Fermi level and D the bandwidth of the conduction band. Because of the logarithmic terms, the perturbative approach of Kondo fails at very low temperature and one defines the Kondo temperature

$$T_K = D \exp \left(-\frac{1}{2\rho_0 J_K} \right),$$

below which the perturbative results are no longer valid. Indeed for $T \to T_K$, $R(T) \to \infty$. Kondo's treatment allowed to understand the resistance minimum but a different theory was needed to explain the physics of $T \to 0$.

This turned out to be a very involved issue, known as the Kondo problem, and it is only in the late '60s that the key notion of scaling, put forward by Anderson [11], provided the theoretical framework to understand the low-energy behavior of the Kondo model.

The idea was that if the higher order excitations were eliminated to give an effective model valid on a lower energy scale, the effective coupling between the local moment and the conduction electrons increased. In other words, at temperatures below T_K, the conduction electrons feel a coupling J_K to the impurity spin that flows to infinity, suggesting that the impurity effectively binds into a singlet with the conduction electrons. The screened impurity behaves like a non-magnetic impurity which explains the results found experimentally. Note that the same analysis can be carried by considering a ferromagnetic coupling ($J_K < 0$) and shows that the effective coupling flows to zero as $T \to 0$. Shortly later, building on the scaling ideas of Anderson, Wilson confirmed these results using the numerical renormalization group. This non-perturbative approach provided definitive results for the spin $S = 1/2$ model and can be easily generalized to different impurity models. We will describe Wilson's technique more in detail in Section 2.6 and use it in the following chapters.

Let us relate these findings to the Hubbard model. We have seen earlier that for U slightly below the critical U_c, the quasiparticle peak is essentially separated from the Hubbard bands. This represents a regime for which the Anderson impurity model maps on the Kondo model. The quasiparticle peak is therefore understood as being the lattice version of the resonance induced by the screening of the impurity by the conduction electrons. Its width is roughly given by the Kondo temperature T_K. Therefore, getting closer to the critical value of U of the Mott transition translates into a vanishing Kondo temperature in the corresponding Kondo model.

Impurity models, together with the techniques that were developed to study them, provide an important tool in understanding the Mott transition in infinite dimensions. Above, we focused on the single-band Hubbard model and the corresponding single-band Anderson and Kondo models. As we will see in the next chapters, more involved Hubbard models lead to different impurity models that can include several orbitals or in which the impurities are arranged in clusters. A careful analysis of these impurity models helps to come to grips with the underlying physics. An especially important tool that we will use is Wilson's numerical renormalization group that allows to have precise results about the low-energy properties of impurity models.

2.6 Wilson's Numerical Renormalization Group

The numerical renormalization group (NRG) method has been developed by Wilson [110] in the '70s to investigate the Kondo problem. The need for a renormalization technique came from the failure of perturbative approaches to describe the zero-temperature limit of the Kondo model. Indeed, the Kondo effect depends crucially on the presence of fermionic excitations down to arbitrarily small energy scales and the NRG proved to be a very powerful tool. Since then, NRG has been used to study a variety of impurity models and to derive their static and dynamical properties.

2.6.1 One-Dimensional Formulation of the Model

If originally formulated for the Kondo problem, the NRG methods can be equally well applied on the Anderson model and we present it for this model [70, 71]. In order to keep the notation simple, we will focus on the simplest Anderson impurity model, defined by the Hamiltonian

$$\mathcal{H} = \sum_{\mathbf{k}\sigma} \epsilon_{\mathbf{k}} c^{\dagger}_{\mathbf{k}\sigma} c_{\mathbf{k}\sigma} + \epsilon_d n_d + \sum_{\mathbf{k}\sigma} \left(V_{\mathbf{k}} c^{\dagger}_{\mathbf{k}\sigma} d_{\sigma} + H.c. \right) + U n_{d\uparrow} n_{d\downarrow}, \tag{2.20}$$

where $c^{\dagger}_{\mathbf{k}\sigma}$ creates a conduction bath electron with spin σ and momentum $\mathbf{k}$, $d^{\dagger}_{\sigma}$ creates a σ-spin on the impurity, $n_{d\sigma} = c^{\dagger}_{d\sigma} c_{d\sigma}$ and $n_d = \sum_{\sigma} n_{d\sigma}$ are occupation operators. In this Hamiltonian, U implements the Coulomb repulsion of two electrons sitting on the impurity and $V_{\mathbf{k}}$ the hybridization of the impurity with the conduction bath. Let us separate the Hamiltonian (2.20) in two parts, $\mathcal{H} = \mathcal{H}_{\mathrm{c}} + \mathcal{H}_{\mathrm{imp}}$, where $\mathcal{H}_{\mathrm{c}}$ is the Hamiltonian for the conduction band and $\mathcal{H}_{\mathrm{imp}}$ involves the impurity. The impurity is only connected to one specific linear combination of conduction bath operators

$$f_{0\sigma} = \frac{1}{\sqrt{\sum_{\mathbf{k}} |V_{\mathbf{k}}|^2}} \sum_{\mathbf{k}} V_{\mathbf{k}} c_{\mathbf{k}\sigma},$$

where we have properly normalized $f_{0\sigma}$. With this definition, $\mathcal{H}_{\mathrm{imp}}$ is written as

$$\mathcal{H}_{\mathrm{imp}} = \epsilon_d n_d + U n_{d\uparrow} n_{d\downarrow} + \sqrt{\sum_{\mathbf{k}} |V_{\mathbf{k}}|^2}\, f^{\dagger}_{0\sigma} d_{\sigma} + H.c.$$

It is then possible to transform the conduction-band part of the Hamiltonian to a tight-binding Hamiltonian, using a Lanczos procedure. Basically, one constructs a basis for the Hilbert space starting from $f^{\dagger}_{0\sigma}|0\rangle$ and successively applying the conduction-band Hamiltonian on these states. Expressed in this new basis, $\mathcal{H}_{\mathrm{c}}$ is tridiagonal and defined on a semi-infinite chain

$$\mathcal{H}_{\mathrm{c}} = \sum_{n=0}^{\infty} \left[\epsilon_n f^{\dagger}_{n,\sigma} f_{n,\sigma} + t_n (f^{\dagger}_{n,\sigma} f_{n-1,\sigma} + H.c.) \right], \tag{2.21}$$

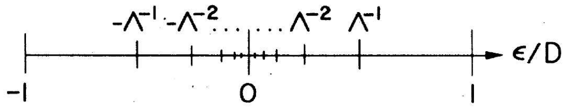

Figure 2.10: Logarithmic discretization of the energy interval $[-1, +1]$.

where $t_0 = 0$, and where the ϵ_n and t_n are defined by the recursion relations

$$\begin{aligned}&\epsilon_n = \langle f_{n,\sigma} | \mathcal{H}_\mathrm{c} | f_{n,\sigma} \rangle \\ &t_{n+1} \, | f_{n+1,\sigma} \rangle = (\mathcal{H}_\mathrm{c} - \epsilon_n) \, | f_{n,\sigma} \rangle - t_n \, | f_{n-1,\sigma} \rangle \\ &\langle f_{n+1,\sigma} | f_{n+1,\sigma} \rangle = 1. \end{aligned} \tag{2.22}$$

We used the notation $|f_{n,\sigma}\rangle = f^\dagger_{n,\sigma}|0\rangle$. Although the discretized problem is easily implemented numerically, it has the important drawback that the coefficients t_n go to a constant value with increasing n. For this reason, there is little hope to converge by considering a finite-length chain. The solution to this problem lies in a logarithmic discretization of the conduction band.

2.6.2 Logarithmic Discretization

The conduction band Hamiltonian (2.21) is defined on a one-dimensional semi-infinite chain. If we diagonalized it, we would obtain a Hamiltonian $\mathcal{H}_\mathrm{c} = \int_{-\infty}^{\infty} \epsilon \, c^\dagger_{\epsilon\sigma} c_{\epsilon\sigma}$, where $c^\dagger_{\epsilon\sigma}$ creates a conduction-band electron with energy ϵ. In terms of these, f_{0_σ} has the expression

$$f_{0\sigma} = \frac{1}{\sqrt{\sum_\mathbf{k} |V_\mathbf{k}|^2}} \int_{-\infty}^{\infty} \sqrt{\Delta(\epsilon)/\pi} \, c_{\epsilon\sigma}.$$

This defines the hybridization function $\Delta(\epsilon)$ which is a function of the conduction-band density of states and the parameters $V_\mathbf{k}$. The knowledge of $\Delta(\epsilon)$ fully determines the Anderson model. We will assume that $\Delta(\epsilon)$ is a smooth function around the chemical potential. As we are interested in the low-energy properties of the system, we model $\Delta(\epsilon)$ by a constant Δ_0 over the energy interval $[-D, D]$. The bandwidth is given by $2D$ and hereafter we use D as our unit energy. Neglecting the energy-dependence of $\Delta(\epsilon)$ around the chemical potential is not a crucial approximation in the study of the fixed points of an impurity model. Indeed, small changes in the structure of $\Delta(\epsilon)$ will not affect universal properties at the fixed point. Note, however, that this is no longer true if the density of states vanishes at the Fermi level, like in pseudo-gap systems. Also, if one is interested in more quantitative quantities, the details of $\Delta(\epsilon)$ might be important. This is for example the case when NRG is used as an impurity solver for DMFT. The self-consistency sets the shape of the conduction bath density of states and thus the energy dependence of $\Delta(\epsilon)$ is relevant. Note, that NRG can also be written for a general hybridization function [44].

We then introduce a parameter $\Lambda > 1$ and divide up the energy domain $[-1, +1]$ into a sequence of intervals $I_n = [\Lambda^{-(n+1)}, \Lambda^{-n}]$ as shown in Fig. 2.10. Within a positive (negative) interval I_n, we define a complete set of annihilation operators $a_{n\sigma}^{(p)}$ ($b_{n\sigma}^{(p)}$), with $p = 0, \pm 1, \pm 2, \ldots$. The associated wave functions $\Psi_{np}^{\pm}(\epsilon)$ form an orthonormal set for the functions defined in the interval I_n

$$\Psi_{np}^{\pm}(\epsilon) = \begin{cases} \frac{\Lambda^{n/2}}{(1-\Lambda^{-1})^{1/2}} e^{\pm i\omega_n p\epsilon} & \text{if } \pm\epsilon \in I_n \\ 0 & \text{if } \pm\epsilon \notin I_n, \end{cases}$$

and

$$\omega_n = \frac{2\pi\Lambda^n}{1-\Lambda^{-1}}.$$

The original operators $c_{\epsilon\sigma}$ can be expanded in this basis

$$c_{\epsilon\sigma} = \sum_{np} \left[a_{n\sigma}^{(p)} \Psi_{np}^{+}(\epsilon) + b_{n\sigma}^{(p)} \Psi_{np}^{-}(\epsilon) \right].$$

Using these new operators, one sees that the impurity is only connected to $a_{n\sigma}^{(0)}$ and $b_{n\sigma}^{(0)}$. Neglecting terms that have $p \neq 0$ one replaces all the operators $c_{\epsilon\sigma}$ in a positive energy interval I_n by a single operator

$$a_{n\sigma} = \frac{\Lambda^{n/2}}{(1-\Lambda^{-1})^{1/2}} \int_{I_n} c_{\epsilon\sigma}\, d\epsilon,$$

and similarly in a negative energy interval by $b_{n\sigma}$. Now the conduction-band Hamiltonian reads

$$\mathcal{H}_c/D = \frac{1}{2}(1+\Lambda^{-1}) \sum_n \Lambda^{-n} \left(a_{n\sigma}^{\dagger} a_{n\sigma} - b_{n\sigma}^{\dagger} b_{n\sigma} \right),$$

and

$$f_{0\sigma} = \left[\frac{1}{2}(1-\Lambda^{-1}) \right]^{1/2} \sum_n \Lambda^{-n/2} (a_{n\sigma} + b_{n\sigma}).$$

These new expressions can now be inserted in the recursion relations (2.22). When particle-hole symmetry holds, $\epsilon_n = 0$ and one finds, for the t_n,

$$t_{n+1} = \frac{1}{2}(1+\Lambda^{-1})\Lambda^{-n/2}\xi_n,$$

with

$$\xi_n = (1-\Lambda^{-n-1})(1-\Lambda^{-2n-1})^{-1/2}(1-\Lambda^{-2n-3})^{-1/2}.$$

We see that using the logarithmic discretization the t_n decay like $\Lambda^{-n/2}$ with increasing n. This is the consequence of separating the electronic energies into different orders of magnitude that contribute equally to the logarithmic divergences found at low-temperature in a perturbative approach to the Kondo model. We also see that the discretization has a bigger effect at high energies. Instead, energies close to the Fermi level are well sampled. The discretization ceases to be an approximation when $\Lambda \to 1$. On the other hand, the bigger Λ, the faster the decay of the hopping coefficients t_n. This demonstrates that one has to make a compromise between choosing a small Λ, that does not induce many discretization errors but requires the use of longer chains, or a large Λ, for which small chains can be used but discretization errors will become more important. Typical values for Λ range between 1.5 and 3.0. Putting everything together, the Hamiltonian (2.20) can be written as

$$\begin{aligned}\mathcal{H} = D\frac{1}{2}(1+\Lambda^{-1})\sum_{n=0}^{\infty}\Lambda^{-n/2}\xi_n\left[f^{\dagger}_{n,\sigma}f_{n+1,\sigma}+H.c.\right]\\ +\epsilon_d n_d + U n_{d\uparrow}n_{d\downarrow} + \sqrt{\frac{2D\Delta_0}{\pi}}\left(f^{\dagger}_{0\sigma}d_{\sigma}+H.c.\right).\end{aligned} \tag{2.23}$$

2.6.3 Iterative Diagonalization

The Hamiltonian (2.23) represents a chain with an impurity sitting at the first site. The rest of the chain is made of sites from and on which the electrons can hop with coefficients that decay with increasing distance from the impurity. It then seems natural to construct the chain by iteratively adding sites at its end. Let us therefore define the following Hamiltonian

$$\begin{aligned}\mathcal{H}_N = \Lambda^{(N-1)/2}\Bigg[\sum_{n=0}^{N-1}\Lambda^{-n/2}\xi_n\left(f^{\dagger}_{n,\sigma}f_{n+1,\sigma}+H.c.\right)\\ +\tilde{\epsilon}_d n_d + \tilde{U} n_{d\uparrow}n_{d\downarrow} + \tilde{\Delta}_0^{1/2}\left(f^{\dagger}_{0\sigma}d_{\sigma}+H.c.\right)\Bigg],\end{aligned} \tag{2.24}$$

where we have defined

$$\begin{aligned}\tilde{\epsilon}_d &= \left(\frac{2}{1+\Lambda^{-1}}\right)\frac{\epsilon_d}{D}\\ \tilde{U} &= \left(\frac{2}{1+\Lambda^{-1}}\right)\frac{U}{D}\\ \tilde{\Delta}_0 &= \left(\frac{2}{1+\Lambda^{-1}}\right)^2\frac{2\Delta_0}{\pi D}.\end{aligned}$$

The original Hamiltonian is recovered as

$$\mathcal{H} = \lim_{N\to\infty}\frac{1}{2}(1+\Lambda^{-1})D\Lambda^{-(N-1)/2}\mathcal{H}_N.$$

The prefactor $\Lambda^{(N-1)/2}$ in the expression for $\mathcal{H}_N$ in (2.24) has been introduced so that the smallest hopping is of order 1. Using the recursion relation

$$\mathcal{H}_{N+1} = \Lambda^{1/2}\mathcal{H}_N + \xi_N \left(f^{\dagger}_{N,\sigma} f_{N+1,\sigma} + H.c. \right), \tag{2.25}$$

one can build up the chain by adding one site at a time. Such a procedure can be justified because the energy scales that are brought in by the new site are of order $\Lambda^{1/2}$ smaller than the smallest energy scales of the previous chain. The addition is therefore understood as a perturbation and one hopes to be able to follow the low-energy physics using such a procedure.

2.6.4 Implementation

In a practical implementation, one starts by computing the eigenvalues and eigenvectors of $\mathcal{H}_0$ as well as the matrix elements of the operators $f^{\dagger}_{0,\sigma}$. The Hilbert space is then increased by adding the states of an additional site. The Hamiltonian $\mathcal{H}_1$ is diagonalized using the recursion (2.25) and the operators $f^{\dagger}_{1,\sigma}$ are computed. This is repeated until the desired length of the chain is reached. However, one quickly faces a technical difficulty. The Hilbert space grows as 4^N and it becomes rapidly impossible to diagonalize the Hamiltonian. The solution, proposed by Wilson, is to keep, at every step, only the N_k lowest energy states. N_k has to be determined such as to have an affordable computational time. The success of this truncation scheme lies in the exponential falling down of the matrix elements. Finally, it is very important to use all the available symmetries of the problem in order to reduce the computational effort. Typically, spin and isospin symmetries can be implemented.

One of the outcomes of an NRG run, are the eigenvalues of $\mathcal{H}_n$ at each step n. As we have seen earlier, the smallest hopping term in the Hamiltonian is of order 1, for every n. Therefore the eigenvalues at every step are of the same order of magnitude and one can show a plot of these eigenvalues as a function of n. This plot is called a *flow diagram* and we show a typical example in Fig. 2.11.

2.6.5 Fixed Points

The recursion relation (2.25) defines a renormalization group transformation

$$\mathcal{H}_{N+1} = \mathcal{T}[\mathcal{H}_N].$$

As can be seen from Fig. 2.11, there are regions were the spectrum does not change with increasing steps. This indicates the proximity to a fixed point, described by a Hamiltonian satisfying

$$\mathcal{H}^* = \mathcal{T}^2[\mathcal{H}^*],$$

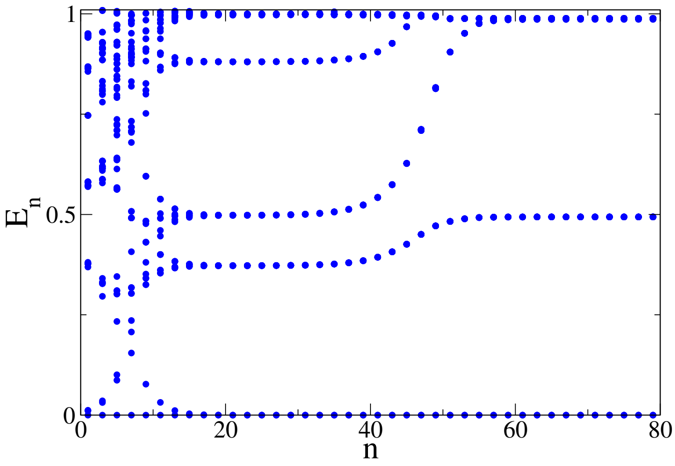

Figure 2.11: Typical flow diagram for an NRG run.

where the square comes from the distinction between odd and even chains. A fixed point has therefore two associated Hamiltonians, one corresponding to an even chain, and one corresponding to an odd chain. An important property of the fixed points is that they describe a theory which is scale invariant. Indeed, the low-energy spectrum is invariant and depends only on one scale that can be thought of as the length of the chain. The renormalization transformation $\mathcal{T}$ adds in new degrees of freedom, keeping the length of the chain fixed. Further applying $\mathcal{T}$, one reaches the continuous limit (corresponding to $\Lambda = 1$). Hence, there is a continuous field theory which describes the physics of the fixed point. Actually, the corresponding field theory has more than just scale invariance, it is conformally invariant. This important property will prove very useful in understanding the fixed point properties as it allows to use the tools of conformal field theory (see Section 2.7).

2.6.6 Spectral Function

The early applications of the NRG approach were restricted to the calculation of static properties, like the specific heat or the magnetic susceptibility. The increase of computational resources made it possible to compute dynamical quantities as well. In particular, we will be interested in the single-particle spectral function of the impurity. As the calculations are made with a discrete version of the conduction band, the spectral function is given by a set of δ-peaks. For a chain made of N sites it is given by

$$A(\omega) = \frac{1}{Z_N} \sum_{nm} \left| \langle n | d_\sigma^\dagger | m \rangle \right|^2 \delta(\omega - (E_n - E_m)) \left(e^{-\beta E_n} + e^{-\beta E_m} \right) ,$$

where Z_N is the grand canonical partition function. Ideally, one should do this computation for a large N where the low-energy fixed point has been reached. However, because of the truncation procedure, at that iteration, the information about the high-energy spectrum is completely lost. In order to get the spectral information at all energy scales, one must compute the spectral function at every iteration and combine [21, 33, 38, 101] it together. The continuous version of this discrete set is finally obtained by broadening the δ-peaks with Gaussians on a logarithmic scale

$$\delta(\omega - \tilde{\omega}) \to \frac{e^{-b^2/4}}{b\,\tilde{\omega}\sqrt{\pi}} \exp\left[-\frac{(\ln\omega - \ln\tilde{\omega})^2}{b^2}\right],$$

where b is the broadening parameter and takes a typical value of 0.5.

2.7 Conformal Field Theory

Over the past 20 years, the methods of conformal field theory have received significant interest in statistical and condensed matter physics [17, 35]. In statistical physics, they have allowed to study critical points in the phase diagram of two-dimensional classical models like the Ising or the three-state Potts model. Quantum mechanical models for which conformal field theory can be used are one-dimensional critical systems, like the spin-1/2 Heisenberg chain. A common feature of all these models is that they have a diverging correlation length so that there is no microscopic characteristic length entering their low-energy description. For statistical systems this means that the lattice spacing does not enter the low-energy physics. In critical quantum systems, instead, this is directly related to the presence of gapless excitations. Indeed, a gap would introduce a microscopic length given by the associated Compton wavelength. The absence of microscopic length endows these systems with scale invariance, but they actually often possess a larger symmetry: They are *conformally invariant*. As a result, they can be described by an effective $(1+1)$-dimensional quantum field theory which is invariant under conformal transformations.

In the beginning of the '90s, Affleck and Ludwig [1] have shown that the techniques of conformal field theory can also be applied to impurity problems. As we have seen in Section 2.6 for the Anderson model, these problems can be mapped onto a semi-infinite chain. Their corresponding field theory is therefore defined on part of a $(1+1)$-dimensional space-time plane. The impurity is sitting at the space coordinate $x = 0$ and the problem is formulated for $x \geq 0$. Far from the impurity, the theory must be that of free fermions and should be scale invariant. Indeed, the impurity can not open a bulk gap so that the theory remains gapless. In fact, the theory should be invariant under the conformal transformations that leave the $x = 0$ line fixed. Affleck and Ludwig argued that it is then natural to assume that the critical properties are described by the free bulk theory with some scale-invariant boundary condition replacing the dynamical impurity. The different regimes (or fixed-points) of the impurity model correspond to different boundary conditions. Note that in some particular cases, like in the Kondo model of a spin-1/2 connected to a single conduction band, these boundaries are equivalent to imposing specific boundary conditions on the fermionic fields, but this is not true in general.

The extension of conformal field theory to account for the presence of a boundary has been developed by Cardy [27, 30] and has provided important results that can used for the study of impurity models. Let us briefly review them here.

2.7.1 Boundary Conformal Field Theory

When boundaries are absent, conformal transformations correspond to transformations $z \to w(z)$, where $z = t + ix$ is the space-time coordinate on the complex plane and w is any analytical function. Expanded about the origin,

$$w(z) = \sum_{n=0}^{\infty} a_n \, z^n,$$

so that there is an infinite number of generators of conformal transformations. This is actually why conformal invariance is so powerful in two dimensions (in dimension bigger than two, the group of conformal transformations is isomorphic to $SL(2, \mathbb{C})$ and therefore finite dimensional). With a boundary along the real axis, the requirement that the transformations leave the boundary fixed yields $w(t) = w^*(t)$, or equivalently $a_n = a_n^*$. The number of generators is reduced by two but is still infinite, though, and the boundary conformal symmetry remains very powerful.

Let us consider a problem defined on a cylinder of length L in the space direction x and of circumference β in the imaginary-time t direction. This would correspond to a quantum mechanical system at temperature $1/\beta$. The ends of the cylinder have a boundary A at $x = 0$ and B at $x = L$, see left panel of Fig. 2.12. We assume that at the boundaries the holomorphic and the anti-holomorphic part of the energy-momentum tensor are equal

$$T(t - ix) = \bar{T}(t + ix), \qquad x = 0, L \tag{2.26}$$

expressing the fact that there is no current flowing through the boundaries. It is then possible to regard $\bar{T}$ as the analytical continuation of T to the negative axis and $x = \pm L$ are identified. The resulting theory is now defined on a torus of length $2L$. It is chiral and has only the symmetry of one of the two Virasoro algebras of the original theory with no boundaries. We note that T is not aware of the boundary condition and the conformal towers of T are not affected. Actually, the boundaries only modify *which conformal towers occur*.

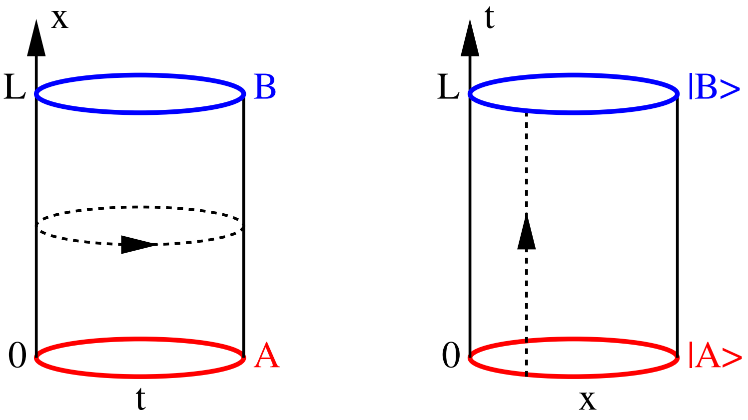

Figure 2.12: Two possible geometries to compute the partition function Z_{AB}. The left geometry has a modular parameter $\tau = i\beta/2L$ whereas on the right $\tau = i2L/\beta$. They are related by a modular transformation $\tau \to -1/\tau$. The dashed lines indicate the direction of the time propagation.

To be more specific, the partition function for this theory is

$$Z_{AB} = \sum_a n^a_{AB} \sum_m e^{-\beta E^a_m(2L)},$$

where n^a_{AB} are non-negative integers giving the multiplicity with which the various conformal towers appear. Only these integers depend on the boundary conditions. The eigenenergy $E^a_m(2L)$ corresponding to the field m with dimension x^a_m in the conformal tower a is given by

$$E^a_m(2L) = \frac{\pi}{L} x^a_m - \frac{\pi c}{24L},$$

where c is the central charge of the theory. Using the definition of the characters

$$\chi_a(q) = q^{-c/24} \sum_m q^{x_m},$$

where $q = e^{2\pi i\tau}$ and τ is the modular parameter, it is possible to write the partition function as

$$Z_{AB} = \sum_a n^a_{AB}\, \chi_a(e^{-\pi\beta/L}). \tag{2.27}$$

This partition function corresponds to $\tau = i\beta/2L$. We emphasize again that the characters do not depend on the boundary conditions, only the n^a_{AB} do. The problem is now to find the multiplicities n^a_{AB} corresponding to all the possible boundary conditions A and B. To make progress, it is useful to compute the partition function in a different way by performing a modular transformation $x \leftrightarrow t$ (i.e. $\tau \to -1/\tau$). Now the original problem that was formulated on a cylinder of time circumference β and space length L is transformed into a cylinder of time length L with antiperiodic conditions along the space direction x, as shown in the right panel of Fig. 2.12. The boundary conditions can be seen as boundary states $|A\rangle$ and $|B\rangle$ that are connected by the evolution operator of a Hamiltonian that we denote by $\tilde{\mathcal{H}}$. In this case, the partition function is

$$Z_{AB} = \langle A|e^{-L\tilde{\mathcal{H}}}|B\rangle. \tag{2.28}$$

Equating this with equation (2.27) will give powerful constraints to determine the possible conformally invariant boundary conditions. The restriction (2.26) implies that the boundary states satisfy

$$\Big[T(x) - \bar{T}(x)\Big]|A\rangle = 0.$$

The most general solution to these constraints is written as

$$|A\rangle = \sum_a \langle a|A\rangle \Big(\sum_m |a,m\rangle \otimes \overline{|a,m\rangle}\Big),$$

where the sum is over so-called Ishibashi [56, 57] states, and $|a,m\rangle$ form a basis for the conformal tower a. The prefactors $\langle a|A\rangle$ are defined by this formula. The partition function (2.28) now reads

$$Z_{AB} = \sum_a \langle A|a\rangle\langle a|B\rangle \sum_m e^{-2LE_m^a(\beta)} = \sum_a \langle A|a\rangle\langle a|B\rangle\, \chi_a(e^{-4L\pi/\beta}).$$

This expression is very close to (2.27) but the characters are not the same. Here, they correspond to a modular parameter $\tau = i2L/\beta$. They are related [29] through the modular transformation $\tau \to -1/\tau$ so that

$$\chi_a(e^{-\pi\beta/L}) = \sum_b \mathcal{S}_a^b\, \chi_b(e^{-4L\pi/\beta}),$$

where $\mathcal{S}$ is the modular $\mathcal{S}$-matrix. Since the two partition functions have to be the same for all β/L we find Cardy's formula

$$\sum_b n_{AB}^b\, \mathcal{S}_b^a = \langle A|a\rangle\langle a|B\rangle. \tag{2.29}$$

This formula relates the occurrence of the conformal towers with the boundary states A and B. In general, it is possible to identify some trivial boundaries and new boundary states can then be obtained by *fusion*. Imagine we fuse all the conformal towers of the theory with boundaries A, B with a tower c and let us show that the resulting theory can be described by new boundaries A, C. In other words, the fusion with c replaces the boundary B by C. Clearly, the new towers appear according to

$$n_{AC}^{a} = \sum_{d} N_{dc}^{a} n_{AB}^{d}, \tag{2.30}$$

where N_{dc}^{a} are the fusion coefficients. The boundary state $|C\rangle$ then needs to have the following coefficients in its expansion in Ishibashi states

$$\langle a|C\rangle = \frac{\mathcal{S}_{c}^{a}}{\mathcal{S}_{0}^{a}} \langle a|B\rangle. \tag{2.31}$$

Indeed, with this definition, we have that the boundary state $|C\rangle$ and n_{AC}^{a} satisfy Cardy's relation (2.29)

$$\begin{aligned} \sum_{b} n_{AC}^{b} \mathcal{S}_{b}^{a} &= \sum_{b,d} N_{dc}^{b} \mathcal{S}_{b}^{a} n_{AB}^{d} = \sum_{d} \frac{\mathcal{S}_{d}^{a} \mathcal{S}_{c}^{a}}{\mathcal{S}_{0}^{a}} n_{AB}^{d} \\ &= \frac{\mathcal{S}_{c}^{a}}{\mathcal{S}_{0}^{a}} \langle A|a\rangle \langle a|B\rangle = \langle A|a\rangle \langle a|C\rangle, \end{aligned}$$

where we used the Verlinde formula [107] in the second equality. This is the main result of this section. It shows that the fusion hypothesis originally proposed by Affleck and Ludwig finds a very natural interpretation within the framework of boundary conformal field theory. The fusion with a conformal tower c reshuffles the towers according to (2.30) and the new boundary state has coefficients given by (2.31). Starting from appropriate known boundaries, it is believed that a complete set of boundary states will be generated.

Let us also mention that it is possible to find the allowed boundary operators that are compatible with a boundary C. Indeed, there is a correspondence between the scaling dimensions of the boundary operators and the conformal towers that appear in the spectrum on a strip with two identical boundaries C [28, 29]. In order to obtain the operator content it is therefore enough to do a double fusion with the tower generating the boundary C. Let us assume we have identified some trivial boundary A and know n_{AA}^{a}. A first fusion with the tower c produces a boundary C and

$$n_{AC}^{a} = \sum_{d} N_{dc}^{a} n_{AA}^{d}.$$

A second fusion then allows to get the boundary operator content for the boundary C. We get

$$n_{CC}^{a} = \sum_{d,b} N_{bc}^{a} N_{dc}^{b} n_{AA}^{d},$$

which tells if there are operators with scaling dimensions corresponding to the conformal tower a.

2.7.2 Ground-State Degeneracy

One-dimensional quantum systems have a universal ground-state degeneracy g which only depends on the boundary conditions [4]. Let us consider a system with boundaries A, B. In general, the logarithm of the partition function for $L \gg \beta$ reads

$$\ln Z_{AB} = \frac{\pi L c}{6\beta} + \ln g + \ldots,$$

where the first term depends on L/β and represents the bulk contribution. Instead, the second term does not scale with the system size and depends on the boundaries: $g = g_A g_B$. If we consider the limit $L \gg \beta$ in the partition function (2.28) we see that only the trivial conformal tower with lowest energy survives

$$\ln Z_{AB} = \frac{\pi L c}{6\beta} + \ln\langle A|0\rangle\langle 0|B\rangle + \ldots.$$

Using Cardy's formula (2.29) the ground-state degeneracy is found to be

$$g = g_A g_B = \langle A|0\rangle\langle 0|B\rangle = \sum_b n^b_{AB}\, \mathcal{S}^0_b. \tag{2.32}$$

Starting from free boundary conditions F for which $g_F = 1$, we can find how g is modified by the introduction of a boundary A after fusion with a conformal tower a

$$g = g_A g_F = \sum_b n^b_{AF}\, \mathcal{S}^0_b = \sum_{b,d} N^b_{da} n^d_{FF} \mathcal{S}^0_b = \sum_d \frac{\mathcal{S}^0_d \mathcal{S}^0_a}{\mathcal{S}^0_0} n^d_{FF} = \frac{\mathcal{S}^0_a}{\mathcal{S}^0_0}.$$

We used (2.32) in the first and last identity, the Verlinde formula in the third equality and (2.30) in the second identity. From this equation it is easy to find the residual entropy of the impurity

$$S(0) = \ln \frac{\mathcal{S}^0_a}{\mathcal{S}^0_0}.$$

2.7.3 Scattering Matrix

In Chapter 4, we will use the one-particle components of the scattering matrix to characterize the different fixed points of the theory. The fermionic fields ψ that describe the electrons on the chain can be expressed as a product of a left-moving part ψ_L (proportional to the holomorphic part of a primary field) and a right-moving part ψ_R (proportional to the anti-holomorphic part of a primary field). In the bulk, we have that the Green's function

$$\langle \psi^\dagger_L(z_1)\, \psi_R(z_2)\rangle = 0.$$

However, as z_1 and z_2 get close to the boundary, the two fermionic fields are no longer independent, like the energy-momentum tensor in Section 2.7.1, and they can acquire a non-zero average value

$$\langle \psi_L^\dagger(z_1)\, \psi_R(z_2) \rangle = \langle \psi_L^\dagger(z_1)\, \psi_L(z_2^*) \rangle = \frac{S_1}{z_1 - z_2^*},$$

where S_1 is a one-particle S-matrix element [6]. For a simple periodic boundary condition $S_1 = 1$, whereas for an antiperiodic condition $S_1 = -1$. In general, if $|S_1| = 1$, the boundary conserves the Fermi-liquid properties. Indeed, in this case, there is no multi-particle scattering occurring at the Fermi surface. The boundary corresponds to imposing $\psi_R(z) = e^{2i\delta}\psi_L(z)$ on the fermionic fields and δ is the phase shift. However, it is also possible to have $|S_1| < 1$ which means that there is inelastic scattering at the Fermi surface and Fermi-liquid behavior is lost. Therefore, S_1 indicates if the introduction of the boundary destroys Fermi-liquid behavior.

The actual computation of S_1 can be done using a result by Cardy and Lewellen [31]. If the boundary of the system is A, then the expectation value of two primary fields is given by

$$\langle \phi(z_1)\, \bar{\phi}(z_2) \rangle = \frac{\langle a|A\rangle}{\langle 0|A\rangle} \frac{1}{(z_1 - z_2^*)^{2x_a}},$$

where ϕ are primary fields of dimension x_a and $|a\rangle$ and $|0\rangle$ correspond to the conformal tower a and the identity, respectively. Applying this result to compute the above Green's function, we have

$$S_1 = \frac{\langle f|A\rangle}{\langle 0|A\rangle},$$

where we used f to label the conformal tower corresponding the the fermionic operators ψ. Starting from some reference boundary F, for which $S_1 = S_{\text{free}}$ is known, we can find the new scattering matrix element for a boundary A, obtained by fusion with a tower a, using (2.31)

$$S_1 = S_{\text{free}} \frac{\mathcal{S}_a^f / \mathcal{S}_0^f}{\mathcal{S}_a^0 / \mathcal{S}_0^0}.$$

Chapter 3

Different Bandwidths in the Two-Band Hubbard Model

We investigate the role of the bandwidth difference in the Mott metal-insulator transition of a two-band Hubbard model in the limit of infinite dimensions, by means of a Gutzwiller variational wave function as well as by dynamical mean-field theory. The variational calculation predicts a two-stage quenching of the charge degrees of freedom, in which the narrower band undergoes a Mott transition before the wider one, both in the presence and in the absence of a Hund's exchange coupling. However, this scenario is not fully confirmed by the dynamical mean-field theory calculation, which shows that, although the quasiparticle residue of the narrower band is zero within our numerical accuracy, low-energy spectral weight still exists inside the Mott-Hubbard gap, concentrated into two peaks symmetric around the chemical potential. This spectral weight vanishes only when the wider band ceases to conduct too. Although our results are compatible with several scenarios, e.g., a narrow gap semiconductor or a semimetal, we argue that the most plausible one is that the two peaks coexist with a narrow resonance tied at the chemical potential, with a spectral weight below our numerical accuracy. This quasiparticle resonance is expected to vanish when the wider band undergoes the Mott transition. The work of this chapter has been done in collaboration with M. Fabrizio, F. Becca and M. Capone and is published in Ref. [37].

3.1 Introduction

Unlike in single-band models, the Mott metal-insulator transition (MIT) in multi-orbital strongly correlated systems generically involves other energy scales besides the short-range Coulomb repulsion U and the *bare* electron bandwidth. They include, for instance, the Coulomb exchange J which produces the Hund's rules, any crystal field or Jahn-Teller effect splitting the orbital degeneracy, and possibly bandwidth differences between the orbitals. There are many theoretical works making use of dynamical mean-field theory which analyze the role of the exchange J [50, 64, 96, 99], the crystal field splitting [82], and the Jahn-Teller effect [25, 26, 48, 49, 51]. All these analyses suggest that these perturbations, which have the common feature of splitting multiplets at fixed charge, are amplified near the MIT, leading for instance to an appreciable shift of the transition towards lower U's [50, 64, 96, 99] or to the appearance of anomalous phases just before the MIT [25, 26]. This behavior is not surprising, since the more the electronic motion is slowed down, i.e., the longer the time electrons stay localized around a site, the larger the chance to get advantage of multiplet-splitting mechanisms.

On the contrary, the role of different bandwidths for nearly degenerate orbitals is less predictable, since the Coulomb charge repulsion only depends on the total number of electrons at a given site, while it is not concerned with the orbital they sit in. Recently, this issue has been addressed in a two-band Hubbard model by DMFT, yet leading to controversial results.

Liebsch has argued, on the basis of a DMFT calculation using quantum Monte Carlo at finite temperature and iterated perturbation theory as impurity solvers, that for not too different bandwidths (he used a ratio 2 between the bandwidths) the two orbitals undergo a common MIT at zero temperature [78, 79]. Other recent developments by Koga and coworkers [67], have shown, using exact diagonalization instead of quantum Monte Carlo, that if one considers the full Hund's coupling there are two distinct MITs: There is a first transition at which the orbital with smaller bandwidth becomes insulating, followed at larger values of the interaction by a second transition at which the other orbital ceases to conduct as well. This two-stage quenching of the charge degrees of freedom has been named orbital-selective Mott transition (OSMT) by those authors. Further calculations by Koga and coworkers [66] also indicate that an Ising-like anisotropy (without pair hopping and exchange term) in the Coulomb exchange tends to favor a single transition. This might explain the apparent contradiction between their $T = 0$ exact diagonalization results and Liebsch's quantum Monte Carlo results extrapolated at $T = 0$. Indeed, Liebsch used an Ising-like Hund's coupling to avoid sign problems at low temperatures in the quantum Monte Carlo algorithm.

Although the coexistence of localized f-electrons and itinerant d-electrons is not unusual in rare-earth compounds, the conclusions of Ref. [67] are somewhat surprising in the case of degenerate orbitals. Indeed, the Coulomb exchange-splitting, rather than favoring an OSMT, should naïvely oppose to it, since J competes against the angular momentum quenching due to the different bandwidths.

In this work, we attempt to clarify this issue by means of a variational analysis based on Gutzwiller wave functions, by standard DMFT calculations as well as by an approximate DMFT projective technique. This chapter is organized as follows: In Section 3.2, we introduce the two-band model and discuss general properties. In Section 3.3, we apply a variational technique based on Gutzwiller-type trial wave functions to analyze the ground state of the Hamiltonian. A full DMFT analysis is presented in Section 3.4. As a guide to interpret the DMFT spectral functions, in Section 3.5, we show the density of state obtained by Wilson's numerical renormalization group of the Anderson impurity model onto which the lattice model maps within DMFT. In Section 3.6, we present an approximate DMFT solution obtained by projecting out self-consistently high-energy degrees of freedom, which allow a better low-energy description. Conclusions are drawn in Section 3.7.

3.2 The Model

We consider a two-band Hubbard model at half-filling described by the Hamiltonian

$$\begin{aligned}\mathcal{H} = &- \sum_{\langle i,j\rangle,\sigma} \sum_{a=1}^{2} t_a\, f^\dagger_{i,a\sigma} f_{j,a\sigma} + H.c. \\ &+ \left(\frac{U}{2} + \frac{J}{3}\right) \sum_i \left(n_i - 2\right)^2 + \mathcal{H}_{\text{exch}},\end{aligned} \tag{3.1}$$

where $f^\dagger_{i,a\sigma}$ creates an electron at site i in orbital $a = 1, 2$ with spin σ, $n_{i\,a} = \sum_\sigma f^\dagger_{i,a\sigma} f_{i,a\sigma}$ is the occupation number at site i in orbital a, and $n_i = n_{i\,1} + n_{i\,2}$ is the total occupation number. The explicit expression of the Coulomb exchange $\mathcal{H}_{\text{exch}}$ is

$$\begin{aligned}\mathcal{H}_{\text{exch}} = &\frac{J}{2} \sum_i \left(n_{i\,1} - n_{i\,2}\right)^2 \\ &+ \frac{J}{2} \sum_i \sum_{\sigma,\sigma'} f^\dagger_{i,1\sigma} f^\dagger_{i,1\sigma'} f_{i,2\sigma'} f_{i,2\sigma} + H.c. \\ &+ \frac{J}{2} \sum_{\sigma,\sigma'} f^\dagger_{i,1\sigma} f_{i,2\sigma} f^\dagger_{i,2\sigma'} f_{i,1\sigma'} + (1 \leftrightarrow 2) \\ \equiv &\, 2J \sum_i \left(T^2_{i\,x} + T^2_{i\,z}\right),\end{aligned} \tag{3.2}$$

where

$$T_{i\,\alpha} = \frac{1}{2} \sum_{a,b} \sum_\sigma f^\dagger_{i,a\sigma}\, \tau^\alpha_{ab}\, f_{i,b\sigma} \tag{3.3}$$

are pseudo-spin-1/2 operators, with τ^α the Pauli matrices, $\alpha = x, y, z$. Note that the term $J\sum_i (n_i - 2)^2/3$ in (3.1) has been introduced so that the center of gravity of the electronic configurations at fixed charge n_i does not depend on J and is simply $U\sum_i (n_i - 2)^2/2$. Hereafter, we always take $0 < t_2 \leq t_1$. Let us start by discussing some general properties of this Hamiltonian.

If $U \gg t_1$, the model describes a Mott insulator in which two electrons localize on each site. For $J > 0$, the atomic two-electron ground state is the spin triplet, followed at energy $2J$ by the two degenerate singlets (we drop the site index)

$$\sqrt{\frac{1}{2}}\left(f^\dagger_{1\uparrow}f^\dagger_{2\downarrow} - f^\dagger_{1\downarrow}f^\dagger_{2\uparrow}\right)|0\rangle, \quad \sqrt{\frac{1}{2}}\left(f^\dagger_{1\uparrow}f^\dagger_{1\downarrow} - f^\dagger_{2\uparrow}f^\dagger_{2\downarrow}\right)|0\rangle,$$

and finally at energy $4J$ by the singlet

$$\sqrt{\frac{1}{2}}\left(f^\dagger_{1\uparrow}f^\dagger_{1\downarrow} + f^\dagger_{2\uparrow}f^\dagger_{2\downarrow}\right)|0\rangle.$$

Here $|0\rangle$ is the vacuum state. Hence, the Mott insulator for very large U, specifically $t_1^2/U \ll J$, is effectively a spin-1 Heisenberg model where, at any site, each orbital is occupied by one electron, the two electrons being bound into a spin-triplet configuration. Within the OSMT scenario, below some critical repulsion, defined in the following as U_1, electrons in orbital 1 start moving, while one electron per site remains localized in orbital 2. Only below a lower $U_2 < U_1$, electrons in orbital 2 delocalize too. In this particular example with a half-filled shell, the Coulomb exchange does not conflict with the OSMT, since $\mathcal{H}_{\text{exch}}$ favors single occupancy of each orbital. Yet, one may wonder about the role of the exchange term (3.2) which can transfer electrons from the delocalized orbital to the localized one.

3.3 Gutzwiller Variational Technique

Let us start by a variational analysis of the ground state of the Hamiltonian (3.1). In particular, we are going to use the Gutzwiller variational approach described in Section 2.2, which is one of the simplest ways to include electronic correlations into a many-body wave function. We label the different atomic configurations for the model (3.1) by

$$\begin{aligned}
&|1,+\rangle_\sigma = f^\dagger_{2\sigma}|0\rangle && |2,+\rangle = f^\dagger_{2\uparrow}f^\dagger_{2\downarrow}|0\rangle\\
&|1,-\rangle_\sigma = f^\dagger_{1\sigma}|0\rangle && |2,-\rangle = f^\dagger_{1\uparrow}f^\dagger_{1\downarrow}|0\rangle\\
&|2,0\rangle = \sqrt{\frac{1}{2}}(f^\dagger_{1\uparrow}f^\dagger_{2\downarrow} - f^\dagger_{1\downarrow}f^\dagger_{2\uparrow})|0\rangle && |3,+\rangle_\sigma = f^\dagger_{1\sigma}f^\dagger_{2\uparrow}f^\dagger_{2\downarrow}|0\rangle\\
&|2,1\rangle_{+1} = f^\dagger_{1\uparrow}f^\dagger_{2\uparrow}|0\rangle && |3,-\rangle_\sigma = f^\dagger_{1\uparrow}f^\dagger_{1\downarrow}f^\dagger_{2\sigma}|0\rangle\\
&|2,1\rangle_0 = \sqrt{\frac{1}{2}}(f^\dagger_{1\uparrow}f^\dagger_{2\downarrow} + f^\dagger_{1\downarrow}f^\dagger_{2\uparrow})|0\rangle && |4\rangle = f^\dagger_{1\uparrow}f^\dagger_{1\downarrow}f^\dagger_{2\uparrow}f^\dagger_{2\downarrow}|0\rangle\\
&|2,1\rangle_{-1} = f^\dagger_{1\downarrow}f^\dagger_{2\downarrow}|0\rangle, &&
\end{aligned}$$

where $|0\rangle$ is the vacuum state. Together with these states, we define the associated projectors

$$\begin{aligned}
\mathcal{P}(0) &= |0\rangle\langle 0| & \mathcal{P}(2,+) &= |2+\rangle\langle 2+| \\
\mathcal{P}(1,+) &= \sum_{\sigma} |1+\rangle_{\sigma\sigma}\langle 1+| & \mathcal{P}(2,-) &= |2-\rangle\langle 2-| \\
\mathcal{P}(1,-) &= \sum_{\sigma} |1-\rangle_{\sigma\sigma}\langle 1-| & \mathcal{P}(2,0) &= |2\,0\rangle\langle 2\,0| \\
\mathcal{P}(3,-) &= \sum_{\sigma} |3-\rangle_{\sigma\sigma}\langle 3-| & \mathcal{P}(2,1) &= \sum_{s} |2\,1\rangle_{ss}\langle 2\,1| \\
\mathcal{P}(3,+) &= \sum_{\sigma} |3+\rangle_{\sigma\sigma}\langle 3+| & \mathcal{A}(2,\pm) &= |2+\rangle\langle 2-| \\
\mathcal{P}(4) &= |4\rangle\langle 4| & \mathcal{A}(2,\mp) &= |2-\rangle\langle 2+|. \qquad (3.4)
\end{aligned}$$

It is now possible to rewrite the Hamiltonian (3.1) in terms of these projectors so that it is brought under the form (2.6) that we used in Section 2.2

$$\begin{aligned}
\mathcal{H} = &- \sum_{\langle i,j\rangle,\sigma} \sum_{a=1}^{2} t_a\, f^{\dagger}_{i,a\sigma} f_{j,a\sigma} + H.c. + 2U\Big[\mathcal{P}(0)+\mathcal{P}(4)\Big] \\
&+ \frac{U}{2}\Big[\mathcal{P}(1,+)+\mathcal{P}(1,-)+\mathcal{P}(3,+)+\mathcal{P}(3,-)\Big] + J\Big[\mathcal{A}(2,\pm)+\mathcal{A}(2,\mp)\Big] \\
&+ \frac{2J}{3}\mathcal{P}(2,0) - \frac{4J}{3}\mathcal{P}(2,1) + \frac{5J}{3}\Big[\mathcal{P}(2,-)+\mathcal{P}(2,+)\Big].
\end{aligned} \tag{3.5}$$

The solution of the uncorrelated problem ($U = J = 0$) is the Fermi-sea Slater determinant $|\Psi_0\rangle$. The correlated variational wave function $|\Psi\rangle$ will be constructed from the uncorrelated one by applying a Gutzwiller projector on it. The explicit form of this projector will be shown in the following sections. The kinetic term is diagonal in orbital and spin index which brings in some simplifications. The Fermi sea $|\Psi_0\rangle$ satisfies

$$\begin{aligned}
\langle\Psi_0|f^{\dagger}_{i,a\sigma} f_{j,b\sigma'}|\Psi_0\rangle &= 0 \qquad \text{if} \quad (a,\sigma) \neq (b,\sigma') \\
\langle\Psi_0|f^{\dagger}_{i,a\sigma} f_{i,b\sigma'}|\Psi_0\rangle &= \delta_{\sigma\sigma'}\,\delta_{ab}\,\frac{N}{2k},
\end{aligned}$$

where N is the average occupation per site. Let us denote by roman letters the correlated probabilities $P(n,\Gamma) = \langle\Psi|\mathcal{P}(n,\Gamma)|\Psi\rangle$ and $A(n,\Gamma) = \langle\Psi|\mathcal{A}(n,\Gamma)|\Psi\rangle$. These variables will be used as the variational parameters that have to be tuned to minimize the Gutzwiller energy. Given the particle-hole symmetry of the model, we can identify

$$\begin{aligned}
P(0) &= P(4) & P(1,+) &= P(3,-) \\
P(1,-) &= P(3,+) & P(2,+) &= P(2,-) \\
A(2,\pm) &= A(2,\mp).
\end{aligned}$$

Considering these properties, the variational ground-state energy (2.10) per site takes a simpler form

$$\begin{aligned}E = &-\frac{1}{V}\sum_{\langle i,j\rangle,\sigma\sigma'}\sum_{a,b=1}^{2} t_a\, Z_{a\sigma}^{b\sigma'}\, \langle\Psi_0| f^\dagger_{i,b\sigma'} f_{j,b\sigma'} + H.c.|\Psi_0\rangle + 4U\,P(0)\\ &+ U\left[P(1,+) + P(1,-)\right] + 2J\,A(2,\pm)\\ &+ \frac{2J}{3}P(2,0) - \frac{4J}{3}P(2,1) + \frac{10J}{3}P(2,+),\end{aligned}$$

and the reduction factors $Z_{a\sigma}^{b\sigma'}$ are evaluated through

$$\sqrt{Z_{a\sigma}^{b\sigma'}} = \frac{2k}{N}\langle\Psi_0|\mathcal{P}^\dagger_{i\,G}\, f^\dagger_{i,a\sigma}\, \mathcal{P}_{i\,G}\, f_{i,b\sigma'}|\Psi_0\rangle. \tag{3.6}$$

3.3.1 Results for $J = 0$

Let start with the simpler case where $J = 0$. The Hamiltonian is written in terms of diagonal projectors only. We may therefore write the Gutzwiller projector using the $\mathcal{P}(n,\Gamma)$ given in (3.4)

$$\mathcal{P} = \prod_i \mathcal{P}_{i\,G} = \prod_i \sum_{n,\Gamma} \lambda_{n\Gamma}\mathcal{P}_i(n,\Gamma). \tag{3.7}$$

The states within a spin multiplet are expected to appear with the same probability. This is the motivation for defining projectors like $\mathcal{P}(2,1)$ as a sum of projectors over the different states of the multiplet. Any of these 3 states will have a correlated probability $\frac{1}{3}P(2,1)$. In the limit $d \to \infty$ and when the Gutzwiller projector has only diagonal components it is easy to relate the $\lambda_{n\Gamma}$ to the correlated probabilities $P(n,\Gamma)$

$$\lambda^2_{n\Gamma} = \frac{P(n,\Gamma)}{P^{(0)}(n,\Gamma)},$$

where $P^{(0)}(n,\Gamma)$ is the uncorrelated probability $\langle\Psi_0|\mathcal{P}_i(n,\Gamma)|\Psi_0\rangle$. Clearly every correlated quantity can now be expressed as a function of the $P(n,\Gamma)$. The restriction (2.8) reads

$$\sum_{n\Gamma} P(n,\Gamma) = 1$$

and, because of particle-hole and spin symmetry, all the restrictions (2.9) are diagonal and equivalent and impose that

$$\sum_{n\Gamma} n\,P(n,\Gamma) = N.$$

We will be interested in the half-filled case $N = 2$. After some simple, but lengthy algebra, we find that the hopping energy reduction factors (3.6) are given by $Z_{a\sigma}^{b\sigma'} = \delta_{ab}\delta_{\sigma\sigma'} Z_a$ with

$$\begin{aligned}\sqrt{Z_1} &= 2\sqrt{2}\sqrt{P(0)P(1,-)} + 2\sqrt{2}\sqrt{P(1,-)P(2,+)}\\ &\quad + \sqrt{2}\sqrt{P(1,+)P(2,0)} + \sqrt{6}\sqrt{P(1,+)P(2,1)},\\ \sqrt{Z_2} &= 2\sqrt{2}\sqrt{P(0)P(1,+)} + 2\sqrt{2}\sqrt{P(1,+)P(2,+)}\\ &\quad + \sqrt{2}\sqrt{P(1,-)P(2,0)} + \sqrt{6}\sqrt{P(1,-)P(2,1)}.\end{aligned}$$

Since $J = 0$, the two-electron configurations with one electron in each orbital are equally probable, namely $P(2,1) = 3P(2,0)$. Therefore, one can use the following parametrization

$$\begin{aligned}P(1,+) &= P(1)\,\cos^2\phi,\\ P(1,-) &= P(1)\,\sin^2\phi,\\ P(2,1) &= P(2)\,\frac{3}{4}\,\cos^2\theta,\\ P(2,0) &= P(2)\,\frac{1}{4}\,\cos^2\theta,\\ P(2,+) &= P(2)\,\frac{1}{2}\,\sin^2\theta.\end{aligned}$$

The normalization conditions (2.8) and (2.9) now both read

$$2\,P(0) + 2\,P(1) + P(2) = 1, \tag{3.8}$$

and the Z-reduction factors can be written as

$$\begin{aligned}\sqrt{Z_1} &= 2\sqrt{2}\,\sin\phi\,\sqrt{P(0)P(1)}\\ &\quad + \sqrt{P(1)P(2)}\,\left[2\,\sin\phi\,\sin\theta + \sqrt{8}\,\cos\phi\,\cos\theta\right],\\ \sqrt{Z_2} &= 2\sqrt{2}\,\cos\phi\,\sqrt{P(0)P(1)}\\ &\quad + \sqrt{P(1)P(2)}\,\left[2\,\cos\phi\,\sin\theta + \sqrt{8}\,\sin\phi\,\cos\theta\right].\end{aligned}$$

If we define

$$\begin{aligned}T &= \frac{1}{V}\langle\Psi_0|\sum_{\langle i,j\rangle,\sigma} f^\dagger_{i,1\sigma} f_{j,1\sigma} + H.c.|\Psi_0\rangle\\ &= \frac{1}{V}\langle\Psi_0|\sum_{\langle i,j\rangle,\sigma} f^\dagger_{i,2\sigma} f_{j,2\sigma} + H.c.|\Psi_0\rangle,\end{aligned}$$

the average value per site of the hopping operator in the Fermi sea, then the variational energy of the Gutzwiller wave function in infinite dimensions is

$$E = -t_1\,T\,Z_1 - t_2\,T\,Z_2 + U\,P(1) + 4\,U\,P(0). \tag{3.9}$$

Here, the Z_i are functionals of the probability distribution $P(n)$, $n = 0, 1, 2$, with the normalization (3.8), as well as of the two angles $\phi, \theta \in [0, \pi/2]$.

One can proceed analytically a bit further. It is known [13] that near a Mott transition and within the Gutzwiller wave function approach, one can safely neglect $P(0) = P(4)$. Within this approximation, $P(2) = 1 - 2\,P(1)$ and

$$\sqrt{Z_1} = \sqrt{P(1)P(2)}\,\left[2\,\sin\phi\,\sin\theta + \sqrt{8}\,\cos\phi\,\cos\theta\right],$$
$$\sqrt{Z_2} = \sqrt{P(1)P(2)}\,\left[2\,\cos\phi\,\sin\theta + \sqrt{8}\,\sin\phi\,\cos\theta\right].$$

We denote $P(1) = d/2$, hence $P(2) = 1 - d$, so that the variational energy (3.9) becomes

$$E = -T\,\frac{d\,(1-d)}{2}\,f(\phi,\theta) + \frac{U}{2}\,d$$

where

$$f(\phi,\theta) = t_1\,\left[2\,\sin\phi\,\sin\theta + \sqrt{8}\,\cos\phi\,\cos\theta\right]^2 + t_2\,\left[2\,\cos\phi\,\sin\theta + \sqrt{8}\,\sin\phi\,\cos\theta\right]^2.$$

The optimal value for d is

$$d_* = \frac{T\,f(\phi,\theta) - U}{2\,T\,f(\phi,\theta)},$$

and the variational energy becomes:

$$E[\phi,\theta] = -\frac{[T\,f(\phi,\theta) - U]^2}{8\,T\,f(\phi,\theta)}.$$

At given ϕ and θ, the Mott transition at which both orbitals localize occurs when $d_* = 0$, namely when

$$U_c(\phi,\theta) = T\,f(\phi,\theta).$$

The most stable solution is the one which maximizes f. An OSMT corresponds to a situation in which the Mott transition occurs with orbital 2 being already strictly singly-occupied, namely with $\phi = \theta = 0$. This solution is an extremum of f. Yet, one has to check whether it is also a maximum. We find that this is indeed the case whenever

$$t_2 \le \frac{1}{5}\,t_1. \tag{3.10}$$

Therefore, within the Gutzwiller variational technique, an OSMT can occur even in the absence of Coulomb exchange, provided (3.10) is satisfied.

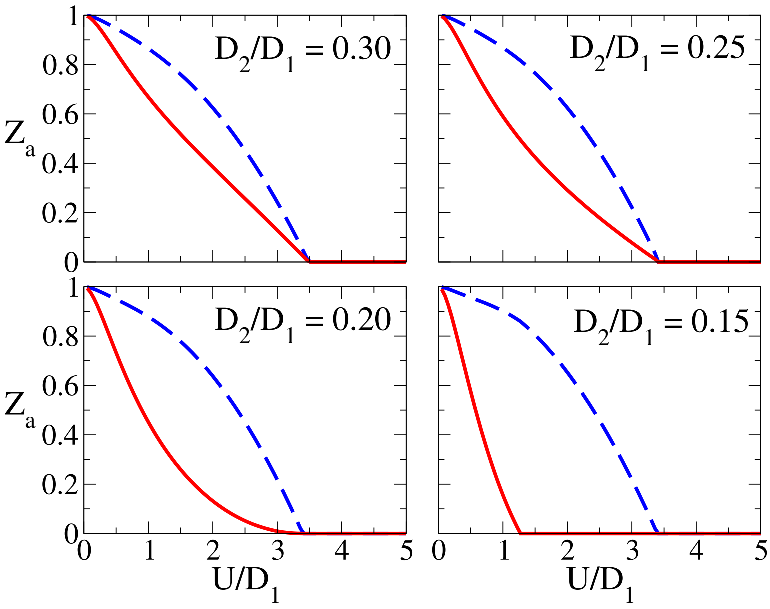

Figure 3.1: Reduction factors Z_a for the wide band (dashed line) and for the narrow band (continuous line) obtained with the Gutzwiller wave function for different ratios of the bandwidth D_2/D_1 and $J = 0$.

We optimized (3.9) numerically, considering an infinite coordination Bethe lattice at half-filling. The free density of state is given by

$$\rho_a(\epsilon) = \frac{\sqrt{4t_a^2 - \epsilon^2}}{2\pi t_a^2}, \tag{3.11}$$

and, in this case, $T = 8/(3\pi)$. The half-bandwidth of each band is $D_a = 2t_a$, and our unit of energy is D_1. The reduction factors Z_1 and Z_2 are shown in Fig. 3.1, for different ratios D_2/D_1. The results indeed confirm the analytical calculation (3.10), displaying two distinct transitions when $D_2/D_1 < 0.20$. Moreover, the transitions are of second order both if an OSMT occurs or not.

3.3.2 Results for $J \neq 0$

Let us now move to the more complicated case of $J \neq 0$. As can be seen from (3.5), the Hund's rule coupling acts only within the two-electron configurations and is not diagonal in the representation which we have used so far. As a consequence, we generalize the Gutzwiller correlator (3.7) into

$$\mathcal{P}_{iG} \to \mathcal{P}_{iG} + \lambda_{2\perp}\left(\mathcal{A}(2,\pm) + \mathcal{A}(2,\mp)\right).$$

We can still relate the $\lambda_{n\Gamma}$ to the correlated probabilities using

$$\begin{aligned}P(2,+) &= \lambda_{2+}^2\, P^{(0)}(2,+) + \lambda_{2\perp}^2\, P^{(0)}(2,-),\\ P(2,-) &= \lambda_{2-}^2\, P^{(0)}(2,-) + \lambda_{2\perp}^2\, P^{(0)}(2,+).\end{aligned}$$

Since by particle-hole symmetry $P(2,+) = P(2,-)$, as well as $P^{(0)}(2,+) = P^{(0)}(2,-)$, then $\lambda_{2+} = \lambda_{2-} \equiv \lambda_{2\pm}$ and hence

$$\lambda_{2\pm}^2 + \lambda_{2\perp}^2 = \frac{P(2,+)}{P^{(0)}(2,+)}.$$

In addition,

$$A(2,\pm) = 2\,\lambda_{2\perp}\,\lambda_{2\pm}\,P^{(0)}(2,+),$$

so that

$$\begin{aligned}\lambda_{2\pm} &= \frac{1}{2\sqrt{P^{(0)}(2,+)}}\left[\sqrt{P(2,+)+A(2,\pm)} + \sqrt{P(2,+)-A(2,\pm)}\right],\\ \lambda_{2\perp} &= \frac{1}{2\sqrt{P^{(0)}(2,+)}}\left[\sqrt{P(2,+)+A(2,\pm)} - \sqrt{P(2,+)-A(2,\pm)}\right].\end{aligned}$$

We notice that $|A(2,\pm)| \leq P(2,+)$. The hopping reduction factors (3.6) are now modified into $Z_{a\sigma}^{b\sigma'} = \delta_{ab}\delta_{\sigma\sigma'}Z_a$ with

$$\begin{aligned}\sqrt{Z_1} = 2\sqrt{2}\,&\sqrt{P(0)P(1,-)}\\ &+\sqrt{2}\,\sqrt{P(1,-)}\left[\sqrt{P(2,+)+A(2,\pm)} + \sqrt{P(2,+)-A(2,\pm)}\right]\\ &+\sqrt{2}\,\sqrt{P(1,+)P(2,0)} + \sqrt{6}\,\sqrt{P(1,+)P(2,1)},\\ \sqrt{Z_2} = 2\sqrt{2}\,&\sqrt{P(0)P(1,+)}\\ &+\sqrt{2}\,\sqrt{P(1,+)}\left[\sqrt{P(2,+)+A(2,\pm)} + \sqrt{P(2,+)-A(2,\pm)}\right]\\ &+\sqrt{2}\,\sqrt{P(1,-)P(2,0)} + \sqrt{6}\,\sqrt{P(1,-)P(2,1)}.\end{aligned}$$

The average value of the Hund's coupling is

$$E_J = 2J\,A(2,\pm) + \frac{2J}{3}P(2,0) - \frac{4J}{3}P(2,1) + \frac{10J}{3}P(2,+),$$

and that of the Hubbard repulsion

$$E_U = 4U\,P(0) + U\left[P(1,+) + P(1,-)\right].$$

Thus, the variational energy to be minimized is

$$E = -t_1\,T\,Z_1 - t_2\,T\,Z_2 + E_J + E_U. \tag{3.12}$$

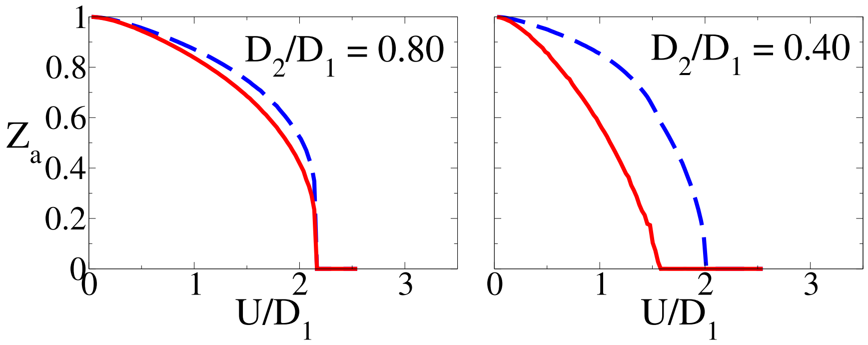

Figure 3.2: Reduction factors Z_a for the wide band (dashed line) and the narrow band (continuous line) obtained with the Gutzwiller wave function for different ratios of the bandwidth D_2/D_1 and $J/U = 0.10$.

With the modified Gutzwiller projector, the restrictions (2.8) and (2.9) still read

$$2P(0) + 2\,P(1) + P(2) = 1,$$

where $P(n) = \sum_\Gamma P(n,\Gamma)$. By the numerical minimization of the variational energy, we find that the critical ratio D_2/D_1 for an OSMT increases when $J \neq 0$ from the value 0.2 found for $J = 0$. In Fig. 3.2, we show Z_1 and Z_2 as obtained by numerical minimization of (3.12), for two ratios of D_2/D_1 and $J/U = 0.10$. Additional calculations allowed to draw the phase diagram within the Gutzwiller variational approach, see the left panel of Fig. 3.3. As is apparent from the inset, the introduction of the Hund's coupling increases the value of the critical ratio D_2/D_1. The right panel of Fig. 3.3 shows how the phase diagram is modified as J/U is increased. It is clear that both U_2, after which the OSMT is observed, and U_1 where the complete Mott transition takes place, decrease with increasing J, going to zero as J goes to infinity. We also notice that the Mott transition at which only one band localizes is second order while the the transition to the complete insulator is first order. This is different from the case $J = 0$ where both transitions are second order and might be a pathology of the Gutzwiller wave function [13].

In conclusion, we find that the Gutzwiller variational technique predicts an OSMT both for $J = 0$ and $J \neq 0$, provided that D_1/D_2 is smaller than a critical value which increases with J.

3.4 Dynamical Mean-Field Theory

To have further insights into the quality of the Gutzwiller wave function in infinite dimensions, we have performed an extensive DMFT calculation (see Section 2.3) for the same Hamiltonian. For simplicity, we consider an infinite

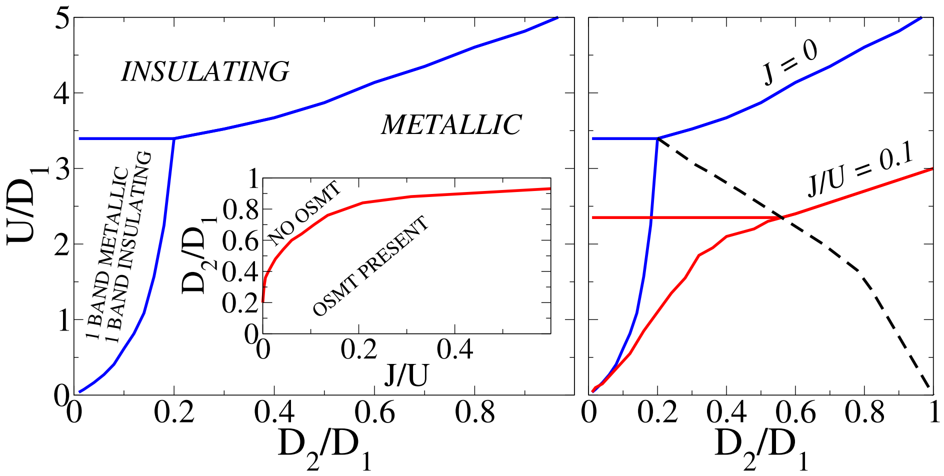

Figure 3.3: Left: Phase diagram obtained within the Gutzwiller approximation in the absence of the Hund's coupling. Inset: the critical ratio D_2/D_1 below which an OSMT is observed as a function of J/U. Right: Modification of the phase diagram as J/U is increased. The dashed line shows when the OSMT starts appearing.

coordination Bethe lattice, as in the Gutzwiller variational approach, with a bare density of states given by (3.11). Again, $D_a = 2t_a$ is the half-bandwidth of band a. The Anderson impurity model onto which the lattice model maps within DMFT is

$$\begin{aligned}\mathcal{H}_{\mathrm{AM}} &= \sum_{k,a,\sigma} \epsilon_{ka} c^\dagger_{ka\sigma} c_{ka\sigma} + \sum_{k,a,\sigma} V_{ka}\left(f^\dagger_{a\sigma} c_{ka\sigma} + H.c.\right) \\ &+ \left(\frac{U}{2} + \frac{J}{3}\right)(n_f - 2)^2 + 2J\left(T_x^2 + T_z^2\right), \qquad (3.13)\end{aligned}$$

where T_α, $\alpha = x, y, z$, are the pseudo-spin operators (3.3) for the impurity. The self-consistency condition relates the impurity Green's function for orbital a, G_a, to the parameters ϵ_{ka} and V_{ka} through

$$t_a^2 G_a(i\omega_n) = \sum_k \frac{V_{ka}^2}{i\omega_n - \epsilon_{ka}}. \qquad (3.14)$$

We solve the Anderson impurity model using an exact diagonalization method [24] at zero temperature. The continuous conduction-electron bath is modeled by a finite number of parameters ϵ_{ka} and V_{ka} ($k = 1, \ldots, n_s - 1$). In our calculations, we considered $n_s = 6$ and 4 (not shown). The self-consistency (3.14) is implemented through a fitting procedure along the imaginary axis. To this end, we discretize the axis into Matsubara frequencies $\omega_n = (2n+1)\pi/\beta$, where β is a fictitious temperature that we have set to

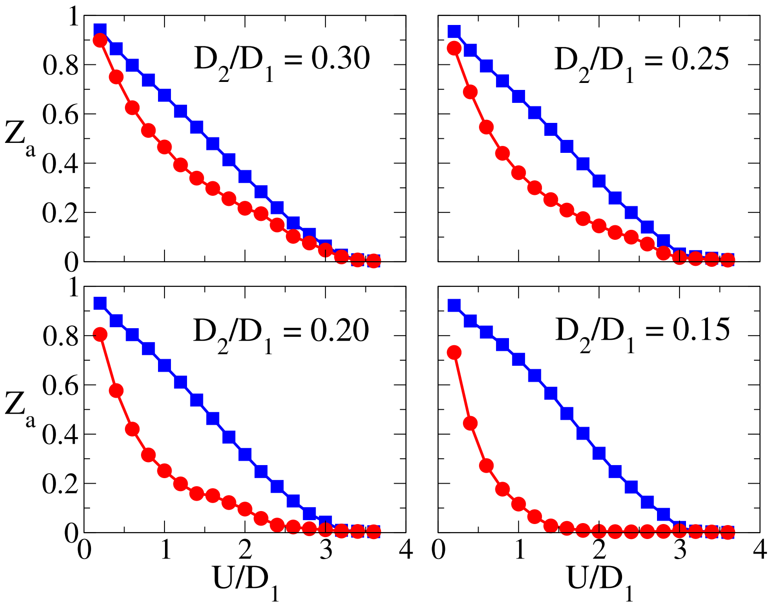

Figure 3.4: Quasiparticle residues Z_a for the wide band (squares) and for the narrow band (circles) obtained by the DMFT calculation for different ratios of the bandwidth D_2/D_1 and $J = 0$.

$\beta = 500/D_1$. Moreover, the smallest frequency ω_{min} has been determined by the smallest pole in the continued fraction expansion of the Green's function [90]. Frequencies below ω_{min} are not taken into account in the fitting. Note that this procedure sometimes leads to different minimum cutoff frequencies for the two bands. In the following, we will work in units of D_1.

First, we treat the $J = 0$ case in which there is no Hund's coupling. The metallic or insulating nature of each band is characterized by its quasiparticle residue $Z_a^{-1} = 1 - (\partial \mathrm{Im}\Sigma_a(i\omega)/\partial i\omega)\,|_{\omega\to 0}$. In Fig. 3.4, we show Z_a as a function of the Coulomb repulsion U for different bandwidth ratios D_2/D_1. When the ratio of the bandwidth $D_2/D_1 \geq 0.20$, the quasiparticle weights decrease as the Coulomb interaction gets bigger. Even though there is a stronger initial reduction for the narrow band, the weights eventually vanish for the same critical value of $U_c/D_1 \simeq 3.6$. The situation changes when we further decrease the bandwidth ratio (i.e., $D_2/D_1 = 0.15$). In this case, we find that the weights of the bands vanish for different values of U, in agreement with the results of the Gutzwiller wave function. Moreover, the critical ratio $D_2/D_1 = 0.20$ that we found earlier seems consistent with the DMFT calculation.

Let us turn now to the model in the presence of a finite Hund's coupling, $J/U = 0.10$, and perform the same calculations for the following ratios of

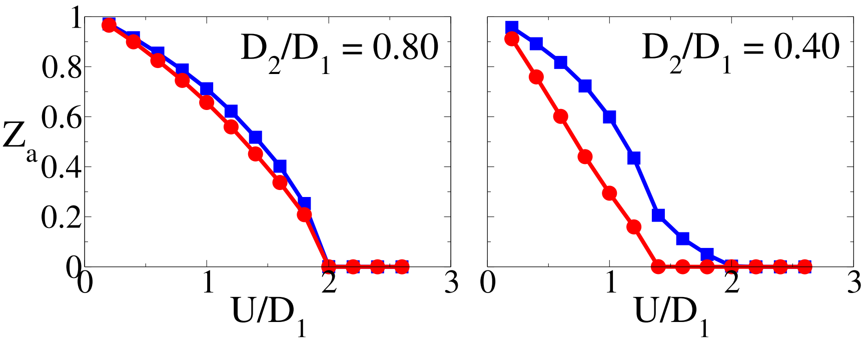

Figure 3.5: Quasiparticle residues Z_a for the wide band (squares) and the narrow band (circles) obtained by the DMFT calculation for different ratios of the bandwidth D_2/D_1 and $J/U = 0.10$.

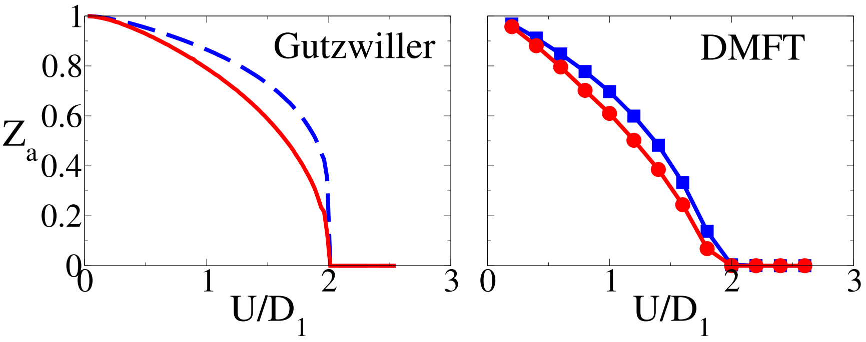

Figure 3.6: Quasiparticle residues Z_a obtained with the Gutzwiller wave function (wide band: dashed line, narrow band: continuous line) and by DMFT (wide band: squares, narrow band: circles) for the critical ratio of the bandwidth $D_2/D_1 = 0.66$ and $J/U = 0.10$.

the bandwidths: $D_2/D_1 = 0.80$ and 0.40. The results are shown in Fig. 3.5. We still find evidences for an OSMT, this time, however, below a larger ratio of the bandwidths. Further calculations show that the critical ratio of the bandwidth for $J/U = 0.10$ is $D_2/D_1 \sim 0.66$. That is also what one finds within the Gutzwiller approximation. In Fig. 3.6, we plot the outcome obtained by Gutzwiller and DMFT for $D_2/D_1 = 0.66$. Again, the two results agree rather well and display a similar critical $U \sim 2D_1$.

If we were to confine our analysis to the behavior of the quasiparticle residues Z_a, we should conclude that, both in the absence and in the presence of a Hund's coupling, the OSMT scenario does occur for a sufficiently small ratio of the bandwidths, in qualitative and also quantitative agreement with the variational results of the Gutzwiller wave function. The only difference

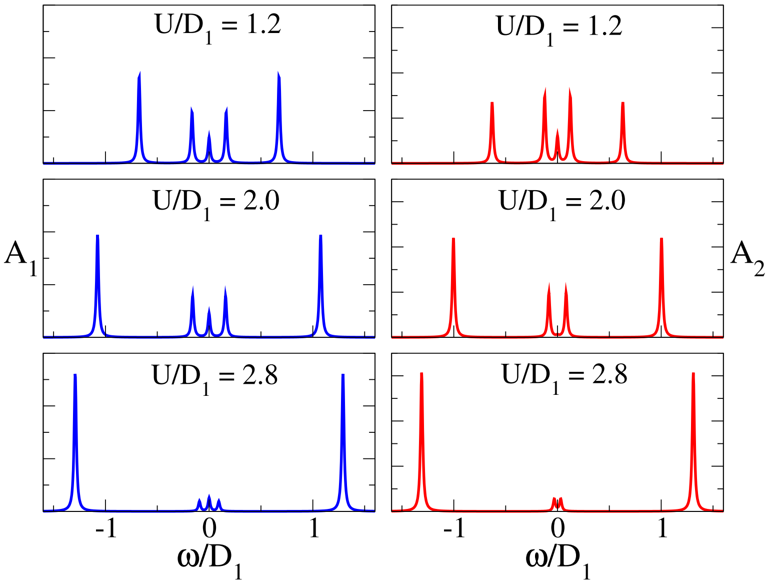

Figure 3.7: Density of states for the wide band (left panels) and the narrow band (right panels) as obtained by DMFT for different values of the Coulomb interaction. The ratio of the bandwidth is $D_2/D_1 = 0.15$ and $J = 0$.

may lie in the order of the transition. Even if it is difficult to settle precisely the order of the transition with exact diagonalization calculations, our results seem to point towards a second-order phase transition at the MIT U_1 with finite J, contrary to the first-order transition predicted by the Gutzwiller wave function.

A deeper insight into the above scenario can be gained by analyzing the spectral properties of the more correlated band, and not just its quasiparticle residue. Indeed, such an inspection leads to a less clear-cut picture, revealing features which are not captured by the Gutzwiller wave function. In Fig. 3.7, we show the density of states (DOS) of both orbitals for various Hubbard U's and $D_2/D_1 = 0.15$. We notice that, although the DOS of the narrow band right at the chemical potential becomes zero within our numerical accuracy above U_2, there is still low-energy spectral weight inside the Mott-Hubbard gap. Due to our discretization procedure, this weight is concentrated in two peaks located symmetrically with respect to the chemical potential. These peaks are also present at $J = 0$, and move linearly away from the chemical potential when $J \neq 0$, roughly as $2J$, see Fig. 3.8. Their total spectral weight scales approximately like the quasiparticle residue of the wider band, Z_1, both vanishing at the second MIT, U_1. In addition, if $J = 0$, the distance between the peaks also scales like Z_1, see Fig. 3.7. If we, reasonably, assume that

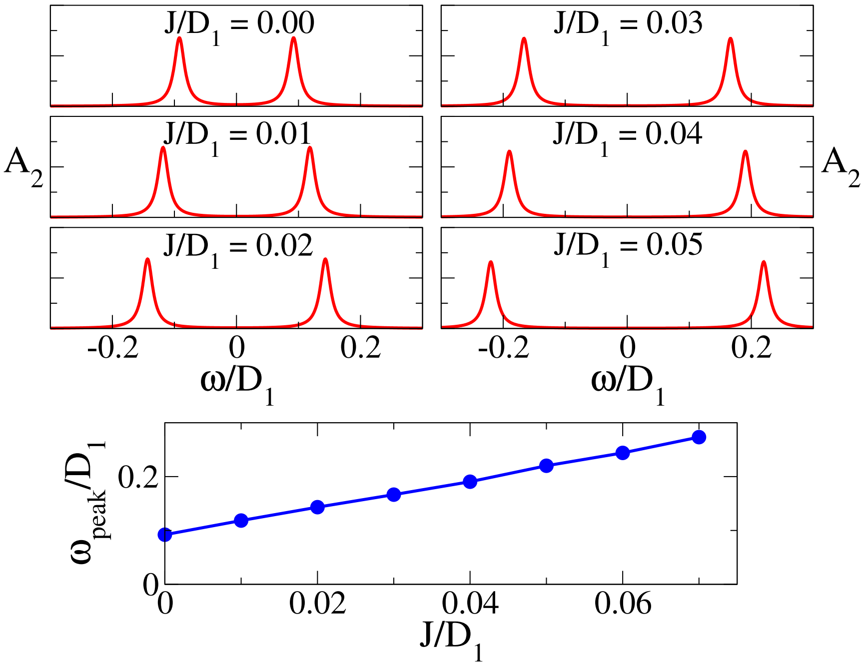

Figure 3.8: Upper panels: low-energy part of the density of states of the narrow band as obtained by DMFT for different values of J/D_1. The ratio of the bandwidths is $D_2/D_1 = 0.15$, and the Coulomb repulsion is set to $U/D_1 = 2$. Lower panel: position of the low-energy peaks as a function of J/D_1.

these two peaks mimic two resonances, one below and the other above the chemical potential, it becomes much less obvious what might be the actual value of the DOS right at the chemical potential if we were not constrained to a small number of levels. Moreover, even if the DOS were strictly zero at the chemical potential, still we should determine whether band 2 behaves like a small-gap semiconductor or a semimetal for $U_2 \leq U \leq U_1$. In other words, the energy discretization inherent in the exact diagonalization technique might play a more critical role in this case than in the simplest single-band Hubbard model.

Therefore, although the numerical evidences we have presented so far point in favor of the existence of an OSMT with zero or finite J below a critical bandwidth ratio, there are several aspects which still need to be clarified. We will consider a deeper investigation of such aspects in the following sections.

3.5 Single Impurity Spectral Properties

The first issue we want to address concerns the origin of the two peaks in the orbital 2 spectral function inside the Mott-Hubbard gap. The self-consistency condition (3.14) of the effective Anderson impurity model (3.13) plays a very crucial role, for instance it determines a critical value of U above which the Kondo effect does not take place anymore. Yet, useful information can be obtained by studying (3.13) without imposing (3.14), which is what we are going to do in this section by means of Wilson's numerical renormalization group (see Section 2.6).

The Anderson impurity model (3.13) is controlled by several energy scales, the Hubbard U, the Hund's coupling J and the so-called hybridization widths

$$\Gamma_a = \sum_k V_{ka}^2 \, \delta\left(\epsilon_{ka}\right) .$$

For simplicity, we will assume that the two conduction baths are degenerate with half-bandwidth D, which will be our unit of energy. In Fig. 3.9, we show the impurity spectral function of the orbital 2, $A_2(\omega)$, as obtained by NRG for $J = 0$, $U = 2D$, $\Gamma_1 = D/(2\pi)$, and for several values of $\Gamma_2/\Gamma_1 < 1$. Since we do not impose any self-consistency, the DOS for any $\Gamma_2 \neq 0$ shows a Kondo resonance at the chemical potential, which narrows as Γ_2 decreases. In addition, there are two more peaks which move slightly away from the chemical potential as Γ_2 is reduced. These peaks actually resemble those we find in the DMFT calculation. Indeed, they move linearly as we switch on J, see Fig. 3.10, just like we observe within DMFT.

The origin of these peaks is easy to identify when $\Gamma_2 = 0$. When the orbital 2 is not hybridized with its bath, its occupation number n_2 is a conserved quantity. The ground state is expected to belong to the subspace with $n_2 = 1$, because, in this case, $\langle n_1 \rangle = 1$ and the Kondo-screening energy gain is maximum. This state is twofold degenerate reflecting the free spin-1/2 of the electron localized in orbital 2. The energy gap to the lowest energy states for $n_2 = 0, 2$, $\langle n_1 \rangle = 2, 0$, respectively, is therefore of the order of the Kondo temperature of orbital 1, $T_{K\,1}$. The DOS of the impurity orbital 2 is analogous to the core-hole spectral function in X-ray absorption, so it should start above a finite threshold proportional to $T_{K\,1}$. In other words, the DOS has a small but finite gap of order $T_{K\,1}$, similar to what we observe within DMFT.

However, as soon as Γ_2 is non zero, this gap is filled and, in addition, a Kondo-resonance appears. Even if we move the peaks away from the chemical potential by increasing J, see Fig. 3.10, the region between them and the narrow (practically invisible in the figure) Kondo-resonance is still covered by spectral weight. In the light of this dynamical behavior, it is not at all obvious what the self-consistency requirement (3.14) may lead to when band-1 is still conducting. In other words, either a true narrow gap, as if $\Gamma_2 = 0$, or a pseudo-gap with a power-law vanishing DOS, or two-peaks plus the narrow

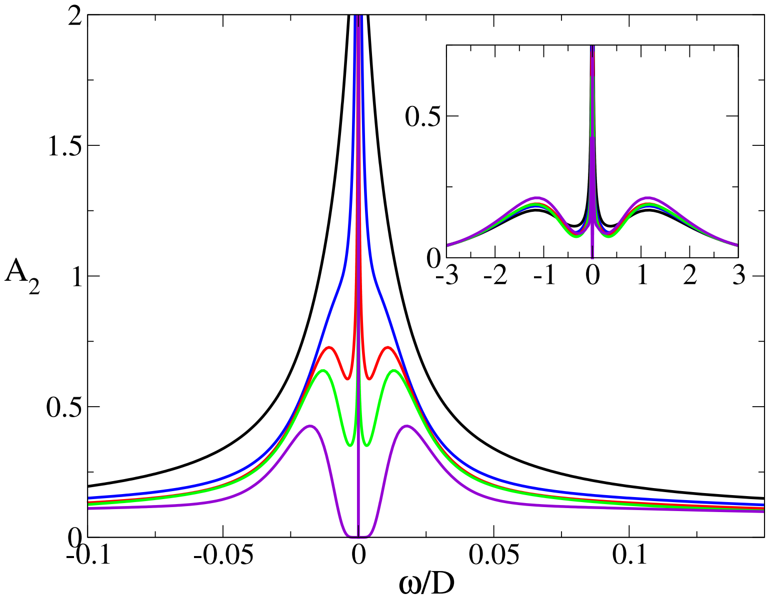

Figure 3.9: Spectral function $A_2(\omega)$ of the narrow band for $J = 0$, $U/D = 2$, $\Gamma_1 = D/2\pi$, and $\Gamma_2/\Gamma_1 = \frac{1}{2}, \frac{1}{4}, \frac{1}{6}, \frac{1}{8}, 0$ (from top to bottom). Inset: the same spectral function on a wider scale.

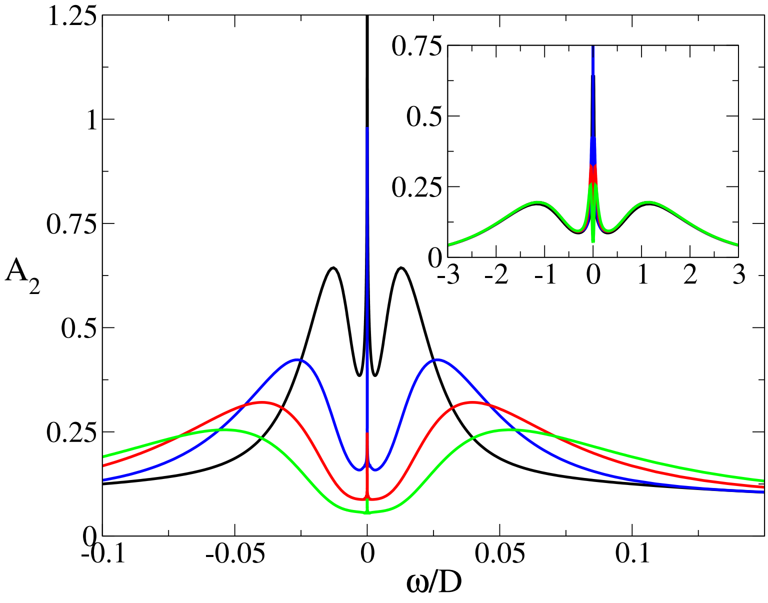

Figure 3.10: Spectral function $A_2(\omega)$ of the narrow band for $J/D = 0, 0.004, 0.008, 0.012$ (from top to bottom), $U/D = 2$, $\Gamma_1 = D/2\pi$, and $\Gamma_2/\Gamma_1 = 1/8$. Inset: the same spectral function on a wider scale.

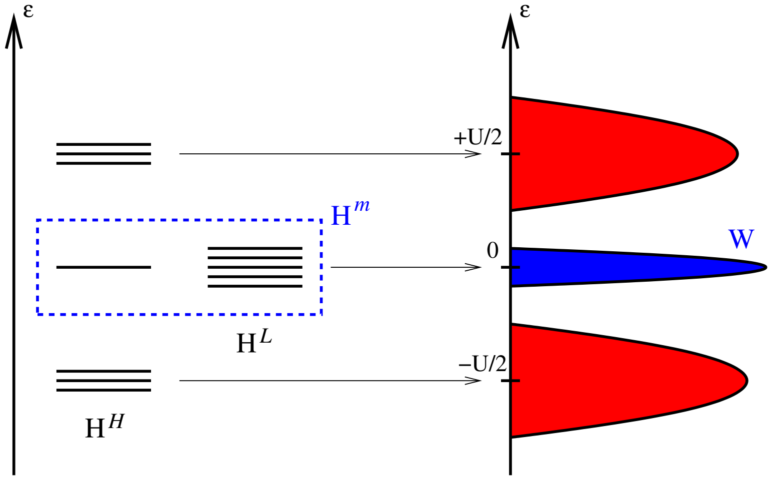

Figure 3.11: Schematic picture of the projective self-consistent technique. The Hubbard bands of the impurity density of states are found from the high-energy solutions of $\mathcal{H}^H$. The quasiparticle peak is constructed from the hybridization Hamiltonian $\mathcal{H}^m$ that couples the low-energy eigenvectors of $\mathcal{H}^L$ and $\mathcal{H}^H$.

resonance are equally compatible with the self-consistency condition. However, the event in which most of the spectral weight is concentrated in the two symmetric peaks, leaving only negligible weight within the narrow resonance, is extremely hard to identify with a limited number of levels. As an attempt to discriminate among the aforementioned possible scenarios, in the following section, we implement a projective self-consistency technique which allows a more detailed low-energy description within DMFT.

3.6 Projective Self-Consistent Technique

A remarkable feature uncovered by DMFT nearby a MIT is the clear separation of energy scales between well preformed high-energy Hubbard bands and lingering low-energy itinerant quasiparticles. It has been shown [90] that this partition of energy scales allows to reformulate the problem into a new one, in which the high-energy part is projected out. Essentially, the original Anderson impurity model, which involves both high-energy side-bands and low-energy quasiparticles, is reduced to a Kondo-like model which can be attacked more easily by a numerical procedure. In this section, we apply a projective technique to our model, which is similar to Ref. [90], with the only difference that the resulting effective problem is still an Anderson impurity model with rescaled parameters.

As we have shown, the occurrence of an OSMT does not seem to require a finite exchange, but rather a sufficiently small bandwidth ratio. Therefore, we prefer to present the projective technique in the simpler case where $J = 0$. Following Ref. [90], we start by rewriting the Anderson impurity model (3.13) explicitly separating low- (L) and high- (H) energy scales

$$\mathcal{H}_{\mathrm{AM}} = \mathcal{H}^H + \mathcal{H}^L + \mathcal{H}^m, \tag{3.15}$$

where

$$\mathcal{H}^H = \frac{U}{2}(n_f - 2)^2 + \sum_{k,a,\sigma}^{H} \epsilon^H_{ka} c^\dagger_{ka\sigma} c_{ka\sigma} + \sum_{k,a,\sigma}^{H} V^H_{ka}(f^\dagger_{a\sigma} c_{ka\sigma} + h.c.), \tag{3.16}$$

describes the impurity coupled to the high-energy levels,

$$\mathcal{H}^L = \sum_{k,a,\sigma}^{L} \epsilon^L_{ka} c^\dagger_{ka\sigma} c_{ka\sigma}, \tag{3.17}$$

is the low-energy bath Hamiltonian, and finally

$$\mathcal{H}^m = \sum_{k,a,\sigma}^{L} V^L_{ka}(f^\dagger_{a\sigma} c_{ka\sigma} + h.c.), \tag{3.18}$$

mixes low- and high-energy sectors (see Fig. 3.11). The impurity Green's function, also written as sum of a low- and a high-energy part, $G_a(i\omega) = G^L_a(i\omega) + G^H_a(i\omega)$, should satisfy the self-consistency requirement (3.14). If we assume that the low-energy spectral weight is $W_a \ll 1$, the self-consistency condition for the integrated low- and high-energy spectral functions, $\rho^L_a(\epsilon)$ and $\rho^H_a(\epsilon)$, respectively, implies the following sum-rules

$$\sum_{k}^{L} \left(V^L_{ka}\right)^2 = t_a^2 W_a, \tag{3.19}$$

$$\sum_{k}^{H} \left(V^H_{ka}\right)^2 = t_a^2 \left(1 - W_a\right), \tag{3.20}$$

showing that the impurity is strongly hybridized with the high-energy levels and very weakly with the low-energy ones. Let us for the moment neglect the coupling to the latter. The ground state of (3.16) is the adiabatic evolution of the states in which all negative-energy bath levels are doubly occupied and two electrons sit on the impurity, giving rise to a six-fold degenerate ground state. Other states with the same number of electrons lie above the ground state at least by an energy U. The lowest-energy states with one more (less) electron are more degenerate, since they emerge adiabatically from the states obtained by adding (removing) an electron either in the impurity levels or in the positive (negative)-energy baths. This large degeneracy is, however, split linearly by V^H_{ka}, which implies the broadening of the Hubbard bands around their centers of gravity $\pm U/2$. The main effect of the mixing term (3.18) is to provide a

Kondo exchange coupling between the six-fold degenerate ground state of $\mathcal{H}^H$ and the low-energy baths, which can be obtained by degenerate second-order perturbation theory in $\mathcal{H}^m$ or, more formally, by a Schrieffer-Wolff canonical transformation [90, 104]. Once the effective Kondo model is obtained, we could for instance follow Ref. [90], namely solve that model and impose the self-consistency condition to the impurity Green's function, calculated through the Schrieffer-Wolff canonically transformed $f_{a\sigma}$. To be consistent, one should in principle expand the transformed $f_{a\sigma}$ up to second order in V^L/U and impose the self-consistency requirement in the whole energy range, including low and high energies. In practice, even if the self-consistency is imposed only to the low-energy spectrum, one still gets a faithful description of the critical behavior near the MIT [90]. An equivalent procedure, that we have instead decided to follow, is to identify a new two-orbital Anderson impurity model, coupled only to the low-energy levels, which maps to the same Kondo model and next impose the self-consistency only to the low-energy part of the impurity Green's function:

$$t_a^2\, G_a^L(i\omega_n) = \sum_k \frac{\left(V_{ka}^L\right)^2}{i\omega_n - \epsilon_{ka}^L}. \tag{3.21}$$

Regarding the high-energy part of the self-consistency, since we always model the high-energy levels with just four levels at energies $\epsilon_{a\pm}^H = \pm U/2$, we need to impose an additional requirement besides (3.21), which, through (3.20), is simply

$$V_{a\pm}^H = t_a \sqrt{\frac{1-W_a}{2}}, \tag{3.22}$$

where W_a is the low-energy spectral weight obtained self-consistently from (3.21). The advantage of the projective method is that we can now model the low-energy spectrum with more levels, the cost being the additional self-consistency condition (3.22).

When we apply this projective technique to our two-orbital model with $J = 0$ and $t_1 \geq t_2$, we end up with an effective Anderson impurity model

$$\begin{aligned}\mathcal{H}_{\text{eff}} = {} & \frac{U_1}{2}(n_1-1)^2 + \frac{U_2}{2}(n_2-1)^2 + U_{12}(n_1-1)(n_2-1) \\ & + \sum_{k,a,\sigma}^{L} \epsilon_{ka}^L c_{ka\sigma}^\dagger c_{ka\sigma} + \sum_{k,a,\sigma}^{L} \sqrt{\gamma_a}\, V_{ka}^L (f_{a\sigma}^\dagger c_{ka\sigma} + h.c.).\end{aligned} \tag{3.23}$$

Here U_1 (U_2) is found from the solution of the high-energy problem (3.16) by looking at the energy difference of the states with one more or one less particle in orbital 1 (2) and we set $U_{12} = (U_1 + U_2)/2$ which assures the six-fold degeneracy of the isolated doubly-occupied impurity. In other words, if we denote by E_0 the energy of the six-fold degenerate ground-state and by $E_{\pm a}$ the energy of the ground-state in the sector with one more (less) particle on orbitals a, then $U_a = E_{+a} - 2E_0 + E_{-a}$ and we have that $U_1 \leq U_2$ with

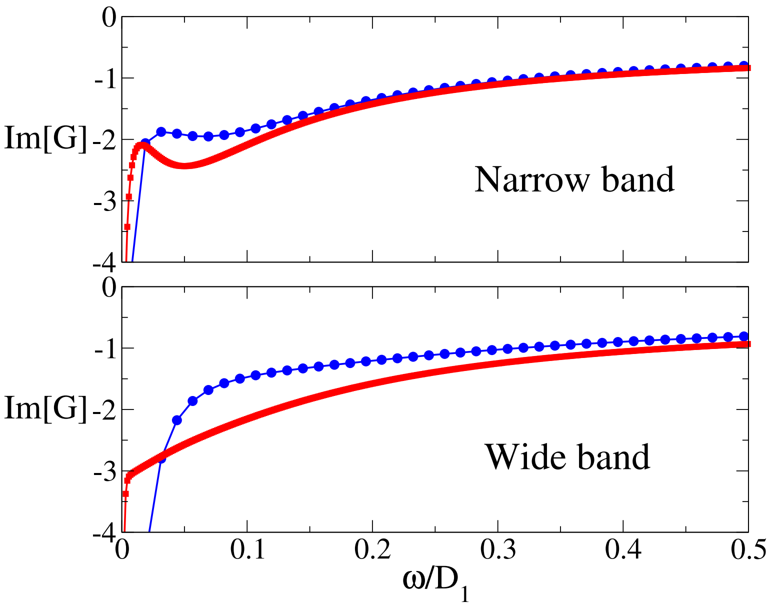

Figure 3.12: Imaginary part of the Green's function for $D_2/D_1 = 0.18$, $U/D_1 = 2.00$, and $J = 0$ as obtained by DMFT (circles) and with the PSCT (squares).

$U_2 - U_1 \sim t_1 - t_2$. Finally, $\sqrt{\gamma_a}$ gives the reduction of the overlap between states that are connected by $f^\dagger_{a\sigma}$, due to the introduction of the hybridization through V^H_{ka}: $\sqrt{\gamma_a} = \langle +a|f^\dagger_{a\sigma}|0\rangle$, where $|+a\rangle$ is the ground state with one more particle in orbitals a and $|0\rangle$ is the relevant[1] state in the ground-state multiplet. In this effective model, the high-energy levels provide a partial screening of the Hubbard repulsion, more efficient within orbital 1, which is more hybridized with the bath. Therefore, the difference of bandwidths acquires quite a transparent role in our projective method: while the *bare* Coulomb repulsion does not care about the orbitals in which electrons sit, this indifference is lost once the high-energy screening is taken into account. In Fig. 3.12, we compare the imaginary part of the Green's functions in Matsubara frequencies ω_n as function of ω_n as obtained by full DMFT or using the above projective self-consistent technique (PSCT), at $J = 0$. Note that within the PSCT, we model the low-energy conduction bath through five discrete levels. The agreement is satisfying, and the additional levels clearly allow for a more accurate description of the low-energy Green's function.

In Fig. 3.13, we plot the PSCT values of the quasiparticle residues Z_1 and Z_2 as function of U at $J = 0$ for $D_2/D_1 = 0.18$, as well as of the full spectral weights, W_1 and W_2, inside the Mott Hubbard gap. In agreement with standard

---

[1] This state is selected by fixing its quantum numbers.

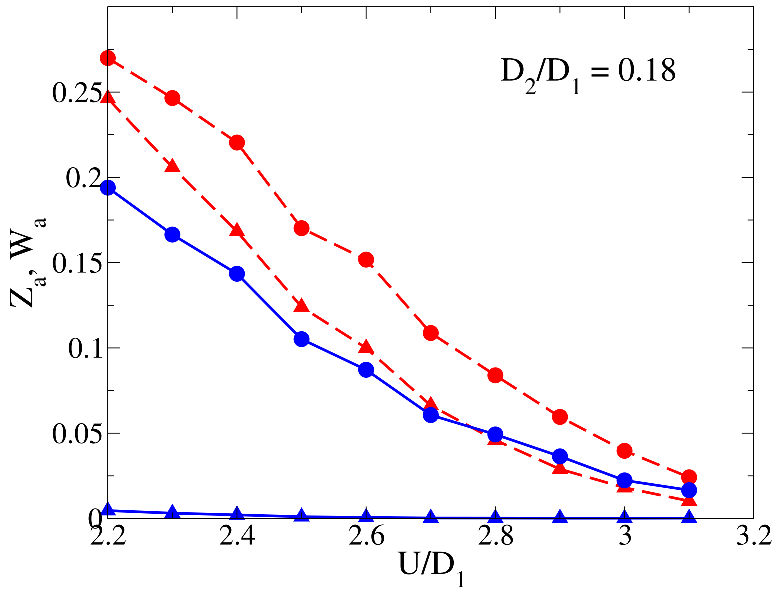

Figure 3.13: Quasiparticle residues Z_a (triangles) and low-energy spectral weights W_a (circles) as obtained by the PSCT with $J = 0$. Dashed lines refer to the wide band, and continuous lines to the narrow one.

DMFT, we find a region where Z_2 is zero within our numerical accuracy, while Z_1 is still finite. Yet, the total spectral weights are both non zero. In Fig. 3.14, we draw the DOS for the two bands and various U's. Note that the scale is different from the one in Fig. 3.7 and the position of the largest peaks found with the PSCT are in good agreement with the low-energy peaks obtained by DMFT. Moreover, even though the PSCT allows for two additional levels to model the low-energy part of the spectrum, after the self-consistency, no additional structure appears around the chemical potential. Actually, the two supplementary levels merge into the central or the lateral structures.

3.7 Discussion and Conclusions

In this chapter, we have studied by several techniques the properties of the Mott transition in an infinite-dimensional Hubbard model with two bands having the same center of gravity but different bandwidths, both in the presence and in the absence of the Hund's exchange splitting J. We have shown that a variational calculation based on a Gutzwiller wave function predicts that the two bands may undergo different metal-insulator transitions both for $J = 0$ and $J \neq 0$: By increasing U, the narrower band ceases to conduct before the wider one. The necessary condition for this orbital-selective Mott transition is

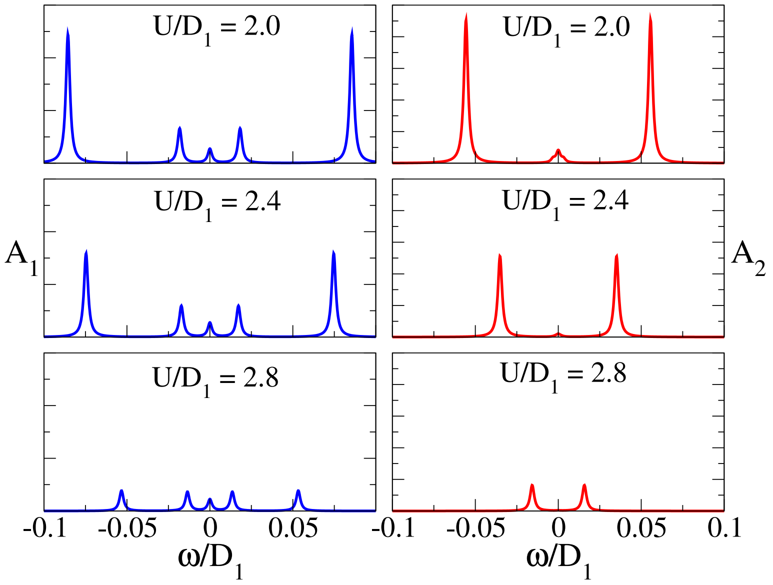

Figure 3.14: Low-energy part of the density of states of the wide band (left panels) and the narrow band (right panels) obtained within the PSCT for different U/D_1. The ratio of the bandwidth is $D_2/D_1 = 0.18$ and $J = 0$.

that the bandwidth ratio is lower than a critical value which increases with J, being 0.2 when $J = 0$, see Fig. 3.3. The behavior of the quasiparticle residues as obtained by DMFT using exact diagonalization as impurity solver confirms, even quantitatively, the variational results, showing that the residue of the narrower band may vanish before the one of the wider band if the bandwidth ratio is sufficiently small. In this model the OSMT occurs both in the absence and in the presence of an exchange splitting. We notice that, in more general situations where the number of orbitals is greater than two and different from the number of electrons, as for instance in the case of t_{2g} orbitals occupied by two or four electrons on average, the Coulomb exchange would instead compete against the angular momentum quenching which occurs in the OSMT scenario. Therefore we suspect that the role of the Coulomb exchange might actually depend on the specific model.

However, a closer inspection of the low-energy spectral properties of the narrower band in the region, where it is apparently insulating while the wider band still conducts, poses doubts on the above simple scenario. The reason is that, in spite of a quasiparticle residue which is zero within our numerical accuracy, the narrower band has spectral weight inside the Mott-Hubbard gap, which scales like the quasiparticle residue of the wider band. In other words, the charge fluctuations which still occur in the wider band are transferred into the narrower one, as one can expect. This low-energy spectral weight is concentrated in two peaks symmetrically located around the chemical potential. Roughly speaking, the distance of each peak from the chemical potential is $2J$ plus a quantity of the order of the quasiparticle resonance width of the wider band. Due to our limited numerical resolution, we can not establish rigorously whether these two peaks (a) signal a narrow-gap semiconducting behavior, (b) signal a semimetallic behavior, with a power-law vanishing density of states, (c) or coexist with an extremely narrow resonance at the chemical potential, with a spectral weight well below our numerical accuracy, just like the single impurity does. Although the elements at our disposal do not definitely allow to discriminate among these three scenarios, one can recognize that some of them are more plausible than the others.

The first possibility (a) of a narrow-gap semiconductor seems very unlikely. Indeed, in this case, the gap between the two low-energy peaks would open large and then diminish as the quasiparticle resonance width of the wider band, by further increasing the repulsion U. Therefore, the insulating character of the narrower band would weaken by increasing U, which seems a bit unlikely.

Let us consider instead the scenario (b) of a semimetal. If taken literally, it would imply a vanishingly small local magnetic susceptibility, while we actually find a very large one, much larger than the local susceptibility of the wider band. However, a semimetallic behavior would imply, in our particle-hole symmetric case, a breakdown of Fermi-liquid theory[2]. Therefore, a power-law vanishing single-particle DOS might not necessarily conflict with almost free-spin excitations in a scenario in which Fermi-liquid theory breaks down and for instance spin-charge separation emerges. Although it might represent a quite interesting circumstance, yet we could not find any physical arguments justifying such a non-Fermi liquid behavior. Therefore, we are tempted to discard it in favor of the more conservative scenario (c) in which the two peaks coexist with a narrow resonance which remains tied at the chemical potential, its spectral weight being smaller than our numerical accuracy. This resonance should disappear right at the same U where the wider band ceases to conduct. Finally, we note that, whatever the correct zero-temperature scenario, either (b) or (c), there should exist a finite-temperature interval where the narrower band loses its coherence unlike the wider one, which might display unusual properties.

We terminate by mentioning that a parallel work by de' Medici *et al.* [84] studied the same problem using DMFT and a slave-spin mean-field approach and reached similar conclusions. Moreover, in Ref. [18], the zero-temperature properties of the self-energy of the wide band were investigated in detail and

---

[2] In the presence of particle-hole symmetry, the chemical potential is strictly zero whatever is the interaction. On the other hand, if Fermi-liquid theory holds, then $\mathrm{Im}\,\Sigma(\omega) \sim \omega^2$. In this case, it turns out that the value of the DOS at the chemical potential should not be affected by U and J. Therefore, if one finds a different DOS from the *bare* one, that necessarily implies a breakdown of Fermi-liquid theory.

point in favor of scenario (b). Indeed, in their calculation, the low-energy behavior of the self-energy displays non-Fermi liquid behavior. Finally, the problem of the OSMT has continued to attract a lot of interest after the completion of this work and an overview of the related activity can be found in Ref. [65].

Chapter 4

Critical Behavior in Impurity Trimers and Tetramers

We study two clusters of three and four Kondo impurities by means of Wilson's numerical renormalization group and conformal field theory. In both clusters, the spin-1/2 magnetic moments are connected between them through a direct exchange and each one is coupled to a conduction bath. The competition between the Kondo effect, that is favored by a degenerate ground-state, and the direct exchange, that tends to split this degeneracy, leads to rich phase diagrams displaying stable phases separated by quantum critical lines. We precisely analyze these different phases by identifying the correct theory for every fixed point of the renormalization group. We finally discuss their properties in connection with the Mott transition as described by cluster dynamical mean-field theory. Indeed, an impurity trimer and tetramer represent the simplest clusters to simulate a Hubbard model on a triangular and square lattice. In this context, we show that exotic behaviors that are found close to the Mott transition in lattice models might well be traced back to instabilities, like antiferromagnetism or Cooper pairing, that are already present at the impurity level. The project presented in this chapter has been realized in collaboration with M. Fabrizio, L. De Leo and P. Lecheminant.

4.1 Introduction

More than fifty years after its proposal [91], the Mott transition remains an issue of current and broad interest, continually revived by the discovery of strongly correlated materials which display anomalous phenomena in the vicinity of a Mott insulating phase. The interaction-driven metal-to-insulator transition emerges out of the competition between the tendency of the electrons to delocalize throughout the crystal, so as to maximize the band-energy gain, and the Coulomb repulsion among the same electrons which, on the contrary, tends to suppress valence fluctuations by localizing the carriers. Yet, as we have discussed in Chapter 1, realistic systems generally involve other energy scales besides the Coulomb repulsion and the band-energy gain. Let us collectively denote them by J. Approaching the Mott insulating phase, the entropy is first reduced by the onset of a quasiparticle Fermi sea below a temperature T_F^*, which gradually decreases because of strong correlations. At some point, T_F^* will become of the same order as J and the new energy scales compete with the formation of a degenerate quasiparticle gas. Indeed, the presence of J provides new mechanisms to quench the entropy by freezing spin and orbital degrees of freedom, independently from the charge degrees of freedom. This situation is actually realized in heavy fermion materials, where the Kondo effect, favoring the formation of a coherent band of heavy quasiparticles, competes with the RKKY interaction. Here, this competition is supposedly the key to understand the anomalies which appear at the transition between the heavy fermion paramagnet and the magnetically ordered phase [32, 106].

Competing Screening Mechanisms in Anderson Impurity Models

The heavy-fermion example is particularly pertinent for introducing the subject of this chapter. Indeed, the competition between Kondo effect and RKKY coupling has interesting consequences not only in the periodic Anderson model but already at the level of Anderson impurity models. For instance, the phase diagram of two spin-1/2 impurities coupled to a conduction bath but also by a direct antiferromagnetic exchange has two limiting regimes: one where each impurity is independently Kondo screened by the conduction electrons and another where the direct exchange takes care of locking the impurity spins into a singlet state, which is transparent to the conduction electrons. Under particular circumstances, these two regimes are separated by a quantum critical point, at which non-Fermi-liquid behavior emerges [5, 7, 60, 61, 62]. The phase diagram grows richer when one considers three antiferromagnetically coupled spin-1/2 impurities [55, 97]. In this case, besides a Kondo screened regime, there are other phases where the direct exchange prevails even if it is unable to fully quench the impurity degrees of freedom. This leads to stable non-Fermi-liquid phases analogous to overscreened multi-channel Kondo models [2, 3]. These clusters of impurity models are not only interesting as simple attempts towards understanding the fully periodic Anderson model. For instance, compact clusters of impurities are achievable experimentally by adsorbing atoms on metallic surfaces. Indeed, trimers of Cr atoms have already been realized on gold surfaces [58], which has actually motivated the most recent theoretical activity on impurity trimers [55, 72, 75, 102]. In this context, the major task is to identify those phases that are stable towards perturbations which are generally allowed on metallic surfaces. Therefore, the quantum critical points which separate stable phases are of minor interest, as they are extremely unlikely to occur.

Impurity Models and Dynamical Mean-Field Theory

The unstable critical points arise when the competition between Kondo screening and RKKY coupling is maximum. This is nothing but the impurity counterpart of the situation when $T_F^* \simeq J$ that we previously met in connection with the Mott transition. This weak analogy turns into an actual equivalence within the dynamical mean-field theory (DMFT) [42], which is the quantum analogue of classical mean-field theory and, like the latter, becomes exact for infinite coordination lattices (see Section 2.3). Within this limit, the single-particle self-energy becomes fully local but maintains a non-trivial time-dependence. In order to determine the frequency-dependent self-energy, within DMFT, one solves an auxiliary single-impurity Anderson model, designed to have an impurity self-energy that coincides with the local self-energy of the lattice model. This requirement translates into an impurity model which is identified by the same local interaction as the lattice model and by a coupling to a conduction bath which has to be self-consistently determined. As an approximation, which is not exact in any limiting case, DMFT can be extended to include short-range spatial components of the self-energy [69, 77, 81, 98, 105]. In these novel versions, the lattice model is mapped onto a cluster of Anderson impurities, subject to a self-consistency condition which is however no longer uniquely determined by the requirement that the approximation becomes exact in particular limits.

In the original single-site formulation of DMFT, the physics of the Anderson impurity turned out to be a precious guideline to interpret the DMFT results. This was possible mainly because a lot was already known about single-impurity models. On the contrary, apart from few exceptions [60, 97], little is known about impurity clusters. This is likely the reason why, in the cluster versions of DMFT, not much attention has been paid so far to the impurity-cluster models *per se*. In addition, since impurity clusters involve many energy scales, including inter-impurity processes, it is not *a priori* evident whether there is a common interpreting scheme like the Kondo physics in the single-impurity case.

In order to clarify this issue, let us start by recalling some basic facts about the single-site DMFT mapping onto impurity models. Within this mapping, the quasiparticle effective Fermi temperature T_F^* translates into the Kondo temperature T_K of the impurity model. The self-consistency condition causes T_K to vanish at a finite value of U, which signals, in the lattice counterpart, the onset of the Mott transition. This also implies that the metallic phase just prior to the Mott transition translates into an Anderson impurity model deep inside the Kondo regime, with a very narrow Kondo resonance and well formed Hubbard side-bands [42]. The same behavior should remain even when dealing with a cluster of impurities, which should translate into a cluster of Kondo impurities that can effectively be regarded as a single impurity with many internal degrees of freedom. The novelty stems from the other energy

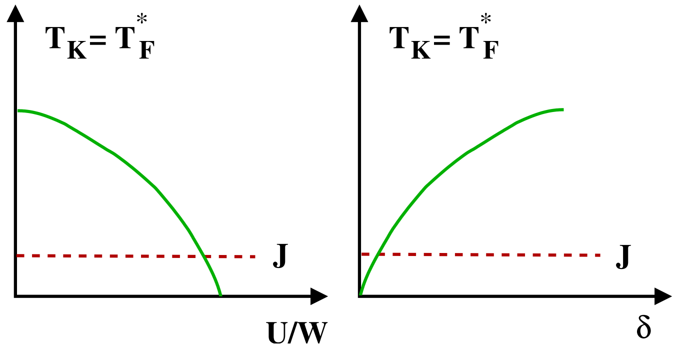

Figure 4.1: Behavior versus U and the doping of the quasiparticle Fermi temperature T_F^*, which translates within DMFT into the Kondo temperature T_K of the effective impurity model.

scales, which we denoted as J, that take care of quenching, in the Mott insulator, the degrees of freedom other than the charge. Indeed, near the Mott transition, J translates into additional processes, like for instance an inter-impurity exchange, which tends to remove, completely or partially, the degeneracy of the cluster. Consequently, J competes with the Kondo effect, which takes better advantage the more degenerate the impurity cluster.

We note that this competition is always active in impurity clusters while it is commonly absent in single-impurity models except in particular multi-orbital cases [25, 26]. We believe that it is this additional ingredient, the common denominator of all impurity-cluster models, which endows them with the capability to provide a more faithful description of a realistic Mott transition within DMFT.

Indeed, in the presence of J, the approach to the Mott transition displays, as qualitatively shown in Fig. 4.1, a Kondo temperature smoothly decreasing from its initial value W as U/W increases. Just before the transition, T_K becomes of order J. Analogously, (see Fig. 4.1) if one starts from the Mott insulator and dopes it, T_K will smoothly increase from its value $T_K = 0$ at zero doping, until it crosses a value of order J. This is the location of the, possibly quantum critical, point which separates the Kondo screened phase, $T_K \gg J$, from the regime in which the internal screening mechanism prevails, $J \gg T_K$. Therefore, these critical points are always crossed in impurity models onto which lattice models approaching a Mott transition are mapped within cluster DMFT. The question is whether and how they may influence the behavior of the lattice model after the DMFT self-consistency is carried out.

It has been argued [34, 36] that these impurity critical points do play an important role in determining the phase diagram of the corresponding lattice models. Indeed, near these unstable critical points, the impurity models display strongly enhanced local susceptibilities (or, equivalently, enhanced local

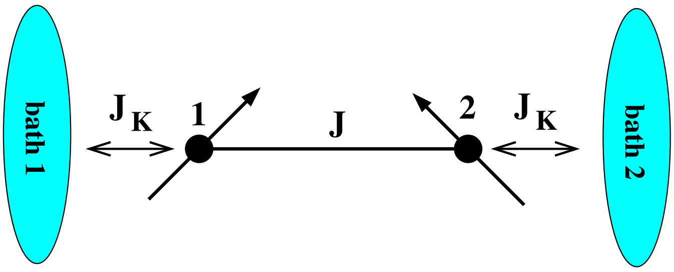

Figure 4.2: The impurity dimer with the Hamiltonian (4.1).

irreducible four-leg vertices) in several instability channels. Moreover, within DMFT the irreducible four-leg vertices, which enter the Bethe-Salpeter equations, coincide with the local ones [42]. Therefore, it is reasonable to argue that, after the full DMFT self-consistency is carried out, these local instabilities may turn into full bulk instabilities, leading to symmetry broken phases that partially hide what would have been the quantum critical regions around the impurity unstable fixed points. This hypothesis, which has been tested with success by a full DMFT calculation in a two-orbital Hubbard model [26], suggests that the analysis of impurity-cluster models, even without any DMFT self-consistency, may be very helpful in interpreting and even anticipating the phase diagrams of strongly-correlated lattice models as uncovered by cluster DMFT.

Following this speculation, we will, in this chapter, study the phase diagram of the simplest Anderson impurity clusters, namely a trimer and a tetramer of impurities, which can be used to implement a cluster DMFT calculation for the Hubbard model on a square lattice. Needless to say, the interest in impurity clusters goes beyond its possible relevance to Hubbard models on a square lattice. As we previously mentioned, these clusters may be experimentally realized on metallic surfaces or, eventually, by arranging quantum dots in proper geometries. Moreover, as will emerge from our analysis, these models represent a theoretical challenge by themselves which requires the full machinery of Wilson's numerical renormalization group (NRG) and conformal field theory (CFT) in order to have a detailed understanding (see Sections 2.6 and 2.7).

4.2 The Impurity Dimer

Before starting a systematic study of three and four impurity clusters, let us briefly review the simplest example of an impurity dimer. This model was originally studied by Jones and Varma [60, 61, 62] using NRG and the results were later interpreted by Affleck and Ludwig [5, 7] within CFT. For simplicity, we consider the impurity dimer drawn in Fig. 4.2 with the following Hamiltonian

$$\begin{aligned}\mathcal{H} = \sum_{a=1}^{2}\Big[\sum_{\mathbf{k}\sigma} \epsilon_{\mathbf{k}}\, c^\dagger_{a\,\mathbf{k}\sigma} c_{a\,\mathbf{k}\sigma} + \frac{J_K}{2V}\sum_{\mathbf{k}\mathbf{k}'\alpha\beta} \mathbf{S}_a \cdot c^\dagger_{a\,\mathbf{k}\alpha}\, \boldsymbol{\sigma}_{\alpha\beta}\, c_{a\,\mathbf{k}'\beta}\Big] \\ + J\,\mathbf{S}_1\cdot\mathbf{S}_2 \equiv \sum_{a=1}^{2}\mathcal{H}^K_a + J\,\mathbf{S}_1\cdot\mathbf{S}_2,\end{aligned} \tag{4.1}$$

which describes two spin-1/2 impurities, coupled together by an antiferromagnetic J, and both Kondo coupled to their own conduction bath by an antiferromagnetic J_K. The operators $c^\dagger_{a\,\mathbf{k}\sigma}$ and $c_{a\,\mathbf{k}\sigma}$ create and annihilate, respectively, a conduction electron with spin σ and momentum $\mathbf{k}$ in the bath a, and $\boldsymbol{\sigma}$ are the Pauli matrices. The two conduction baths are assumed to be degenerate and particle-hole invariant. Furthermore, we assume that the conduction-bath density of state is finite and smooth around the chemical potential on a scale larger than the Kondo temperature. As a consequence, the two baths, in the absence of the impurities, can be described [1] by a CFT which includes independent spin $SU(2)_1$ and charge isospin $SU(2)_1$ symmetry for each bath, namely an overall

$$\big(SU(2)^{(1)}_1 \times SU(2)^{(2)}_1\big)_{\text{charge}} \times \big(SU(2)^{(1)}_1 \times SU(2)^{(2)}_1\big)_{\text{spin}}.$$

The subscript in $SU(2)^{(a)}_k$ can be regarded here as the number of copies of spin-1/2 electrons participating to the $SU(2)$ algebra, while the superscript refers to the bath.

The hypothesis behind the use of CFT is that, once the coupling to the impurities is switched on, conformal invariance is not lost. The effect of the impurities is then merely to change the conduction-bath boundary conditions (BCs) among the conformally invariant ones. An important step in determining the allowed BCs is the *conformal embedding* [35], which amounts to identifying the conformal field theories corresponding to the symmetry groups under which the Hamiltonian of the bath plus the impurity remains invariant. In the most favorable cases, the BCs that actually emerge correspond to conformally invariant BCs only within one of the different CFTs of the embedding. The next useful information is that the conformally invariant BCs within each sectors can be obtained by the so-called *fusion hypothesis*, according to which, starting from the spectrum of a known BC, one can obtain all the others upon *fusion* with the proper primary fields of the CFT (see Section 2.7).

In the model of Fig. 4.2, the isospin generators commute with the Hamiltonian even when J_K and J are finite, and the charge sector can still be represented by two independent isospin $SU(2)_1$. On the other hand, only the overall spin $SU(2)$ transformations leave the Hamiltonian invariant, which translates into an $SU(2)_2$ (two copies of electrons) CFT. As a result, the proper embedding in the spin sector is [5]

$$SU(2)_1 \times SU(2)_1 \to SU(2)_2 \times Z_2,$$

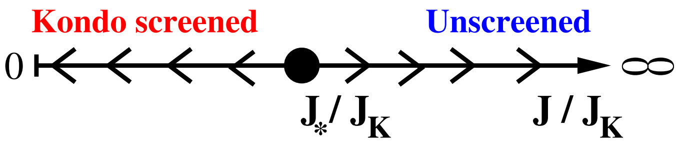

Figure 4.3: Renormalization group flow diagram of the impurity dimer.

where Z_2 denotes an Ising CFT reflecting the symmetry under permutation of the two baths.

The NRG phase diagram of the model [60, 61, 62] is sketched in Fig. 4.3 and includes, as we previously mentioned, two stable phases: a Kondo screened and an unscreened phase, separated by an unstable critical point when $J = J_* \simeq T_K$. Affleck and Ludwig [5, 7] realized that these different fixed points are described by the three different BCs of the Ising CFT. The two stable phases correspond to fixed BCs, where one Ising spin orientation is prohibited at the boundary, and the unstable fixed point to a free BC, where both orientations are allowed. Starting from the unscreened phase, the Kondo screened phase is obtained by fusion with the Ising primary field ϵ of dimension $1/2$, while the unstable fixed point is obtained by fusion with the primary field σ of dimension $1/16$.

As shown in Section 2.7, CFT also allows, by double-fusion, to determine the scaling dimensions of the relevant operators. It turns out that there are three equally relevant (i.e. with dimension smaller than one) symmetry-breaking perturbations which can destabilize the unstable fixed point. They all have the same dimension $1/2$ as the invariant operator which moves away from the fixed point and corresponds to a deviation of J from its fixed point value J_* at fixed T_K. The first perturbation is an opposite spin magnetization for the two baths. The second is a BCS term in the inter-bath Cooper singlet channel. The last perturbation corresponds to a direct hybridization between the two baths breaking the independent conservation of charge.

The latter is very important. Indeed, let us suppose that, instead of two spin-$1/2$ impurities, we have two single-orbital Anderson impurities with the Hamiltonian

$$\begin{aligned}\mathcal{H} = \sum_{a=1}^{2} \Big[\sum_{\mathbf{k}\sigma} \epsilon_{\mathbf{k}}\, c^{\dagger}_{a\,\mathbf{k}\sigma} c_{a\,\mathbf{k}\sigma} - \frac{t_K}{\sqrt{V}} \sum_{\mathbf{k}\sigma} c^{\dagger}_{a\,\mathbf{k}\sigma} d_{a\,\sigma} + H.c. \Big] \\ - t_{\perp} \sum_{\sigma} d^{\dagger}_{1\,\sigma} d_{2\,\sigma} + H.c. + \frac{U}{2} \sum_{a=1}^{2} (n_a - 1)^2,\end{aligned} \tag{4.2}$$

where $d_{a\,\sigma}$ are the annihilation operators for the impurity and $n_a = \sum_\sigma d^{\dagger}_{a\,\sigma} d_{a\,\sigma}$. It is actually the model (4.2) rather than (4.1) that has to be used to simulate, with a single dimer, a Hubbard model within cluster DMFT. As we previously mentioned, the approach to the Mott transition corresponds to an impurity model deep inside the Kondo regime, namely with $U \gg t_K, t_\perp$. Within this limit, the model (4.2) can be mapped by a Schrieffer-Wolff transformation onto (4.1), with $J = 4t_\perp^2/U$ and $J_K = 4t_K^2/U$. However, at next order in $1/U$, a local direct hybridization V among the baths is generated, with $V \sim J_K\, t_\perp/U$. Although small, V is a relevant perturbation which makes the unstable fixed point of the model (4.1) inaccessible in the model (4.2). Yet, since $J \gg V$, a quantum critical region, instead of a true quantum critical point, is still well visible as was shown in Ref. [34]. In other words, the quantum phase transition which occurs in model (4.1) turns into a very sharp crossover in (4.2). This suggests that the unstable fixed point of the spin-dimer may still influence the approach to the Mott transition in lattice models which map within DMFT onto the impurity model (4.2). In particular, if the latter is used to mimic, within cluster DMFT, a Hubbard model on a square lattice, we would speculate that near the Mott transition the inter-site singlet Cooper pairing and the tendency to antiferromagnetic ordering are strongly enhanced, since both are instability channels of the dimer fixed point (note that the hybridization among the baths is explicitly present in the Hamiltonian). Most likely, antiferromagnetism prevails at half-filling, but upon doping, superconductivity might still emerge [34].

4.3 The Impurity Trimer

Let us move now to our actual work and start considering the impurity trimer drawn in Fig. 4.4 with the Hamiltonian

$$\mathcal{H} = \sum_{a=1}^{3} \mathcal{H}_a^K + J\,(\mathbf{S}_1 + \mathbf{S}_3)\cdot\mathbf{S}_2 + J'\,\mathbf{S}_1\cdot\mathbf{S}_3, \qquad (4.3)$$

where $\mathcal{H}_a^K$ has been defined in (4.1). This model describes three spin-1/2 impurities coupled together by antiferromagnetic J and J' and to their own conduction bath by $J_K > 0$. As before, we assume that the baths are degenerate and particle-hole invariant. When $J' = 0$ the trimer is the next simple cluster beyond the dimer to represent a Hubbard model on a square lattice within cluster DMFT. This would really be true only if we considered three single-orbital Anderson impurities coupled by a single-particle hopping $t_\perp$ rather than three spin-1/2 moments coupled by an exchange J. However, in view of what we discussed in the case of the dimer, the model (4.3) is more suitable to identify unstable fixed points which might transform into sharp crossover regions in the case of Anderson impurities because of the weak hybridization among the baths generated by $t_\perp$. For this reason, we will consider, both here for the trimer and later for the tetramer, spin-1/2 Kondo impurities and treat the hybridization among the baths as a perturbation.

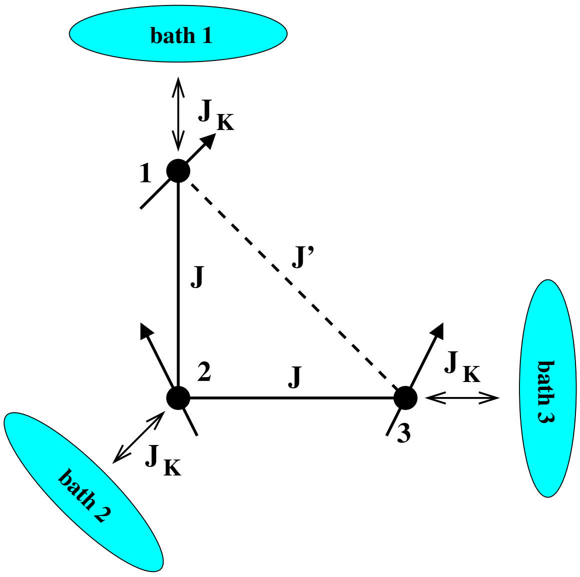

Figure 4.4: The impurity trimer with the Hamiltonian (4.3).

4.3.1 CFT Preliminaries for the Trimer

As in the dimer example, the trimer model (4.3) exhibits charge degrees of freedom described by three independent isospin $SU(2)_1^{(a)}$ CFTs, $a = 1, 2, 3$. The expression of the inter-impurity exchange naturally suggests how the spin symmetry should be reduced. First, we have to couple the spin sectors of baths 1 and 3 into an overall $SU(2)_2$ via the embedding

$$SU(2)_1^{(1)} \times SU(2)_1^{(3)} \rightarrow SU(2)_2^{(1-3)} \times Z_2,$$

where Z_2 denotes the Ising CFT. Then, the $SU(2)_2$ is coupled to the bath 2 into an overall $SU(2)_3$ according to embedding

$$SU(2)_2^{(1-3)} \times SU(2)_1^{(2)} \rightarrow SU(2)_3 \times (\mathrm{TIM})\,,$$

where TIM stands for the tricritical Ising model CFT. Combining everything together, we see that the original symmetry of the three independent spin $SU(2)_1^{(a)}$ is reduced to

$$SU(2)_3 \times Z_2 \times (\mathrm{TIM})\,.$$

This conformal embedding can be rigorously justified by the *character decomposition* [35], namely by the formal identification of the free energies in the original and in the decomposed theory (see Appendix A).

$\times$	$\mathbf{I}$	$\boldsymbol{\epsilon}$	$\mathbf{t}$	$\boldsymbol{\epsilon}^{''}$	$\boldsymbol{\sigma}$	$\boldsymbol{\sigma}^{'}$
$\mathbf{I}$	I	ϵ	t	$\epsilon^{''}$	σ	$\sigma^{'}$
$\boldsymbol{\epsilon}$	ϵ	$I+t$	$\epsilon+\epsilon^{''}$	t	$\sigma+\sigma^{'}$	σ
$\mathbf{t}$	t	$\epsilon+\epsilon^{''}$	$I+t$	ϵ	$\sigma+\sigma^{'}$	σ
$\boldsymbol{\epsilon}^{''}$	$\epsilon^{''}$	t	ϵ	I	σ	$\sigma^{'}$
$\boldsymbol{\sigma}$	σ	$\sigma+\sigma^{'}$	$\sigma+\sigma^{'}$	σ	$I+\epsilon+t+\epsilon^{''}$	$\epsilon+t$
$\boldsymbol{\sigma}^{'}$	$\sigma^{'}$	σ	σ	$\sigma^{'}$	$\epsilon+t$	$I+\epsilon^{''}$

Table 4.1: Fusion rules of the tricritical Ising model.

The $SU(2)_k$ CFT has central charge $c = 3k/(2+k)$. Its primary fields $\phi_{2j}^{(k)}$ are labeled by a spin quantum number $j = 0, \ldots, k/2$ and have the following scaling dimensions and fusion rules:

$$\Delta_j^{(k)} = j(j+1)/(2+k)$$
$$j \times j' = |j-j'| + (|j-j'|+1) + \cdots + \min(j+j', k-j-j').$$

The Ising CFT, with central charge $c = 1/2$, has three primary fields, the identity I, the thermal energy ϵ_I and the order parameter σ_I [35]. Their dimension and fusion rules [35, p. 221] are given by

$$\Delta_I = 0, \qquad \Delta_{\epsilon_I} = 1/2, \qquad \Delta_{\sigma_I} = 1/16$$
$$\sigma_I \times \sigma_I = I + \epsilon_I, \qquad \sigma_I \times \epsilon_I = \sigma_I, \qquad \epsilon_I \times \epsilon_I = I.$$

Finally, the TIM has central charge $c = 7/10$ and six primary fields [35]: the identity I, ϵ, t, $\epsilon^{''}$, σ and $\sigma^{'}$. Their dimension are

$$\Delta_I = 0, \qquad \Delta_\epsilon = 1/10, \qquad \Delta_t = 3/5,$$
$$\Delta_{\epsilon''} = 3/2, \qquad \Delta_\sigma = 3/80, \qquad \Delta_{\sigma'} = 7/16,$$

and the fusion rules [35, p. 224] between these fields are shown in Table 4.1.

As we previously mentioned, the possible conformally invariant boundary conditions can be classified by means of the fusion hypothesis [2, 3, 7]. Starting from the spectrum of a simple BC, for instance corresponding to $J_K = 0$, one can obtain the spectra of other allowed BCs upon fusion with the primary fields of the CFTs. By comparing the low-energy spectra determined in this way with those obtained by NRG, one can identify and characterize all fixed points of the model.

4.3.2 Fixed Points in the Trimer Phase Diagram

In Fig. 4.5, we sketch the phase diagram of the impurity trimer as obtained by NRG (see Section 2.6). The calculations were performed with $\Lambda = 3$.

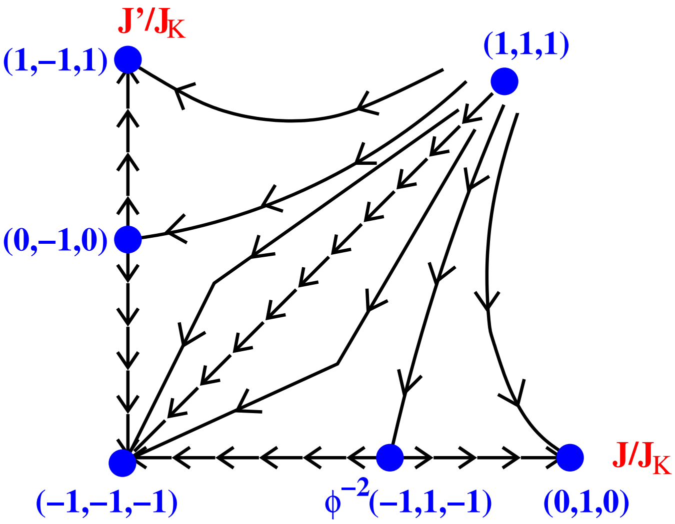

Figure 4.5: Renormalization group flow diagram for the trimer model.

We use both spin and isospin symmetries that allow to keep up to 2000 states at each iteration. Each phase is then identified by a fixed point of the renormalization group, which can be either stable or unstable, as indicated by the flow lines drawn in the figure. In order to have a classification scheme which works equally well for Fermi-liquid and non-Fermi-liquid phases, the fixed points are identified through the zero-frequency values of the bath S-matrices (S_1, S_2, S_3), which can be obtained by CFT through the modular $\mathcal{S}$-matrix (see Section 2.7.3 and Appendix B). Let us now discuss all fixed points, starting from the trivial one with $(S_1, S_2, S_3) = (1, 1, 1)$ corresponding to the case $J_K = 0$.

The Fixed Point $(1, 1, 1)$

The fixed point with $J_K = 0$ describes impurities that are completely decoupled from the conduction baths. In this case, the conduction bath electrons do not experience any phase shift and correspondingly $(S_1, S_2, S_3) = (1, 1, 1)$. This fixed point is unstable towards switching on J_K, since the impurity trimer is always in a non-zero spin configuration and the Kondo exchange is a marginally relevant perturbation (see Fig. 4.5). We will take this fixed point as the ancestor BC which, upon fusion with primary fields, will provide all other BCs.

The Fixed Point $(-1, -1, -1)$

This fixed point describes a conventional perfectly Kondo-screened phase, that can be obtained [2, 3] from the $(1, 1, 1)$ fixed point upon fusion with the highest weight representation of the $SU(2)_3$ CFT with $j = 3/2$. It is clear that this phase extends in a whole region around the origin $J = J' = 0$ in Fig. 4.5. Indeed, when $J = J' = 0$, each impurity is independently Kondo screened by its own conduction bath and this perfect screening can not be affected by finite J and J' much smaller than the Kondo temperature. It is far less obvious that this fixed point remains stable for large $J \simeq J'$. When $J' = J \gg T_K$, the impurity locks into two degenerate S=1/2 configurations. In the first, sites 1 and 3 are coupled into a triplet which in turn is coupled with site 2 into an overall spin-1/2 configuration. Since this is even by interchanging 1 with 3, we denote it as $|e\rangle$. The other configuration, which we denote as $|o\rangle$, is odd under $1 \leftrightarrow 3$ and corresponds to coupling sites 1 and 3 into a singlet, leaving behind the free spin-1/2 moment of site 2. The Kondo exchange projected onto this subspace reads

$$\begin{aligned}&\frac{J_K}{3}\,|e\rangle\langle e|\,\mathbf{S}\cdot\big(2\mathbf{J}_1(0)-\mathbf{J}_2(0)+2\mathbf{J}_3(0)\big)+J_K\,|o\rangle\langle o|\,\mathbf{S}\cdot\mathbf{J}_2(0)\\&-\frac{J_K}{\sqrt{3}}\Big(|e\rangle\langle o|+|o\rangle\langle e|\Big)\,\mathbf{S}\cdot\big(\mathbf{J}_1(0)-\mathbf{J}_3(0)\big),\end{aligned} \tag{4.4}$$

where $\mathbf{S}$ describes the effective S=1/2 of the trimer, while $\mathbf{J}_a(0)$ is the spin density of bath $a = 1, 2, 3$ at the impurity site, assumed to be the origin. All the above screening channels flows to strong coupling within a one-loop calculation. Since it is readily shown that the impurity can be perfectly screened, both in the spin and in the e-o channels, one has to conclude that the whole line $J = J'$ at finite J_K corresponds to the Kondo screened fixed point $(-1, -1, -1)$, as shown in Fig. 4.5. A small deviation from $J = J'$ splits the degeneracy between $|e\rangle$ and $|o\rangle$ and would eventually destabilize this fixed point, the faster the smaller J_K.

The Fixed Point $(0, 1, 0)$

This fixed point occurs for $J \gg T_K, J'$ (see Fig. 4.5). The NRG spectrum is shown at the far right of Fig. 4.6 and the energies are reported in Table 4.2. This spectrum is compatible with that obtained by first fusing the $(1, 1, 1)$ fixed point with the $j = 3/2$ primary field of the $SU(2)_3$ CFT and then with the field σ' of the TIM. It is not difficult to realize that this fixed point is equivalent to the non-Fermi-liquid phase of the S=1/2 two-channel Kondo model [2, 3]. Indeed, if $J' = 0$ and J is very large, the trimer is locked into the S=1/2 configuration which we previously denoted as $|e\rangle$, to indicate the even parity upon $1 \leftrightarrow 3$. According to (4.4), the Kondo exchange projected onto this configuration is

$$\mathbf{S}\cdot\sum_{a=1}^{3} J_K^{(a)}\,\mathbf{J}_a(0) = \frac{J_K}{3}\,\mathbf{S}\cdot\big(2\mathbf{J}_1(0)-\mathbf{J}_2(0)+2\mathbf{J}_3(0)\big). \tag{4.5}$$

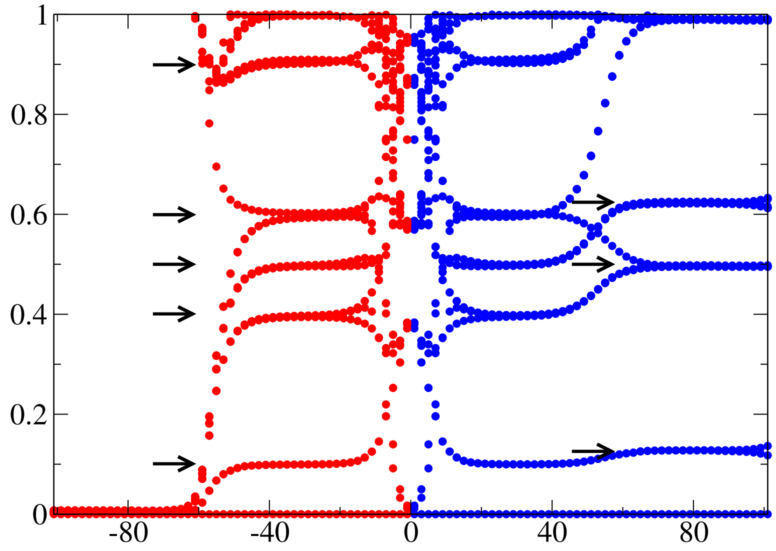

Figure 4.6: Flow diagrams for $J' = 0$ and J slightly smaller (left) and slightly larger (right) than the critical J_*. The intermediate, unstable fixed point is clearly visible. The arrows mark the CFT predictions for the location of the energy levels.

$2I$	$2S$	Q	Z_2	TIM	$x - 3/16$	E_{NRG}
0	1	0	0	3/80	0	0.000000
1	0	1/4	1/16	0	1/8	0.126716
1	0	1/4	1/16	0	1/8	0.128870
1	2	1/4	0	3/80	1/2	0.498068
1	0	1/4	0	7/16	1/2	0.498105
0	1	1/2	0	3/80	1/2	0.499241
2	1	1/2	0	3/80	1/2	0.499241
0	1	0	1/2	3/80	1/2	0.500586
0	1	1/2	1/16	1/10	5/8	0.624506
2	1	1/2	1/16	1/10	5/8	0.624506
0	1	1/2	1/16	1/10	5/8	0.625623
2	1	1/2	1/16	1/10	5/8	0.625623
1	2	1/4	1/16	1/10	5/8	0.628025
1	2	1/4	1/16	1/10	5/8	0.628167

Table 4.2: Lowest energy states as obtained by CFT and NRG for the fixed point $(S_1, S_2, S_3) = (0, 1, 0)$. The states are given with their total isospin I and spin S. The columns Q, Z_2 and TIM indicate the contributions from the charge, the Ising and the TIM CFT respectively.

Hence, while bath 1 and 3 are still antiferromagnetically coupled, the coupling with bath 2 turns effectively ferromagnetic. The ordinary one-loop renormalization group calculation would predict that the Kondo exchanges $J_K^{(1)} = J_K^{(3)} > 0$ flow towards strong coupling, while $J_K^{(2)} < 0$ flows towards zero. This suggests that a model with $J_K^{(1)} = J_K^{(3)} \gg -J_K^{(2)} > 0$ should behave asymptotically as (4.5). If $J_K^{(2)} = 0$ this is just the two-channel spin-1/2 impurity model [2, 3, 6], which is non Fermi-liquid with S-matrices $S_1 = S_3 = 0$. It is easy to realize that the small ferromagnetic $J_K^{(2)}$ transforms into an antiferromagnetic exchange with the spin-density operators of baths 1 and 3, which is irrelevant. Indeed, the operator $(\mathbf{J}_1+\mathbf{J}_2+\mathbf{J}_3)\cdot(\mathbf{J}_1-2\mathbf{J}_2+\mathbf{J}_3)$ has dimension 3/2. Consequently, we expect that this phase should be non-Fermi-liquid and identified by the S-matrices $(S_1, S_2, S_3) = (0, 1, 0)$, as is indeed confirmed by CFT. In addition, through the modular $\mathcal{S}$-matrix (see Section 2.7.2 and Appendix B), one can show that the zero-temperature entropy $S(0) = 1/2 \ln 2$ is finite and coincides with that of the S=1/2 two-channel Kondo model. Since $\sigma' \times \sigma' = I + \epsilon''$ and the dimension of ϵ'' is $3/2 > 1$, this fixed point is stable to symmetry-preserving perturbations. However, there are several symmetry-breaking relevant perturbations of dimension 1/2. One of them corresponds to the staggered magnetization

$$\mathbf{J}_1 - 2\mathbf{J}_2 + \mathbf{J}_3. \tag{4.6}$$

All the other relevant operators break the degeneracy between bath 1 and 3 as well. This is for instance the case for the spin-singlet operator

$$\mathbf{J}_2 \cdot (\mathbf{J}_1 - \mathbf{J}_3), \tag{4.7}$$

which is indeed known to be a relevant perturbation at the overscreened non-Fermi-liquid fixed point [8]. This phase extends at finite J' because a small J' does not generate any symmetry-breaking relevant perturbation.

The approach to the fixed point is controlled by two leading irrelevant operators of dimension 3/2: ϵ'' and the scalar product of the staggered magnetization (4.6) with the first spin descendant. Similarly to the overscreened two-channel Kondo model [2, 3], these operators produce logarithmic singularities in the impurity contribution to the specific heat coefficient and to the magnetic susceptibility, $C_{\mathrm{imp}}/T \sim \chi_{\mathrm{imp}} \sim \ln(1/T)$.

The Fixed Point $\phi^{-2}(-1, 1, -1)$

Since the Kondo screened phase $(-1, -1, -1)$ and the non-Fermi liquid phase $(0, 1, 0)$ are essentially different, an unstable critical line separates them (see Fig. 4.5). The NRG spectrum for this line is shown in the central part of Fig. 4.6 and the corresponding energy levels are reported in Table 4.3. We find that the NRG spectrum can be reproduced by fusing the $(1, 1, 1)$ fixed

$2I$	$2S$	Q	Z_2	TIM	$x-1/4$	E_{NRG}
0	1	0	0	1/10	0	0.000000
1	0	1/4	1/16	3/80	1/10 (×2)	0.100321
1	2	1/4	0	0	2/5	0.396747
0	1	0	1/2	0	2/5	0.400154
0	1	1/2	0	0	2/5	0.400259
2	1	1/2	0	0	2/5	0.400259
0	1	1/2	1/16	3/80	1/2 (×2)	0.499136
2	1	1/2	1/16	3/80	1/2 (×2)	0.499136
1	2	1/4	1/16	3/80	1/2 (×2)	0.501840
0	3	0	0	1/10	3/5	0.597377
1	0	1/4	1/2	1/10	3/5	0.597432
1	0	3/2	0	1/10	3/5 (×2)	0.597512
3	0	3/2	0	1/10	3/5	0.597512
1	0	1/4	0	3/5	3/5	0.606210
0	1	1/2	1/16	7/16	9/10 (×2)	0.908031
2	1	1/2	1/16	7/16	9/10 (×2)	0.908031
1	2	1/4	1/16	7/16	9/10 (×2)	0.914685

Table 4.3: Lowest energy states as obtained by CFT and NRG for the unstable fixed point $(S_1, S_2, S_3) = \phi^{-2}(-1, 1, -1)$. The states are given with their total isospin I and spin S. The columns Q, Z_2 and TIM indicate the contributions from the charge, the Ising and the TIM CFT respectively.

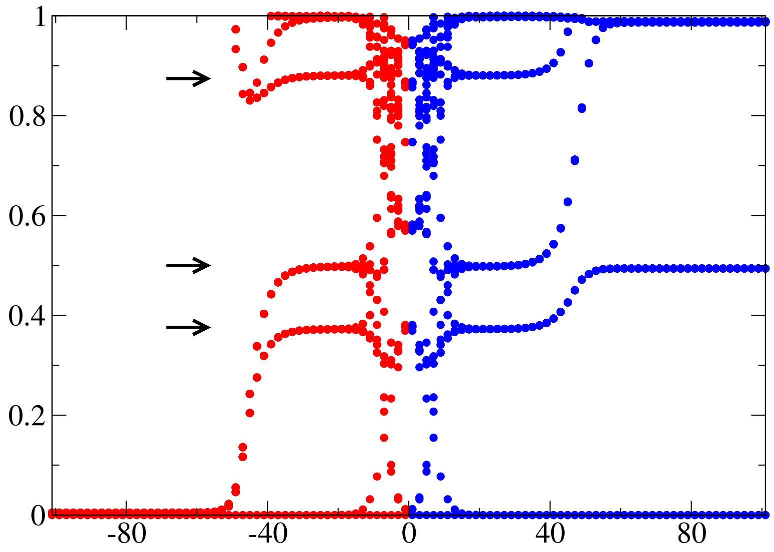

Figure 4.7: Flow diagrams for $J = 0.01$ and J' slightly smaller (left) and slightly larger (right) than the critical J'_*. The intermediate, unstable fixed point is clearly visible. The arrows mark the CFT predictions for the location of the energy levels.

point with the $j = 3/2$ primary field of the $SU(2)_3$ CFT and with the field ϵ of the TIM. The S-matrices are $\phi^{-2}(-1, 1, -1)$ and the residual entropy is $S(0) = \ln\phi$, where $\phi = (1 + \sqrt{5})/2$ is the golden ratio. Since $\epsilon \times \epsilon = I + t$, the operator which moves away from the critical line has dimension $3/5$. In other words, a small deviation δ from the line introduces a cross-over energy scale $\delta^{5/2}$. The most relevant symmetry-breaking operator is still the staggered magnetization (4.6), which now has dimension $2/5$. Once more, the approach to this fixed point is controlled by the scalar product of the staggered magnetization with the first Kac-Moody descendant of the $SU(2)_3$ CFT, which has dimension $1 + 2/5$. Analogously to the multichannel Kondo [2, 3], this operator produces impurity contributions to the specific-heat coefficient and magnetic susceptibility that diverge like $T^{-1/5}$.

The spin-singlet operator (4.7) is also relevant, although with a smaller dimension $3/5$. In addition, there is a new class of dimension-$3/5$ operators which correspond to coupling into a spin-singlet two particles, or one hole and one particle, belonging to bath 2 and either bath 1 or 3. This implies two important features: (*i*) This fixed point, like the dimer one, is destabilized by a single-particle hybridization between the baths, hence it would never be reachable in a model of coupled Anderson impurities, as we expected; (*ii*) The inter-bath Cooper pairing instability is again enhanced, like in the dimer model.

$2I$	$2S$	Q	Z_2	TIM	$x - 5/16$	E_{NRG}
1	0	1/4	1/16	0	0	0.00000
0	1	0	1/16	1/10	0	0.00001
0	1	1/2	0	3/80	3/8 (×2)	0.37234
2	1	1/2	0	3/80	3/8 (×2)	0.37234
1	0	1/4	0	7/16	3/8 (×2)	0.37245
1	2	1/4	0	3/80	3/8 (×2)	0.37245
0	1	0	1/16	3/5	1/2	0.49748
0	3	0	1/16	0	1/2	0.49748
1	2	1/4	1/16	1/10	1/2	0.49765
0	1	1/2	1/16	1/10	1/2	0.49797
2	1	1/2	1/16	1/10	1/2	0.49797
1	0	3/4	1/16	0	1/2 (×2)	0.49813
3	0	3/4	1/16	0	1/2	0.49813
0	1	1/2	1/2	3/80	7/8 (×2)	0.88039
2	1	1/2	1/2	3/80	7/8 (×2)	0.88039
1	0	1/4	1/2	7/16	7/8 (×2)	0.88048
1	2	1/4	1/2	3/80	7/8 (×2)	0.88048

Table 4.4: Lowest energy states as obtained by CFT and NRG for the fixed point $(S_1, S_2, S_3) = (0, -1, 0)$. The states are given with their total isospin I and spin S. The columns Q, Z_2 and TIM indicate the contributions from the charge, the Ising and the TIM CFT respectively.

The Fixed Points $(1, -1, 1)$ and $(0, -1, 0)$

These two fixed points occur when $J' > J$ is larger or comparable to the Kondo temperature. They have a simple explanation. Indeed, when $J = 0$, site 2 is only coupled to bath 2 with a Kondo exchange, leading to a full screening, i.e. $S_2 = -1$. Sites 1 and 3 plus their own baths realize once more a two-impurity Kondo model which, as discussed before, has two stable regimes. One regime, for $J' \ll T_K$, is Kondo screened and has $S_1 = S_3 = -1$ so that it is described by the fixed point $(S_1, S_2, S_3) = (-1, -1, -1)$ (see Fig. 4.5). The other regime, $J' \gg T_K$, has $(S_1, S_2, S_3) = (1, -1, 1)$ in Fig. 4.5. These two regimes are clearly stable towards switching on a small $J \ll J'$. When $J = 0$, we also know that an unstable fixed point at $J' = J'_* \sim T_K$ separates these two stable phases and is identified by $S_1 = S_3 = 0$, hence the label $(0, -1, 0)$ in Fig. 4.5. Since site 2 is tightly bound into a singlet state with bath 2, a finite but small $J \ll T_K$ will simply generate a ferromagnetic exchange of order $-J^2/T_K$ by virtually exciting the singlet state. The net effect is that the unstable fixed point at $J = 0$ is just the endpoint of another critical line which, for $J \ll T_K$, moves to larger values of J'. This has been checked by the NRG calculations, and we show the flow diagram around this line in Fig. 4.7. From the CFT viewpoint, the $(1,-1,1)$ or $(0,-1,0)$ fixed points can be obtained by fusing with the $j=3/2$ primary field of the $SU(2)_3$ and with ϵ'' of the TIM or σ_I of the Ising CFT, respectively. For comparison, we report the energies obtained by NRG at the fixed point $(0,-1,0)$ in Table 4.4. The properties of the unstable $(0,-1,0)$ critical line are the same as those of the dimer critical point. In particular, there is a relevant operator in the singlet Cooper channel that now involves pairing among baths 1 and 3, as well as an equally relevant operator which corresponds to an opposite magnetization of bath 1 and 3, i.e. $\mathbf{J}_1 - \mathbf{J}_3$.

4.3.3 Concluding Remarks About the Trimer

We have shown that the trimer model (4.3) has quite a rich phase diagram, drawn in Fig. 4.5. Besides the three different stable phases, we have found two unstable critical lines with some notable features:

(1) Both critical lines turn into crossover regions, which we believe should be sharp, if instead of three coupled spin-1/2 Kondo impurities we had considered three Anderson impurities, with an on-site Hubbard U, coupled by a hopping t between sites 2 and 1 and 2 and 3, and a hopping t' between sites 1 and 3.

(2) Both lines are unstable towards a magnetic symmetry breaking determined by the largest among J and J', namely $\mathbf{J}_1 - 2\mathbf{J}_2 + \mathbf{J}_3$ for $J > J'$ and $\mathbf{J}_1 - \mathbf{J}_3$ for $J' > J$.

(3) Both lines are also unstable in a singlet Cooper channel. In particular, for $J > J'$ along the critical line $\phi^{-2}(-1,1,-1)$, the instability channel corresponds to an inter-site pairing along bonds 1-2 and 2-3. On the contrary, along the line $(0,-1,0)$ for $J' > J$, it is the inter-site pairing along bond 1-3 which is singular.

The Trimer with C_3 Symmetry and the Hubbard Model on a Triangular Lattice

Let us conclude by noting that, for $J = J'$, the trimer is actually the simplest cluster to simulate, within DMFT, a Hubbard model on a triangular lattice. Yet, as we mentioned several times, the trimer representative of a Hubbard model very close to a Mott transition, necessarily includes, besides the inter-impurity exchange $J = J'$, a weak inter-bath hybridization, generally invariant only under global $U(1)$ gauge-symmetry, $SU(2)$ spin-rotations as well as under C_3 symmetry.

A trimer coupled to three baths with C_3 symmetry was studied by NRG by Paul and Ingersent [97], who found a phase diagram which contains three stable phases: the perfectly Kondo screened phase, our $(-1,-1,-1)$ fixed point, and two non-Fermi-liquid regimes, which they denoted as *Isospin-Kondo* and *Frustrated-Kondo*. In other words, the $(-1,-1,-1)$ fixed point at $J = J'$ is destabilized by an hybridization among the baths that preserves the C_3 symmetry, provided it is large compared with the Kondo temperature. Translated within DMFT language, this should imply that the instability of the $(-1,-1,-1)$ fixed point is very likely to be encountered by the trimer, representative of a Hubbard model on a triangular lattice, on the way to the Mott insulating phase, $T_K \to 0$. Which of the two non-Fermi-liquid regimes may occur depends on the density of states at the Fermi energy projected onto the three helicity states, $h = 0, \pm 1$, of the cluster

$$\rho_h = \frac{1}{V}\sum_{\mathbf{k}} \delta\left(\epsilon_{\mathbf{k}} - \epsilon_F\right) \left|1 + \mathrm{e}^{ih2\pi/3}\,\mathrm{e}^{i\mathbf{k}\cdot\mathbf{a}} + \mathrm{e}^{-ih2\pi/3}\,\mathrm{e}^{i\mathbf{k}\cdot\mathbf{b}}\right|^2,$$

where $\epsilon_{\mathbf{k}}$ is the band energy of the triangular lattice, while $\mathbf{a} = (1,0)$ and $\mathbf{b} = (1/2, \sqrt{3}/2)$ are the unit lattice vectors. For the standard Hubbard model with real nearest-neighbor hopping, $\rho_{\pm 1} > \rho_0$. This suggests that the non-Fermi-liquid phase pertinent to this case is likely the *Isospin-Kondo* regime. The *Frustrated-Kondo* regime, which requires $\rho_0 > \rho_{\pm 1}$, might occur for instance on a triangular lattice with purely imaginary nearest-neighbor hopping. Incidentally, this is quite a peculiar model in which, although parity and time reversal are broken, but not their product, particle-hole symmetry is preserved.

In both cases, the approach to the Mott transition should be influenced by the critical point which separates the Fermi-liquid phase from the non-Fermi-liquid one. However, the conformal embedding we have adopted so far is no longer appropriate to describe both these critical points as well as the *Isospin-Kondo* and the *Frustrated-Kondo* regimes, since it assumes independent charge conservation in each bath. The correct embedding has recently been found by Ingersent *et al.* [55], although it has been used only to discuss the *Isospin-* and *Frustrated-Kondo* regimes and not the two unstable fixed points, which would be of interest in connection with cluster DMFT.

4.4 The Impurity Tetramer

The other cluster that we consider is an impurity tetramer, as drawn in Fig. 4.8. The properties of this cluster are still under current investigation and we present hereunder the preliminary results that we have obtained. The Hamiltonian is given by

$$\mathcal{H} = \sum_{a=1}^{4} \mathcal{H}_a^K + J\left(\mathbf{S}_1 + \mathbf{S}_3\right)\cdot\left(\mathbf{S}_2 + \mathbf{S}_4\right) + J'\left(\mathbf{S}_1\cdot\mathbf{S}_3 + \mathbf{S}_2\cdot\mathbf{S}_4\right). \tag{4.8}$$

This model describes four spin-1/2 impurities, coupled together by a nearest J, and next-nearest neighbor J', antiferromagnetic exchanges. In addition,

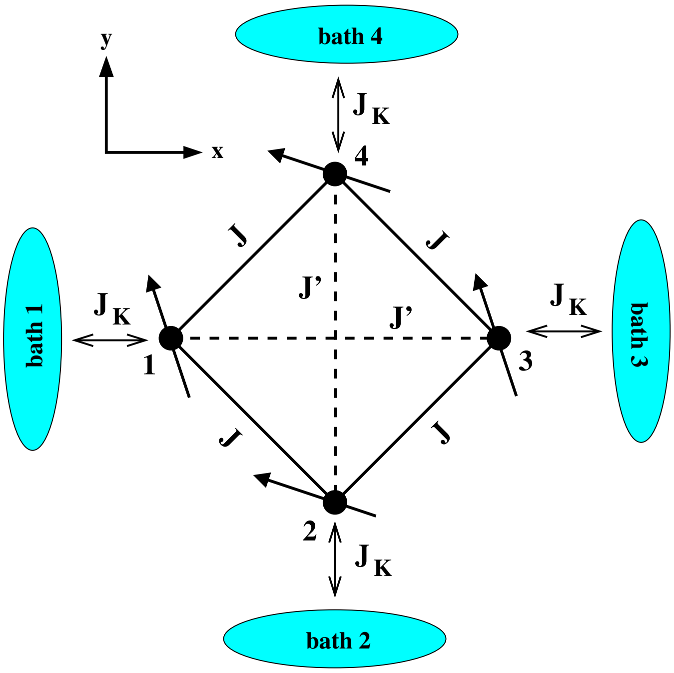

Figure 4.8: The impurity tetramer with the Hamiltonian 4.8.

each spin is Kondo coupled to its conduction bath by $J_K > 0$. The four baths are degenerate and particle-hole invariant. Clearly, the tetramer can be used to represent the Hubbard model on a square lattice within the framework of cluster DMFT. Again, one should in principle consider Anderson impurities, but in order to facilitate the identification of fixed points, we prefer to use Kondo impurities and discuss the effect of the hybridization between the baths by treating it as a perturbation.

4.4.1 CFT Preliminaries for the Tetramer

As usual, given our choice of the model (4.8), the charge degrees of freedom can be described by four independent $SU(2)_1$ CFTs, one for each bath. For the spin symmetry, the way the impurities are coupled by the direct exchange naturally leads to the following conformal embedding scheme: First, we couple the spin sectors of baths 1 and 3 into an overall $SU(2)_2 \times Z_2$ as in the case of the impurity trimer. The same procedure is applied to the baths 2 and 4 and we get

$$\begin{aligned} &\left(SU(2)_1^{(1)} \times SU(2)_1^{(3)}\right) \times \left(SU(2)_1^{(2)} \times SU(2)_1^{(4)}\right) \\ &\to \left(SU(2)_2^{(1-3)} \times Z_2^{(1)}\right) \times \left(SU(2)_2^{(2-4)} \times Z_2^{(2)}\right) . \end{aligned}$$

Field	Dimension	
I	0	x^2+y^2
θ	1	$xy(x^2-y^2)$
$\phi_{3/2}$	3/2	$x(x^2-y^2)$; $y(x^2-y^2)$
$\phi_{1/24}$	1/24	
$\phi_{1/6}$	1/6	x; y
$\phi_{3/8}$	3/8	
$\phi_{2/3}$	2/3	x^2-y^2; xy
$\phi_{25/24}$	25/24	
$\sigma^{(i=1,2)}$	1/16	
$\tau^{(i=1,2)}$	9/16	

Table 4.5: Primary fields of the $c=1$ CFT with their dimensions. Some fields transform according to irreducible representations of C_{4v} and the corresponding functions of coordinates are shown in the last column.

The two $SU(2)_2$ are then coupled together into an $SU(2)_4$ and leave behind a CFT with central charge $c=1$. The resulting embedding is

$$SU(2)_4 \times Z_2^{(1)} \times Z_2^{(2)} \times \Big[c = 1 \text{ (CFT)}\Big],$$

where $c=1$ CFT stands for the Z_2 orbifold of a free bosonic CFT [9, 35] with compactification radius $R=\sqrt{12}$. This embedding can again be proven rigorously through the character decomposition, as shown in Appendix A.

The $c=1$ CFT contains 13 primary fields, some of them being twice degenerate. We list them with their dimension in Table 4.5. Some of the primary fields transform like irreducible representations of the C_{4v} symmetry group and we indicate, in Table 4.5, the functions of coordinates that transform in the same way. The fusion rules between the primary fields can be found in Ref. [35, p. 784].

4.4.2 Fixed Points in the Tetramer Phase Diagram

In Fig. 4.9, we sketch the phase diagram of (4.8) as obtained by NRG. The calculations were performed with $\Lambda = 10$. We use the spin symmetry and the conservation of charge in all four channels. At every NRG iteration, ~ 2000 states are kept. As before, each fixed point of the renormalization group is identified by the S-matrices $(S_1, S_2, S_3, S_4)^{(n)}$, where the superscript (n) is introduced to distinguish between different fixed points with the same S-matrices. Let us describe the different fixed points that we find.

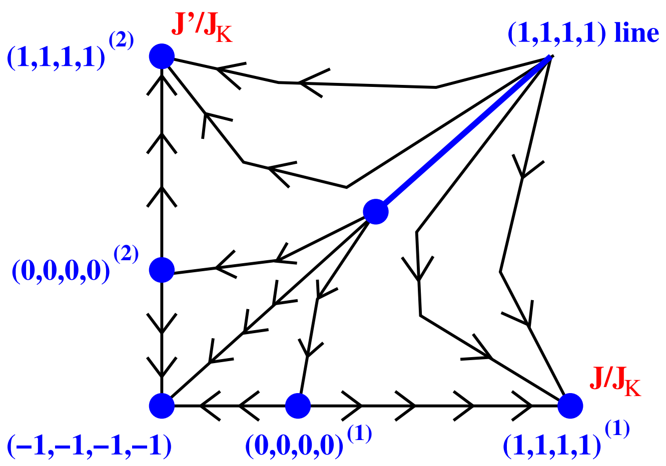

Figure 4.9: NRG phase diagram of the impurity tetramer described by the Hamiltonian (4.8).

The Fixed Point $(-1,-1,-1,-1)$

This fixed point corresponds to a perfectly Kondo-screened phase. It occurs when T_K is large as compared to both J and J', and can again be obtained by fusing the $J_K=0$ spectrum with the highest weight representation of the $SU(2)_4$ with $j=2$. We will use this screened $(-1,-1,-1,-1)$ fixed point as the ancestor BC to generate all the other BCs by fusion.

The Fixed Point $(1,1,1,1)^{(1)}$

If $J'=0$ and $J \gg T_K$, the tetramer locks into a non-degenerate singlet state which is obtained by coupling sites 1 and 3 into a triplet, as well as sites 2 and 4, and coupling the two triplets into an overall singlet. This configuration decouples from the conduction electrons which do not feel the presence of the impurities anymore. This phase (see Fig. 4.9) is Fermi-liquid like and remains stable even in the presence of a finite J', provided the lowest excitation gap from the ground state of the isolated tetramer is much larger than T_K. Within CFT, there are several possible fusions which turn the $(-1,-1,-1,-1)$ fixed point into this new one. One possibility is a fusion with the primary field θ of the $c=1$ CFT.

The Fixed Point $(0,0,0,0)^{(1)}$

The two stable fixed points for $J \ll J_K$ and $J \gg J_K$ at $J' \ll J$ are essentially different and we expect that they are separated by a critical line (see Fig. 4.9). This is confirmed by the NRG computation and the spectrum for

$2I$	$2S$	Q	$Z_2^{(1)}$	$Z_2^{(2)}$	$c=1$	$x-1/6$	E_{NRG}
0	0	0	0	0	1/6	0	0.00000
0	2	0	0	0	1/6	1/3	0.33123
1	1	1/4	1/16	0	1/16	1/3 (×2)	0.33898
1	1	1/4	0	1/16	1/16	1/3 (×2)	0.33898
0	0	1/2	1/16	1/16	1/24	1/2 (×4)	0.49602
2	0	1/2	1/16	1/16	1/24	1/2 (×4)	0.49602
0	2	0	1/2	0	0	2/3	0.67050
0	2	0	0	1/2	0	2/3	0.67050
0	2	1/2	0	0	0	2/3 (×2)	0.67050
2	2	1/2	0	0	0	2/3 (×2)	0.67050
1	1	1/4	1/16	0	9/16	5/6 (×2)	0.81649
1	1	1/4	0	1/16	9/16	5/6 (×2)	0.81649
1	1	3/4	0	1/16	1/16	5/6 (×4)	0.81649
3	1	3/4	0	1/16	1/16	5/6 (×2)	0.81649
1	1	3/4	1/16	0	1/16	5/6 (×4)	0.81649
3	1	3/4	1/16	0	1/16	5/6 (×2)	0.81649
1	3	1/4	1/16	0	1/16	5/6 (×2)	0.82156
1	3	1/4	0	1/16	1/16	5/6 (×2)	0.82156
0	2	1/2	1/16	1/16	1/24	5/6 (×4)	0.84007
2	2	1/2	1/16	1/16	1/24	5/6 (×4)	0.84007
1	1	1/4	1/16	1/2	1/16	5/6 (×2)	1.01981
1	1	1/4	1/2	1/16	1/16	5/6 (×2)	1.01981

Table 4.6: Lowest energy states as obtained by CFT and NRG for the unstable fixed point $(S_1, S_2, S_3, S_4) = (0,0,0,0)^{(1)}$. The states are given with their total isospin I and spin S. The columns Q, $Z_2^{(a)}$ and $c=1$ indicate the contributions from the charge, the Ising and the $c=1$ CFT respectively.

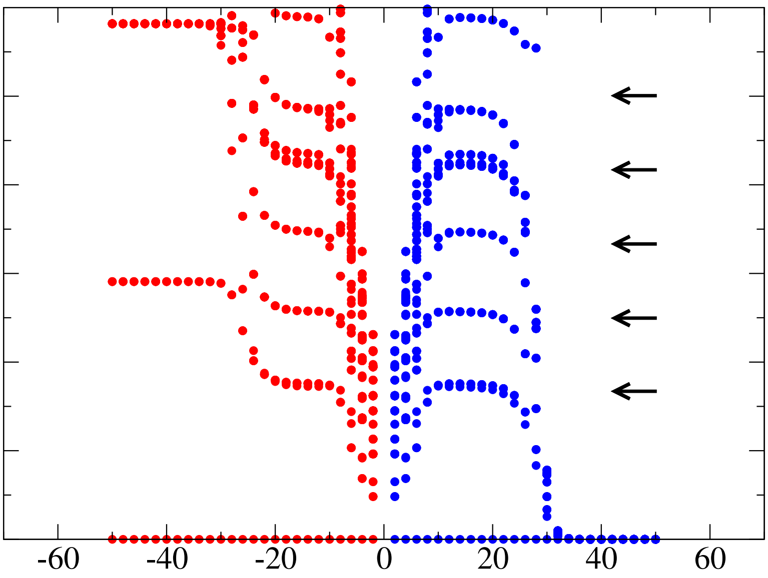

Figure 4.10: Flow diagrams for $J' = 0$ and J slightly smaller (left) and slightly larger (right) than the critical J_*. The intermediate, unstable fixed point is clearly visible. The arrows mark the CFT predictions for the location of the energy levels.

this fixed point is shown in Fig. 4.10. The corresponding energies are reported in Table 4.6. We find that the NRG spectrum can be reproduced by fusing the $(-1,-1,-1,-1)$ BC with the primary field $\phi_{1/6}$ of the $c = 1$ CFT. By the modular $\mathcal{S}$-matrix (see Appendix B), we find that the S-matrices are $(0,0,0,0)$ and the residual entropy is $S(0) = \ln 2$.

Since $\phi_{1/6} \times \phi_{1/6} = I + \theta + \phi_{2/3}$, the operator which moves away from the critical line has dimension $2/3$. The most relevant symmetry-breaking operator corresponds to the staggered magnetization

$$\mathbf{J}_1 - \mathbf{J}_2 + \mathbf{J}_3 - \mathbf{J}_4, \tag{4.9}$$

with dimension $1/3$. Besides the staggered magnetization, there are other less relevant operators of dimension $2/3$. Some of them are four-fermion operators obtained by coupling into a spin-singlet the staggered magnetization with other spin-triplet excitations, such as the operator

$$\left(\mathbf{J}_1 - \mathbf{J}_3\right) \cdot \left(\mathbf{J}_1 - \mathbf{J}_2 + \mathbf{J}_3 - \mathbf{J}_4\right).$$

The other relevant operators of dimension $2/3$ correspond to all possible mean-field decoupling schemes of the exchange term

$$\left(\mathbf{J}_1 + \mathbf{J}_3\right) \cdot \left(\mathbf{J}_2 + \mathbf{J}_4\right),$$

$2I$	$2S$	Q	$Z_2^{(1)}$	$Z_2^{(2)}$	$c=1$	$x-1/8$	E_{NRG}
0	0	0	1/16	1/16	0	0	0.00000
1	1	1/4	1/16	0	1/16	3/8 (×2)	0.37800
1	1	1/4	0	1/16	1/16	3/8 (×2)	0.37800
0	2	0	1/16	1/16	1/6	1/2 (×2)	0.46976
0	0	1/2	1/16	1/16	0	1/2 (×2)	0.47207
2	0	1/2	1/16	1/16	0	1/2 (×2)	0.47207
0	0	1/2	0	0	3/8	3/4 (×4)	0.78136
2	0	1/2	0	0	3/8	3/4 (×4)	0.78136
0	2	1/2	0	0	1/24	3/4 (×4)	0.78137
2	2	1/2	0	0	1/24	3/4 (×4)	0.78137
1	1	1/4	0	1/16	9/16	7/8 (×2)	0.88754
1	1	1/4	1/16	0	9/16	7/8 (×2)	0.88754
1	3	1/4	0	1/16	1/16	7/8 (×2)	0.88755
1	3	1/4	1/16	0	1/16	7/8 (×2)	0.88755
1	1	3/4	0	1/16	1/16	7/8 (×4)	0.89000
3	1	3/4	0	1/16	1/16	7/8 (×2)	0.89000
1	1	3/4	1/16	0	1/16	7/8 (×4)	0.89000
3	1	3/4	1/16	0	1/16	7/8 (×2)	0.89000
1	1	1/4	1/16	1/2	1/16	7/8 (×2)	1.09484
1	1	1/4	1/2	1/16	1/16	7/8 (×2)	1.09484

Table 4.7: Lowest energy states as obtained by CFT and NRG for the unstable fixed point $(S_1, S_2, S_3, S_4) = (0, 0, 0, 0)^{(2)}$. The states are given with their total isospin I and spin S. The columns Q, $Z_2^{(a)}$ and $c = 1$ indicate the contributions from the charge, the Ising and the $c = 1$ CFT respectively.

into inter-bath bilinear operators. Among them, we just mention the inter-bath hopping

$$\sum_\sigma \left(c_{1\sigma}^\dagger + c_{3\sigma}^\dagger\right)\left(c_{2\sigma} + c_{4\sigma}\right) + H.c.,$$

as well as the d-wave Cooper pairing[1]

$$\left(c_{1\uparrow}^\dagger - c_{3\uparrow}^\dagger\right)\left(c_{2\downarrow}^\dagger - c_{4\downarrow}^\dagger\right) - (\uparrow\leftrightarrow\downarrow).$$

---

[1] In the reference frame of Fig. 4.8 this corresponds to a Cooper pair of d_{xy} symmetry. However, in the reference frame conventionally used for square lattices, which is rotated by 90 degrees, it corresponds to $d_{x^2-y^2}$.

The Fixed Points $(1,1,1,1)^{(2)}$ and $(0,0,0,0)^{(2)}$

If $J=0$, sites 1 and 3 are decoupled from sites 2 and 4, hence the tetramer reduces to two independent Kondo dimers. If $J' \gg T_K$ each pair of impurities, 1 and 3 or 2 and 4, is strongly bound into a singlet which decouples from the conduction electrons. This fixed point is clearly stable to switching on a small J. Hence, in analogy with the dimer, one should obtain it from the $(-1,-1,-1,-1)$ fixed point upon fusion with $\epsilon_I^{(1)}\,\epsilon_I^{(2)}$, where $\epsilon_I^{(a)}$, $a=1,2$, are the energy operators of the two Ising CFTs. The NRG spectrum agrees with this prediction, not only for small J, but for the whole region $J' > J$ with $J' \gg T_K$, see Fig. 4.9. Once again, this unscreened regime is separated from the Kondo regime by a critical line which is the same as in the impurity dimer. It is therefore obtained [5] from the $(-1,-1,-1,-1)$ fixed point upon fusion with $\sigma_I^{(1)}\,\sigma_I^{(2)}$ and it is identified by zero scattering matrices $(0,0,0,0)^{(2)}$ (see Fig. 4.9), and by a residual entropy $S(0)=\ln 2$. The energies obtained by NRG for this fixed point are shown in Table 4.7 and agree well with the CFT prediction. Besides the dimension-1/2 operator which moves away from this critical point, there are several symmetry-breaking perturbations with the same dimension: the direct hybridization among baths 1 and 3, as well as among 2 and 4; the spin magnetization $\mathbf{J}_1-\mathbf{J}_3$ and $\mathbf{J}_2-\mathbf{J}_4$; the 1-3 and 2-4 inter-bath singlet Cooper pairing.

The $(1,1,1,1)$ Line

If $J=J' \gg T_K$, the tetramer locks into a doubly degenerate spin-singlet state. One state in the doublet is the singlet formed by two triplets, one between sites 1 and 3, the other between sites 2 and 4. In our reference frame, (see Fig. 4.8) this state has x^2-y^2 symmetry. The second state is instead the product of two singlets, between sites 1 and 3 and between 2 and 4. It transforms like the product $x\,y$. The Kondo exchange provides a coupling between these two configurations only at second order in J_K, which is an irrelevant quartic conduction-electron operator. Therefore, the tetramer decouples asymptotically from the conduction baths, and its degeneracy remains unchanged. This is confirmed by the NRG calculation, which shows the same Fermi-liquid spectrum as in the absence of the impurity-cluster except that every state is doubly degenerate. This phase is the analogous of a first-order line, hence the label "$(1,1,1,1)$ line" in Fig. 4.8, and the splitting of the double degeneracy of the tetramer is described by a relevant operator of dimension 0.

The Intermediate Fixed Point

The NRG calculations show that the two critical lines corresponding to the fixed points $(0,0,0,0)^{(1,2)}$ merge together at an unstable fixed point which is the ending point of the $(1,1,1,1)$ line. This fixed point is unstable in all directions and it has so far been impossible to find compatible BCs and low-energy spectrum. A more precise identification of this fixed point is under current investigation.

4.5 Conclusions

In this chapter, we have studied two clusters of impurities by means of Wilson's numerical renormalization group and conformal field theory. Even if the two clusters are different, the phase diagrams of the impurity trimer and tetramer share striking similarities. In both cases, stable phases are separated by critical lines that show non-Fermi liquid behavior. The unstable fixed points emerge from the competition between the Kondo effect that gains energy if the ground state is degenerate and the RKKY interaction that splits this degeneracy. As a result, these fixed points have many instabilities, but magnetism always appears as being the most relevant one. Actually, going from the trimer to the tetramer, the magnetic instability becomes even more relevant. Besides magnetization, Cooper-pair instabilities are also present.

Let us discuss what might be the effects of these instabilities if these clusters were used to emulate a Hubbard model on a square lattice within cluster DMFT. Clearly, such a discussion is quite speculative at this point, but, as we have discussed in Section 4.1, even neglecting the self-consistency found in DMFT, the local instabilities of the cluster might still transform into bulk instabilities of the lattice model. Another aspect comes from considering Kondo impurities, whereas the appropriate model would display Anderson impurities. In this case, we believe that the true critical lines would turn into sharp crossover regions that are stable against particle-hole symmetry breaking, as was observed in Ref. [34]. As the lattice model approaches the Mott transition, its effective Fermi temperature T_F^* goes to zero, as does the corresponding Kondo temperature T_K of the impurity model. At some point, the Kondo temperature and the energy scales of the RKKY interactions become of the same order and the system enters into the crossover regions of the impurity model. Note that while finding these critical regions requires a fine tuning of the parameters in the impurity model, they are always crossed if it is possible to continuously approach the Mott transition. In the lattice model, these regions are translated into pseudo-gap phases that are controlled by several energy scales [34] and occur before the Mott transition. It is reasonable to think that, if the system is free to break symmetries, it would react to these unstable phases by developing some order corresponding to the most relevant instabilities of the impurity model. From our study, it is clear that developing antiferromagnetism is the most natural way to break the symmetry, at least at half-filling. However, if the model is not at half-filling, as when it is doped, other symmetry breakings might occur, like the formation of Cooper pairs [26], that we found to always be relevant perturbations at the unstable fixed points.

Actually, in the mechanisms behind the Kondo effect, there is always some sort of singlet formation, either between the conduction bath and the impurities, or between the impurities themselves. Therefore, the pairing mechanism is always present and it is not surprising that it can appear in the lattice model.

In conclusion, we expect that the competition between the Kondo effect and other local interactions is a very generic feature that is found in all impurity-cluster models. The consequences of this competition can be seen whenever it is possible to drive a system smoothly to its Mott transition. Therefore, we believe that it plays a key role in understanding the rich physics observed in materials on the verge of a Mott transition.

Appendix A

Character Decompositions

The conformal embeddings of Chapter 4 can be justified by the Goddard-Kent-Olive construction [35], in which a coset conformal field theory is built from a Wess-Zumino-Witten (WZW) model with Lie group symmetry g by stripping off the part of the model corresponding to a subalgebra p of g. The cosets we are interested in have the form

$$\frac{SU(2)_N \times SU(2)_L}{SU(2)_{N+L}},$$

and describe a rational conformal field theory. The central charge of the coset is the difference of the two WZW components and, if it is smaller than 1, it has to correspond to a minimal model. Decomposing the representations of $SU(2)_N \times SU(2)_L$ with respect to

$$SU(2)_{N+L} \times \frac{SU(2)_N \times SU(2)_L}{SU(2)_{N+L}},$$

it is possible [14] to express the characters of the coset and $SU(2)_{N+L}$ as a function of the characters of $SU(2)_N$ and $SU(2)_L$.

A.1 The Impurity Trimer

When the impurities are disconnected ($J_K = 0$) in the trimer, the partition function for an even chain reads

$$Z = \sum_{j_n=0,1} \left(\chi^{(1)}_{j_1}\chi^{(1)}_{j_2}\chi^{(1)}_{j_3}\right)_{\text{charge}} \left(\chi^{(1)}_{j_1}\chi^{(1)}_{j_2}\chi^{(1)}_{j_3}\right)_{\text{spin}}, \tag{A.1}$$

where $\chi^{(1)}_j$ is the character of the conformal tower with highest weight state of spin $2j$ in $SU(2)_1$ and both the charge and spin sectors are described by a CFT with symmetry

$$SU(2)^{(1)}_1 \times SU(2)^{(2)}_1 \times SU(2)^{(3)}_1.$$

The character decomposition allows to identify the free energy of this original theory and the one in which the symmetry has been decomposed. In the case of the impurity trimer, a first decomposition is obtained by

$$SU(2)_1 \times SU(2)_1 \sim SU(2)_2 \times \frac{SU(2)_1 \times SU(2)_1}{SU(2)_2}.$$

Here the coset has central charge $c = 1/2$ and corresponds to the Ising model Z_2. In the second decomposition

$$SU(2)_2 \times SU(2)_1 \sim SU(2)_3 \times \frac{SU(2)_2 \times SU(2)_1}{SU(2)_3},$$

the coset has central charge $c = 7/10$ which is recognized as the tricritical Ising model (TIM). The character decomposition for the embedding

$$SU(2)_1 \times SU(2)_1 \times SU(2)_1 \sim SU(2)_3 \times (\mathrm{TIM}) \times Z_2$$

is given by

$$\begin{aligned}
\chi_0^{(1)}\chi_0^{(1)}\chi_0^{(1)} &= \chi_0^{(3)}\left(\chi_0^{I}\chi_0^{\mathrm{TIM}} + \chi_{1/2}^{I}\chi_{3/2}^{\mathrm{TIM}}\right) + \chi_2^{(3)}\left(\chi_0^{I}\chi_{3/5}^{\mathrm{TIM}} + \chi_{1/2}^{I}\chi_{1/10}^{\mathrm{TIM}}\right)\\
\chi_1^{(1)}\chi_1^{(1)}\chi_1^{(1)} &= \chi_1^{(3)}\left(\chi_{1/2}^{I}\chi_{1/10}^{\mathrm{TIM}} + \chi_0^{I}\chi_{3/5}^{\mathrm{TIM}}\right) + \chi_3^{(3)}\left(\chi_0^{I}\chi_0^{\mathrm{TIM}} + \chi_{1/2}^{I}\chi_{3/2}^{\mathrm{TIM}}\right)\\
\chi_1^{(1)}\chi_0^{(1)}\chi_0^{(1)} &= \chi_0^{(1)}\chi_0^{(1)}\chi_1^{(1)} = \chi_1^{(3)}\chi_{1/16}^{I}\chi_{3/80}^{\mathrm{TIM}} + \chi_3^{(3)}\chi_{1/16}^{I}\chi_{7/16}^{\mathrm{TIM}}\\
\chi_1^{(1)}\chi_1^{(1)}\chi_0^{(1)} &= \chi_0^{(1)}\chi_1^{(1)}\chi_1^{(1)} = \chi_0^{(3)}\chi_{1/16}^{I}\chi_{7/16}^{\mathrm{TIM}} + \chi_2^{(3)}\chi_{1/16}^{I}\chi_{3/80}^{\mathrm{TIM}}\\
\chi_1^{(1)}\chi_0^{(1)}\chi_1^{(1)} &= \chi_0^{(3)}\left(\chi_{1/2}^{I}\chi_0^{\mathrm{TIM}} + \chi_0^{I}\chi_{3/2}^{\mathrm{TIM}}\right) + \chi_2^{(3)}\left(\chi_{1/2}^{I}\chi_{3/5}^{\mathrm{TIM}} + \chi_0^{I}\chi_{1/10}^{\mathrm{TIM}}\right)\\
\chi_0^{(1)}\chi_1^{(1)}\chi_0^{(1)} &= \chi_1^{(3)}\left(\chi_0^{I}\chi_{1/10}^{\mathrm{TIM}} + \chi_{1/2}^{I}\chi_{3/5}^{\mathrm{TIM}}\right) + \chi_3^{(3)}\left(\chi_0^{I}\chi_{3/2}^{\mathrm{TIM}} + \chi_{1/2}^{I}\chi_0^{\mathrm{TIM}}\right).
\end{aligned}$$

Here, $\chi_j^{(k)}$ is the character of the conformal tower with highest weight state of spin $2j$ in $SU(2)_k$. The other characters have a superscript indicating the corresponding minimal model (I for the Ising model and TIM for tricritical Ising model) and a subscript giving their dimension. This formula expresses how the partition function (A.1) is written in terms of the characters of the decomposed theory.

A.2 The Impurity Tetramer

The partition function for the tetramer with disconnected impurities is given by

$$Z = \sum_{j_n=0,1} \left(\chi_{j_1}^{(1)}\chi_{j_2}^{(1)}\chi_{j_3}^{(1)}\chi_{j_4}^{(1)}\right)_{\mathrm{charge}} \left(\chi_{j_1}^{(1)}\chi_{j_2}^{(1)}\chi_{j_3}^{(1)}\chi_{j_4}^{(1)}\right)_{\mathrm{spin}}. \tag{A.2}$$

The symmetry of the theory is first decomposed by coupling two pairs of $SU(2)_1$ together and it involves a coset with the central charge of the Ising model, as in the impurity trimer. The remaining $SU(2)_2$ are then coupled according to

$$SU(2)_2 \times SU(2)_2 \sim SU(2)_4 \times \frac{SU(2)_2 \times SU(2)_2}{SU(2)_4}.$$

In this case, the coset has central charge $c = 1$ and we find that the NRG results are recovered by considering an orbifold Gaussian model with compactification radius $R = \sqrt{12}$. The resulting embedding

$$SU(2)_1 \times SU(2)_1 \times SU(2)_1 \times SU(2)_1 \sim SU(2)_4 \times Z_2 \times Z_2 \times \Big[c = 1 \text{ CFT}\Big],$$

has the following character decomposition:

$$\begin{aligned}
&\chi_0^{(1)}\chi_0^{(1)}\chi_0^{(1)}\chi_0^{(1)} = \\
&\qquad \chi_0^{(4)} \Big[\chi_0^{I_1}\chi_0^{I_2}\chi_I + \chi_{1/2}^{I_1}\chi_{1/2}^{I_2}\chi_\theta + \chi_0^{I_1}\chi_{1/2}^{I_2}\chi_{3/2}^{[1]} + \chi_{1/2}^{I_1}\chi_0^{I_2}\chi_{3/2}^{[2]}\Big] \\
&\qquad + \chi_2^{(4)} \Big[\Big(\chi_0^{I_1}\chi_0^{I_2} + \chi_{1/2}^{I_1}\chi_{1/2}^{I_2}\Big)\chi_{2/3} + \Big(\chi_0^{I_1}\chi_{1/2}^{I_2} + \chi_{1/2}^{I_1}\chi_0^{I_2}\Big)\chi_{1/6}\Big] \\
&\qquad + \chi_4^{(4)} \Big[\chi_0^{I_1}\chi_0^{I_2}\chi_\theta + \chi_{1/2}^{I_1}\chi_{1/2}^{I_2}\chi_I + \chi_0^{I_1}\chi_{1/2}^{I_2}\chi_{3/2}^{[2]} + \chi_{1/2}^{I_1}\chi_0^{I_2}\chi_{3/2}^{[1]}\Big]\,; \\
&\chi_1^{(1)}\chi_0^{(1)}\chi_0^{(1)}\chi_0^{(1)} = \chi_0^{(1)}\chi_1^{(1)}\chi_0^{(1)}\chi_0^{(1)} = \\
&\qquad \chi_1^{(4)} \Big[\chi_{1/16}^{I_1}\chi_0^{I_2}\chi_{1/16}^{[1]} + \chi_{1/16}^{I_1}\chi_{1/2}^{I_2}\chi_{9/16}^{[1]}\Big] \\
&\qquad + \chi_3^{(4)} \Big[\chi_{1/16}^{I_1}\chi_0^{I_2}\chi_{9/16}^{[1]} + \chi_{1/16}^{I_1}\chi_{1/2}^{I_2}\chi_{1/16}^{[1]}\Big]\,; \\
&\chi_0^{(1)}\chi_0^{(1)}\chi_1^{(1)}\chi_0^{(1)} = \chi_0^{(1)}\chi_0^{(1)}\chi_0^{(1)}\chi_1^{(1)} = \\
&\qquad \chi_1^{(4)} \Big[\chi_0^{I_1}\chi_{1/16}^{I_2}\chi_{1/16}^{[2]} + \chi_{1/2}^{I_1}\chi_{1/16}^{I_2}\chi_{9/16}^{[2]}\Big] \\
&\qquad + \chi_3^{(4)} \Big[\chi_0^{I_1}\chi_{1/16}^{I_2}\chi_{9/16}^{[2]} + \chi_{1/2}^{I_1}\chi_{1/16}^{I_2}\chi_{1/16}^{[2]}\Big]\,; \\
&\chi_1^{(1)}\chi_1^{(1)}\chi_0^{(1)}\chi_0^{(1)} = \\
&\qquad \chi_0^{(4)} \Big[\chi_{1/2}^{I_1}\chi_0^{I_2}\chi_I + \chi_0^{I_1}\chi_{1/2}^{I_2}\chi_\theta + \chi_0^{I_1}\chi_0^{I_2}\chi_{3/2}^{[2]} + \chi_{1/2}^{I_1}\chi_{1/2}^{I_2}\chi_{3/2}^{[1]}\Big] \\
&\qquad + \chi_2^{(4)} \Big[\Big(\chi_{1/2}^{I_1}\chi_0^{I_2} + \chi_0^{I_1}\chi_{1/2}^{I_2}\Big)\chi_{2/3} + \Big(\chi_{1/2}^{I_1}\chi_{1/2}^{I_2} + \chi_0^{I_1}\chi_0^{I_2}\Big)\chi_{1/6}\Big] \\
&\qquad + \chi_4^{(4)} \Big[\chi_{1/2}^{I_1}\chi_0^{I_2}\chi_\theta + \chi_0^{I_1}\chi_{1/2}^{I_2}\chi_I + \chi_0^{I_1}\chi_0^{I_2}\chi_{3/2}^{[1]} + \chi_{1/2}^{I_1}\chi_{1/2}^{I_2}\chi_{3/2}^{[2]}\Big]\,; \\
&\chi_0^{(1)}\chi_0^{(1)}\chi_1^{(1)}\chi_1^{(1)} = \\
&\qquad \chi_0^{(4)} \Big[\chi_0^{I_1}\chi_{1/2}^{I_2}\chi_I + \chi_{1/2}^{I_1}\chi_0^{I_2}\chi_\theta + \chi_0^{I_1}\chi_0^{I_2}\chi_{3/2}^{[1]} + \chi_{1/2}^{I_1}\chi_{1/2}^{I_2}\chi_{3/2}^{[2]}\Big] \\
&\qquad + \chi_2^{(4)} \Big[\Big(\chi_{1/2}^{I_1}\chi_0^{I_2} + \chi_0^{I_1}\chi_{1/2}^{I_2}\Big)\chi_{2/3} + \Big(\chi_{1/2}^{I_1}\chi_{1/2}^{I_2} + \chi_0^{I_1}\chi_0^{I_2}\Big)\chi_{1/6}\Big] \\
&\qquad + \chi_4^{(4)} \Big[\chi_0^{I_1}\chi_{1/2}^{I_2}\chi_\theta + \chi_{1/2}^{I_1}\chi_0^{I_2}\chi_I + \chi_0^{I_1}\chi_0^{I_2}\chi_{3/2}^{[2]} + \chi_{1/2}^{I_1}\chi_{1/2}^{I_2}\chi_{3/2}^{[1]}\Big]\,;
\end{aligned}$$

$$
\begin{aligned}
&\chi_1^{(1)}\chi_0^{(1)}\chi_1^{(1)}\chi_0^{(1)} = \chi_0^{(1)}\chi_1^{(1)}\chi_0^{(1)}\chi_1^{(1)} = \\
&\chi_1^{(1)}\chi_0^{(1)}\chi_0^{(1)}\chi_1^{(1)} = \chi_0^{(1)}\chi_1^{(1)}\chi_1^{(1)}\chi_0^{(1)} = \\
&\qquad \chi_0^{(4)}\chi_{1/16}^{I_1}\chi_{1/16}^{I_2}\chi_{3/8} \\
&\qquad + \chi_2^{(4)}\chi_{1/16}^{I_1}\chi_{1/16}^{I_2}\left(\chi_{1/24} + \chi_{25/24}\right) \\
&\qquad + \chi_4^{(4)}\chi_{1/16}^{I_1}\chi_{1/16}^{I_2}\chi_{3/8}; \\
&\chi_1^{(1)}\chi_1^{(1)}\chi_1^{(1)}\chi_0^{(1)} = \chi_1^{(1)}\chi_1^{(1)}\chi_0^{(1)}\chi_1^{(1)} = \\
&\qquad \chi_1^{(4)}\left[\chi_{1/2}^{I_1}\chi_{1/16}^{I_2}\chi_{1/16}^{[2]} + \chi_0^{I_1}\chi_{1/16}^{I_2}\chi_{9/16}^{[2]}\right] \\
&\qquad + \chi_3^{(4)}\left[\chi_{1/2}^{I_1}\chi_{1/16}^{I_2}\chi_{9/16}^{[2]} + \chi_0^{I_1}\chi_{1/16}^{I_2}\chi_{1/16}^{[2]}\right]; \\
&\chi_0^{(1)}\chi_1^{(1)}\chi_1^{(1)}\chi_1^{(1)} = \chi_1^{(1)}\chi_0^{(1)}\chi_1^{(1)}\chi_1^{(1)} = \\
&\qquad \chi_1^{(4)}\left[\chi_{1/16}^{I_1}\chi_{1/2}^{I_2}\chi_{1/16}^{[1]} + \chi_{1/16}^{I_1}\chi_0^{I_2}\chi_{9/16}^{[1]}\right] \\
&\qquad + \chi_3^{(4)}\left[\chi_{1/16}^{I_1}\chi_{1/2}^{I_2}\chi_{9/16}^{[1]} + \chi_{1/16}^{I_1}\chi_0^{I_2}\chi_{1/16}^{[1]}\right]; \\
&\chi_1^{(1)}\chi_1^{(1)}\chi_1^{(1)}\chi_1^{(1)} = \\
&\qquad \chi_0^{(4)}\left[\chi_{1/2}^{I_1}\chi_{1/2}^{I_2}\chi_I + \chi_0^{I_1}\chi_0^{I_2}\chi_\theta + \chi_0^{I_1}\chi_{1/2}^{I_2}\chi_{3/2}^{[2]} + \chi_{1/2}^{I_1}\chi_0^{I_2}\chi_{3/2}^{[1]}\right] \\
&\qquad + \chi_2^{(4)}\left[\left(\chi_0^{I_1}\chi_0^{I_2} + \chi_{1/2}^{I_1}\chi_{1/2}^{I_2}\right)\chi_{2/3} + \left(\chi_0^{I_1}\chi_{1/2}^{I_2} + \chi_{1/2}^{I_1}\chi_0^{I_2}\right)\chi_{1/6}\right] \\
&\qquad + \chi_4^{(4)}\left[\chi_{1/2}^{I_1}\chi_{1/2}^{I_2}\chi_\theta + \chi_0^{I_1}\chi_0^{I_2}\chi_I + \chi_0^{I_1}\chi_{1/2}^{I_2}\chi_{3/2}^{[1]} + \chi_{1/2}^{I_1}\chi_0^{I_2}\chi_{3/2}^{[2]}\right].
\end{aligned}
$$

We use the same notation as earlier, where I_1 and I_2 refer to the Ising model and the remaining characters are those of the $c = 1$ CFT. This formula allows to express the partition (A.2) in terms of the characters of the decomposed theory.

Appendix B

Modular $\mathcal{S}$-Matrices

We write the modular $\mathcal{S}$-matrices for the different models that appear in Chapter 4. These matrices are useful to compute the fusion rules and physical properties like the entropy or the scattering S-matrices.

B.1 Modular $\mathcal{S}$-Matrix for the Ising Model

In the basis (I, ϵ, σ) of the Ising model, the modular $\mathcal{S}$-matrix reads

$$\mathcal{S} = \frac{1}{2}\begin{pmatrix} 1 & 1 & \sqrt{2} \\ 1 & 1 & -\sqrt{2} \\ \sqrt{2} & -\sqrt{2} & 0 \end{pmatrix} .$$

B.2 Modular $\mathcal{S}$-Matrix for the TIM

For the tricritical Ising model, in the basis $(I, \epsilon, t, \epsilon'', \sigma, \sigma')$, the modular $\mathcal{S}$-matrix is given by

$$\mathcal{S} = \sqrt{\frac{1}{5}}\begin{pmatrix} s_2 & s_1 & s_1 & s_2 & \sqrt{2}\,s_1 & \sqrt{2}\,s_2 \\ s_1 & -s_2 & -s_2 & s_1 & \sqrt{2}\,s_2 & -\sqrt{2}\,s_1 \\ s_1 & -s_2 & -s_2 & s_1 & -\sqrt{2}\,s_2 & \sqrt{2}\,s_1 \\ s_2 & s_1 & s_1 & s_2 & -\sqrt{2}\,s_1 & -\sqrt{2}\,s_2 \\ \sqrt{2}\,s_1 & \sqrt{2}\,s_2 & -\sqrt{2}\,s_2 & -\sqrt{2}\,s_1 & 0 & 0 \\ \sqrt{2}\,s_2 & -\sqrt{2}\,s_1 & \sqrt{2}\,s_1 & -\sqrt{2}\,s_2 & 0 & 0 \end{pmatrix} ,$$

where

$$s_1 = \sin\left(\frac{2\pi}{5}\right) , \qquad s_2 = \sin\left(\frac{4\pi}{5}\right) .$$

B.3 Modular $\mathcal{S}$-Matrix for the $c = 1$ CFT

Let us consider a c=1 Z_2 orbifold Gaussian model with $R = \sqrt{2p'}$ and the extended basis

$$\left(I,\, \theta,\, \phi_{p'}^{(i)},\, \phi_\lambda,\, \sigma^{(i')},\, \tau^{(i'')}\right) \quad \text{versus} \quad \left(I,\, \theta,\, \phi_{p'}^{(j)},\, \phi_\mu,\, \sigma^{(j')},\, \tau^{(j'')}\right).$$

In this basis, the modular $\mathcal{S}$-matrix[1] reads

$$\frac{1}{\sqrt{8p'}}\begin{pmatrix} 1 & 1 & 1 & 2 & \sqrt{p'} & \sqrt{p'} \\ 1 & 1 & 1 & 2 & -\sqrt{p'} & -\sqrt{p'} \\ 1 & 1 & 1 & 2(-1)^\mu & (-1)^{i-j'}\sqrt{p'} & (-1)^{i-j''}\sqrt{p'} \\ 2 & 2 & 2(-1)^\lambda & 4\cos\pi\frac{\lambda\mu}{p'} & 0 & 0 \\ \sqrt{p'} & -\sqrt{p'} & (-1)^{i'-j}\sqrt{p'} & 0 & \delta_{i'j'}\sqrt{2p'} & -\delta_{i'j''}\sqrt{2p'} \\ \sqrt{p'} & -\sqrt{p'} & (-1)^{i''-j}\sqrt{p'} & 0 & -\delta_{i''j'}\sqrt{2p'} & \delta_{i''j''}\sqrt{2p'} \end{pmatrix}.$$

---

[1] The expression of the modular $\mathcal{S}$-matrix in Ref. [9], Eq. (2.84), contains a misprint. The last element in the third row of the matrix has actually the opposite sign.

Bibliography

[1] Affleck, I., 1995, Acta Phys. Pol. B **26**, 1869. 39, 78

[2] Affleck, I., and A. W. W. Ludwig, 1991, Nucl. Phys. B **360**(2–3), 641. 74, 82, 83, 84, 86, 88

[3] Affleck, I., and A. W. W. Ludwig, 1991, Nucl. Phys. B **352**(3), 849. 74, 82, 83, 84, 86, 88

[4] Affleck, I., and A. W. W. Ludwig, 1991, Phys. Rev. Lett. **67**(2), 161. 44

[5] Affleck, I., and A. W. W. Ludwig, 1992, Phys. Rev. Lett. **68**(7), 1046. 74, 77, 78, 79, 98

[6] Affleck, I., and A. W. W. Ludwig, 1993, Phys. Rev. B **48**(10), 7297. 45, 86

[7] Affleck, I., A. W. W. Ludwig, and B. A. Jones, 1995, Phys. Rev. B **52**(13), 9528. 74, 77, 79, 82

[8] Affleck, I., A. W. W. Ludwig, H.-B. Pang, and D. L. Cox, 1992, Phys. Rev. B **45**(14), 7918. 86

[9] Affleck, I., M. Oshikawa, and H. Saleur, 2001, Nucl. Phys. B **594**(3), 535. 93, 106

[10] Anderson, P. W., 1961, Phys. Rev. **124**(1), 41. 26

[11] Anderson, P. W., 1970, J. Phys. C **3**(12), 2436. 32

[12] Anisimov, V. I., I. A. Nekrasov, D. E. Kondakov, T. M. Rice, and M. Sigrist, 2002, Eur. Phys. J. B **25**, 191. 5

[13] Attaccalite, C., and M. Fabrizio, 2003, Phys. Rev. B **68**(15), 155117. 15, 54, 57

[14] Bagger, J., D. Nemeschansky, and S. Yankielowicz, 1988, Phys. Rev. Lett. **60**(5), 389. 101

[15] Balicas, L., S. Nakatsuji, D. Hall, T. Ohnishi, Z. Fisk, Y. Maeno, and D. J. Singh, 2005, Phys. Rev. Lett. **95**(19), 196407. 5

[16] Bednorz, J. G., and K. A. Müller, 1986, Z. Phys. B **64**(2), 189. 2

[17] Belavin, A. A., A. M. Polyakov, and A. B. Zamolodchikov, 1984, Nucl. Phys. B **241**(2), 333. 39

[18] Biermann, S., L. de' Medici, and A. Georges, 2005, Phys. Rev. Lett. **95**(20), 206401. 71

[19] de Boer, J. H., and E. J. W. Verwey, 1937, Proc. Phys. Soc. **49**(4S), 59. 1

[20] Brinkman, W. F., and T. M. Rice, 1970, Phys. Rev. B **2**(10), 4302. 10, 13

[21] Bulla, R., T. A. Costi, and D. Vollhardt, 2001, Phys. Rev. B **64**(4), 45103. 39

[22] Bünemann, J., F. Gebhard, and W. Weber, 1997, J. Phys.: Condens. Matter **9**(35), 7343. 15

[23] Bünemann, J., W. Weber, and F. Gebhard, 1998, Phys. Rev. B **57**(12), 6896. 15

[24] Caffarel, M., and W. Krauth, 1994, Phys. Rev. Lett. **72**(10), 1545. 28, 58

[25] Capone, M., M. Fabrizio, C. Castellani, and E. Tosatti, 2002, Science **296**(5577), 2364. 48, 76

[26] Capone, M., M. Fabrizio, C. Castellani, and E. Tosatti, 2004, Phys. Rev. Lett. **93**(4), 47001. 48, 76, 77, 99

[27] Cardy, J. L., 1984, Nucl. Phys. B **240**(4), 514. 40

[28] Cardy, J. L., 1986, Nucl. Phys. B **275**(2), 200. 43

[29] Cardy, J. L., 1986, Nucl. Phys. B **270**, 186. 42, 43

[30] Cardy, J. L., 1989, Nucl. Phys. B **324**(3), 581. 40

[31] Cardy, J. L., and D. C. Lewellen, 1991, Phys. Lett. B **259**(3), 274. 45

[32] Coleman, P., C. Pepin, Q. Si, and R. Ramazashvili, 2001, J. Phys.: Condens. Matter **13**(35), R723. 74

[33] Costi, T. A., A. C. Hewson, and V. Zlatic, 1994, J. Phys.: Condens. Matter **6**(13), 2519. 39

[34] De Leo, L., and M. Fabrizio, 2004, Phys. Rev. B **69**(24), 245114. 76, 80, 99

[35] Di Francesco, P., P. Mathieu, and D. Sénéchal, 1996, *Conformal Field Theory* (Springer, New York). 39, 78, 81, 82, 93, 101

[36] Fabrizio, M., A. F. Ho, L. De Leo, and G. E. Santoro, 2003, Phys. Rev. Lett. **91**(24), 246402. 76

[37] Ferrero, M., F. Becca, M. Fabrizio, and M. Capone, 2005, Phys. Rev. B **72**(20), 205126. 47

[38] Frota, H. O., and L. N. Oliveira, 1986, Phys. Rev. B **33**(11), 7871. 39

[39] Fujimori, A., I. Hase, H. Namatame, Y. Fujishima, Y. Tokura, H. Eisaki, S. Uchida, K. Takegahara, and F. M. F. de Groot, 1992, Phys. Rev. Lett. **69**(12), 1796. 3, 4

[40] Gebhard, F., 1990, Phys. Rev. B **41**(13), 9452. 13

[41] Georges, A., and G. Kotliar, 1992, Phys. Rev. B **45**(12), 6479. 26, 28

[42] Georges, A., G. Kotliar, W. Krauth, and M. J. Rozenberg, 1996, Rev. Mod. Phys. **68**(1), 13. 6, 20, 26, 30, 75, 77

[43] Georges, A., and W. Krauth, 1992, Phys. Rev. Lett. **69**(8), 1240. 29

[44] Gonzalez-Buxton, C., and K. Ingersent, 1998, Phys. Rev. B **57**(22), 14254. 35

[45] Gutzwiller, M. C., 1963, Phys. Rev. Lett. **10**(5), 159. 9, 10

[46] Gutzwiller, M. C., 1964, Phys. Rev. **134**(4A), A923. 10

[47] Gutzwiller, M. C., 1965, Phys. Rev. **137**(6A), A1726. 10

[48] Han, J. E., 2004, Phys. Rev. B **70**(5), 54513. 48

[49] Han, J. E., O. Gunnarsson, and V. H. Crespi, 2003, Phys. Rev. Lett. **90**(16), 167006. 48

[50] Han, J. E., M. Jarrell, and D. L. Cox, 1998, Phys. Rev. B **58**(8), R4199. 48

[51] Han, J. E., E. Koch, and O. Gunnarsson, 2000, Phys. Rev. Lett. **84**(6), 1276. 48

[52] Hewson, A. C., 1997, *The Kondo Problem to Heavy Fermions* (Cambridge University Press, Cambridge). 26

[53] Hirsch, J. E., and R. M. Fye, 1986, Phys. Rev. Lett. **56**(23), 2521. 26

[54] Hubbard, J., 1963, Proc. Roy. Soc. **276**(1365), 238. 9

[55] Ingersent, K., A. W. W. Ludwig, and I. Affleck, 2005, Phys. Rev. Lett. **95**(25), 257204. 74, 91

[56] Ishibashi, N., 1989, Mod. Phys. Lett. A **4**(3), 251. 42

[57] Ishibashi, N., and T. Onogi, 1989, Nucl. Phys. B **318**(1), 239. 42

[58] Jamneala, T., V. Madhavan, and M. F. Crommie, 2001, Phys. Rev. Lett. **87**(25), 256804. 74

[59] Jarrell, M., 1992, Phys. Rev. Lett. **69**(1), 168. 29

[60] Jones, B. A., and C. M. Varma, 1987, Phys. Rev. Lett. **58**(9), 843. 74, 75, 77, 79

[61] Jones, B. A., and C. M. Varma, 1989, Phys. Rev. B **40**(1), 324. 74, 77, 79

[62] Jones, B. A., C. M. Varma, and J. W. Wilkins, 1988, Phys. Rev. Lett. **61**(1), 125. 74, 77, 79

[63] Kanamori, J., 1963, Prog. Theor. Phys. **30**(3), 275. 9

[64] Koga, A., Y. Imai, and N. Kawakami, 2002, Phys. Rev. B **66**(16), 165107. 48

[65] Koga, A., K. Inaba, and N. Kawakami, 2005, Prog. Theor. Phys. Suppl. **160**, 253, and references therein. 72

[66] Koga, A., N. Kawakami, T. M. Rice, and M. Sigrist, 2004, Mott transitions in the multi-orbital systems, URL `arXiv.org:cond-mat/0406457`. 48

[67] Koga, A., N. Kawakami, T. M. Rice, and M. Sigrist, 2004, Phys. Rev. Lett. **92**(21), 216402. 48

[68] Kondo, J., 1964, Prog. Theor. Phys. **32**(1), 37. 31

[69] Kotliar, G., S. Y. Savrasov, G. Pálsson, and G. Biroli, 2001, Phys. Rev. Lett. **87**(18), 186401. 75

[70] Krishna-murthy, H. R., J. W. Wilkins, and K. G. Wilson, 1980, Phys. Rev. B **21**(3), 1003. 33

[71] Krishna-murthy, H. R., J. W. Wilkins, and K. G. Wilson, 1980, Phys. Rev. B **21**(3), 1044. 33

[72] Kudasov, Y. B., and V. M. Uzdin, 2002, Phys. Rev. Lett. **89**(27), 276802. 74

[73] Lanczos, C., 1950, J. Res. Nat. But. Standards **45**, 255. 26

[74] Langreth, D. C., 1966, Phys. Rev. **150**(2), 516. 28

[75] Lazarovits, B., P. Simon, G. Zarand, and L. Szunyogh, 2005, Phys. Rev. Lett. **95**(7), 77202. 74

[76] Lefebvre, S., P. Wzietek, S. Brown, C. Bourbonnais, D. Jérome, C. Mézière, M. Fourmigué, and P. Batail, 2000, Phys. Rev. Lett. **85**(25), 5420. 3

[77] Lichtenstein, A. I., and M. I. Katsnelson, 2000, Phys. Rev. B **62**(14), R9283. 75

[78] Liebsch, A., 2003, Phys. Rev. Lett. **91**(22), 226401. 48

[79] Liebsch, A., 2004, Phys. Rev. B **70**(16), 165103. 48

[80] Maeno, Y., H. Hashimoto, K. Yoshida, S. Nishizaki, T. Fujita, J. G. Bednorz, and F. Lichtenberg, 1994, Nature **372**(6506), 532. 4

[81] Maier, T., M. Jarrell, T. Pruschke, and M. H. Hettler, 2005, Rev. Mod. Phys. **77**(3), 1027. 75

[82] Manini, N., G. E. Santoro, A. Dal Corso, and E. Tosatti, 2002, Phys. Rev. B **66**(11), 115107. 48

[83] McWhan, D. B., A. Menth, J. P. Remeika, W. F. Brinkman, and T. M. Rice, 1973, Phys. Rev. B **7**(5), 1920. 2, 3

[84] de' Medici, L., A. Georges, and S. Biermann, 2005, Phys. Rev. B **72**(20), 205124. 71

[85] Metzner, W., and D. Vollhardt, 1987, Phys. Rev. Lett. **59**(1), 121. 13, 15

[86] Metzner, W., and D. Vollhardt, 1988, Phys. Rev. B **37**(13), 7382. 13, 15

[87] Metzner, W., and D. Vollhardt, 1989, Phys. Rev. Lett. **62**(3), 324. 14, 20, 23

[88] Misguich, G., and C. Lhuillier, 2005, in *Frustrated Spin Systems*, edited by H. T. Diep (World-Scientific, Singapore), p. 981, and references therein. 7

[89] Mo, S.-K., J. D. Denlinger, H.-D. Kim, J.-H. Park, J. W. Allen, A. Sekiyama, A. Yamasaki, K. Kadono, S. Suga, Y. Saitoh, T. Muro, P. Metcalf, *et al.*, 2003, Phys. Rev. Lett. **90**(18), 186403. 3, 4

[90] Moeller, G., Q. Si, G. Kotliar, M. Rozenberg, and D. S. Fisher, 1995, Phys. Rev. Lett. **74**(11), 2082. 59, 65, 66, 67

[91] Mott, N., 1990, *Metal Insulator Transition* (Taylor and Francis, London). 73

[92] Mott, N. F., 1949, Proc. Phys. Soc. A **62**(7), 416. 1, 10

[93] Mott, N. F., and R. Peierls, 1937, Proc. Phys. Soc. **49**(4S), 72. 1

[94] Müller-Hartmann, E., 1989, Z. Phys. B **74**(4), 507. 14, 23

[95] Nakatsuji, S., and Y. Maeno, 2000, Phys. Rev. Lett. **84**(12), 2666. 4, 5

[96] Ono, Y., M. Potthoff, and R. Bulla, 2003, Phys. Rev. B **67**(3), 35119. 48

[97] Paul, B. C., and K. Ingersent, 1996, Frustration-induced non-fermi-liquid behavior in a three-impurity kondo model, URL `arXiv.org:cond-mat/9607190`. 74, 75, 90

[98] Potthoff, M., M. Aichhorn, and C. Dahnken, 2003, Phys. Rev. Lett. **91**(20), 206402. 75

[99] Pruschke, T., and R. Bulla, 2005, Eur. Phys. J. B **44**(2), 217. 48

[100] Rozenberg, M. J., X. Y. Zhang, and G. Kotliar, 1992, Phys. Rev. Lett. **69**(8), 1236. 29

[101] Sakai, O., Y. Shimizu, and T. Kasuya, 1989, J. Phys. Soc. Jap. **58**(10), 3666. 39

[102] Savkin, V. V., A. N. Rubtsov, M. I. Katsnelson, and A. I. Lichtenstein, 2005, Phys. Rev. Lett. **94**(2), 26402. 74

[103] Schrieffer, J. R., and D. C. Mattis, 1965, Phys. Rev. **140**(4A), A1412. 28

[104] Schrieffer, J. R., and P. A. Wolff, 1966, Phys. Rev. **149**(2), 491. 31, 67

[105] Sénéchal, D., D. Perez, and M. Pioro-Ladrière, 2000, Phys. Rev. Lett. **84**(3), 522. 75

[106] Si, Q., 2004, Adv. Sol. St. Phys. **44**, 253. 74

[107] Verlinde, E., 1988, Nucl. Phys. B **300**, 360. 43

[108] Vollhardt, D., 1984, Rev. Mod. Phys. **56**(1), 99. 13

[109] Wang, S.-C., H.-B. Yang, A. K. P. Sekharan, S. Souma, H. Matsui, T. Sato, T. Takahashi, C. Lu, J. Zhang, R. Jin, D. Mandrus, E. W. Plummer, *et al.*, 2004, Phys. Rev. Lett. **93**(17), 177007. 5

[110] Wilson, K. G., 1975, Rev. Mod. Phys. **47**(4), 773. 32

[111] Withoff, D., and E. Fradkin, 1990, Phys. Rev. Lett. **64**(15), 1835. 29

[112] Wolff, U., 1983, Nucl. Phys. B **225**(3), 391. 14

[113] Yokoyama, H., and H. Shiba, 1987, J. Phys. Soc. Jap. **56**(4), 1490. 13

[114] Zhang, X. Y., M. J. Rozenberg, and G. Kotliar, 1993, Phys. Rev. Lett. **70**(11), 1666. 29